Construction and Characterization of Monolithic Femtosecond Fiber Lasers

Liu, Xiaomin ; Lægsgaard, Jesper; Turchinovich, Dmitry

Publication date:
2011

Document Version
Publisher's PDF, also known as Version of record

Construction and Characterization of Monolithic Femtosecond Fiber Lasers

Xiaomin Liu

Department of Photonics Engineering
Technical University of Denmark

PhD thesis
August, 2011

Contents

List of Publications

List of papers included in this thesis:

I. J. T. Kristensen, A. Houmann, X. Liu and D. Turchinovich. Low-loss polarization-maintaining fusion splicing of single-mode fibers and hollow-core photonic crystal fibers, relevant for monolithic fiber laser pulse compression. *Opt. Express*, 16(13):9986-95, 2008.

II. D. Turchinovich, X. Liu and J. Lægsgaard. Monolithic all-PM femtosecond yb-fiber laser stabilized with a narrow-band fiber bragg grating and pulse-compressed in a hollow-core photonic crystal fiber. *Opt. Express*, 16(18):14004-14, 2008.

III. X. Liu, J. Lægsgaard and D. Turchinovich. Self-stabilization of a mode-locked femtosecond fiber laser using a photonic bandgap fiber. *Opt. Lett.*, 35(7):913-5, 2010.

IV. X. Liu, J. Lægsgaard and D. Turchinovich. Highly-stable monolithic femtosecond yb-fiber laser system based on photonic crystal fibers. *Opt. Express*, 18(15):15475-83, 2010.

V. X. Liu, E. U. Rafailov, D. Livshits and D. Turchinovich. Quantum well saturable absorber mirror with electrical control of modulation depth. *Appl. Phys. Lett.*, 97(5), 2010.

Partial list of refereed conference proceedings:

VI. D. Turchinovich, X. Liu, and J. Lægsgaard. Monolithic Femtosecond Yb-fiber Lasers with Photonic Crystal Fibers. *International Conference on Advanced Laser Technologies (ALT¡¯08)*,Siofok, Hungary, 2008 .

VII. X. Liu, J. Lægsgaard and D. Turchinovich. Monolithic Yb-fiber femtosecond laser using photonic crystal fiber *EOS Annual Meeting*, Paris, 2008.

VIII. D. Turchinovich, X. Liu, and J. Lægsgaard Monolithic stabilized Yb-fiber all-PM laser directly delivering nJ-level femtosecond pulses. *EOS IEEE LEOS 21st Annual Meeting*, CA, 2008.

IX. X. Liu, J. Lægsgaard and D. Turchinovich. All-PM monolithic fs Yb-fiber laser, dispersion-managed with all-solid photonic bandgap fiber. *Conference on Lasers and Electro-optics(CLEO)*, Baltimore, MD, 2009.

X. X. Liu, J. Lægsgaard and D. Turchinovich. Monolithic all-PM femtosecond Yb-doped fiber laser using photonic bandgap fibers. *Proceeding of 22nd Annual Meeting of IEEE Photonics Society*, Antalya, Turkey, 2009.

XI. D. Turchinovich, X. Liu, and J. Lægsgaard Monolithic Yb-fiber femtosecond laser with intracavity all-solid PBG fiber and ex-cavity HC-PCF. *SPIE Photonics West 2010*, , San Franscisco, CA, 2010.

XII. X. Liu, E. U. Rafailov, D. Livshits and D. Turchinovich.. Quantum well saturable absorber mirror with electrical control of modulation depth. *Conference on Lasers and Electro-optics(CLEO)*, San Jose, CA, 2010.

List of Symbols and Acronyms

AC	Autocorrelation
ASE	Amplified Spontaneous Emission
AS-PCF	All-Solid Photonid Crystal Fiber
CPA	Chirped Pulse Amplification
E-SESAM	Electrically Controlled SESAM
FBG	Fiber Bragg Grating
FROG	Frequency Resolved Optical Gating
FWHM	Full Width at Half Maximum
GNLSE	Generalized Nonlinear Schrödinger Equations
GVD	Group Velocity Dispersion
HC-PCF	Hollow-Core Photonic Crystal Fiber
KLM	Kerr Lens Mode-Locking
LD	Laser Diode
LMA	Large Mode Area
MIIPS	Mutiphoto Intrapulse Interference Phase Scan
NPR	Nonlinear Polarization Rotation
PFC	Polarization Filter Coupler

PISO	Polarization-maintaining Isolator
PM	Polarization Maintaining
QWs	Quantum Wells
QDs	Quantum Dots
QCSE	Quantum-Confined Stark Effect
SA	Saturable Absorber
SC-PBG	Solid-Core Photonic Bandgap Fiber
SESAM	Semiconductor Saturable Absorber Mirror
SEM	Scanning Electron Microscope
SMF	Single Mode Fiber
SLD	Super Luminescent Diode
SPM	Self-Phase Modulation
SRS	Stimulated Raman Scattering
TIR	Total Internal Reflection
TOD	Third-Order Dispersion
WDM	Wavelength Division Multiplexer
XPM	Cross-Phase Modulation

Acknowledgements

I came to Denmark in the spring of 2008 for pursuing a PhD degree. Time slips away silently. Now, I am approaching the destination of my PhD journey. In this journey, there are a lot of people who stand by me and kindly offer their help to me. Without their help, it would be very hard for me to write this thesis. Here, I want to express my sincere gratitude to them.

I would like to thank my supervisors Jesper Lægsgaard and Dmitry Turchinovich. I learned about mode-locked lasers from them. Jesper is always patient to all my theoretical and experimental questions. Dmitry showed me all the knowledge needed and is especially a great supervisor on guiding me about the experimental research. Meanwhile, both of them are also teachers of my PhD courses. I really had a great time with them!

I would like to express my special appreciation to Lasse Leick, Thomas Vestergaard Andersen, Jens Kristian Lyngsoe and Sren Agger from NKT Photonics A/S for their great help and many insightful comments.

The group leaders Karsten Rottwitt and Peter Uhd Jepsen are also responsible for the project. I also thank them for the courses taught by them and I really benefit a lot from the courses though I didn't learn well and got a poor score at that time:)

I would like to thank Rasmus Kjelsmark Olsson, Jonas Christian Due Buron, Kresten Yvind and Morten Bache for their help especially on FROG measurements.

Thanks a lot to me master project supervisor Xianmin Zhang at Zhejiang University and I learned the first lessons about research from him.

I also acknowledge the helpfulness of the other group members: Uffe Mller, Finn Eichhorn, Lei Wei, Binbin Zhou, Henrik Porte, Sebastian Marschall, Scott Wu Yuan, Johannes Weirich, Anna Chiara Brunetti, Kristian Rymann Hansen, Valentina Cristofori, Alessio Stefani, Kristian Nielsen, Michael Henoch Frosz, Toke

Lund-Hansen and Krzysztof Iwaszczuk.

Great thanks to my family: my husband Wei Yan, my mom, dad, my brother and to all my friends for supporting me all the time.

Finally, I would like to acknowledge the financial support from the HTF project "High-power fibre lasers for eye care".

Chapter 1

Introduction

Ultrafast lasers have been a very rich research field since the first one was demonstrated by De Maria in 1966 [1]. The generated ultrashort pulses open up fascinating possibilities based on their unique properties [2]: the pulse energy can be concentrated in a temporal interval as short as several 10^{-15} s which corresponds to only a few optical cycles in the visible range; the pulse peak power can be extremely high even at moderate pulse energies and the geometrical length of a fs pulse only amounts to several micrometers. Today short pulsed lasers have a wide range of applications, including medical [3, 4], industrial [5, 6] applications, as well as ultrafast science [7, 8]. Recent progress in the development of fs fiber lasers has resulted in pulse energies [9] and durations [10] comparable to the solid-state lasers.

1.1 Background

1.1.1 Mode-Locked Lasers

Mode-locking is a technique referred to a locking of the phase relations between many neighboring longitudinal modes of the laser cavity. Locking of such phase relations enables a periodic variation in the laser output which is stable over time. The periodicity which is also called as repetition rate is decided by the round trip time of the cavity. The scheme of mode-locking can be seen in Figure 1.1. Figure 1.1 (a) shows all the mode-locked modes have the same phase and the pulses are transform limited which are unchirped. Figure 1.1 (b) shows the mode-locked modes

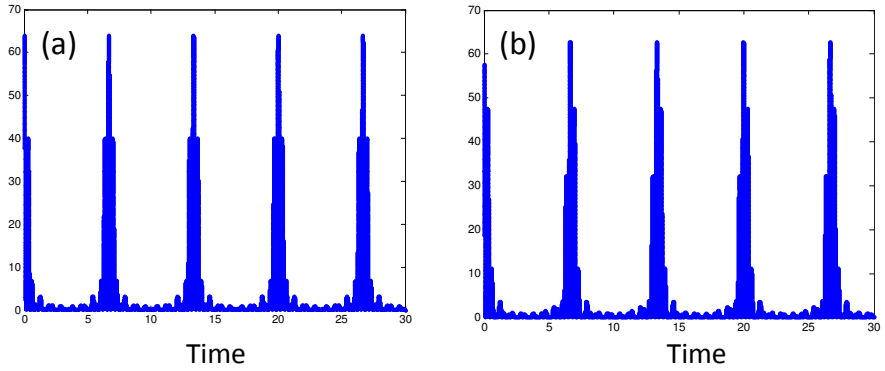

Figure 1.1: Illustration of phase relation when mode-locking. (a) The longitudinal modes with the same phase which induces Fourier transform limited pulses (unchirp). (b) The longitudinal modes have different phases but fixed phase relationship which induced chirped pulses.

have different phase and those pulses are chirped. It's noted that for short pulses, the number of longitudinal modes are much larger. If sufficiently many longitudinal modes are locked together with only small phase differences between the individual modes, it results in a short pulse with significant larger peak power than the average power.

A laser in steady system is a feedback back system where the gain per round trip is balanced by the losses. If a power dependent nonlinear element which has higher loss at lower optical power than the higher power is inserted into the laser cavity, the laser may favor a superposition of longitudinal modes corresponding to a pulse. For stable mode-locking, a further requirement is that the pulse can reproduce itself after one round trip. The phase relations between different modes are affected by effects such as dispersion, gain bandwidth, nonlinear phase shifts and so on.

According to active and passive mode-locking mechanisms, there are various designs of mode-locking lasers. The detail of mode-locking mechanisms is described in Chapter 2. Active mode-locking lasers including Dye lasers and Gas lasers e.g. ionized-argon or krypton lasers [11]. The advantage of active mode-locking mechanism is that the laser can achieve high power. The drawbacks are that it is extreme sensitive to the relative fluctuations of the imposed frequency Ω and the intermode frequency interval c/L, where L is the optical length of one round trip. And it is also very difficult to establish subpicosecond regimes with just a single active locking procedure. Passive mode-locking lasers including solid-state lasers, pulsed semicon-

ductor lasers and femtosecond fiber lasers. Compared with active mode-locking lasers, the passive mode-locking lasers are easier to set up and more stable.

1.1.2 Monolithic Mode-Locked Fiber Lasers

Classical solid-state mode-locked lasers i.e. lasers based on crystals have traditionally dominated the market, e.g. the Ti:Sapphire and the Nd:YAG lasers. In terms of reliability and long term stability compared with the Gas lasers and Dye lasers, the solid-state lasers are still the preferred choice. However, the solid-state lasers still require stable laboratory-like working environments such as optical table and constant room temperature. Furthermore, the solid-state lasers are really expensive and need often maintenance which is also a high consumption. Solutions to these restricts have to be found.

The potential of making compact, stable femtosecond fiber lasers with low price makes mode-locked fiber lasers a very promising alternative to classical solid-state lasers. High gain rare-earth doped fiber with broad gain bandwidth and excellent pulse quality is one of the key properties. The invention of anomalous dispersion PCF fibers at wavelengths where the traditional silica fiber is strongly normal gives the all-fiber lasers the opportunity to generate femstosecond pulses. And the development of large mode area fibers makes high power fiber amplifier possible which can offer high power pulse output from fiber directly.

For biophotonic imaging applications which are widely used in medicine and hospitals, stable mode-locked lasers with central wavelength around 1 um are particularly important. However, the designed mode-locked fiber lasers (e.g. [12]) before are still not stable enough. One reason is that there are still free space optical components in the laser system which are very sensitive to the environment such as minor vibration or temperature fluctuations. Another problem is that most of the fiber lasers are assembled by non-PM fibers whose polarization state are easily effected and induces the instability.

Both the femtosecond fiber lasers described in this thesis are monolithic (with no free space components) and all the fibers are PM. The experimental results showed high operational and environmental stability of the lasers.

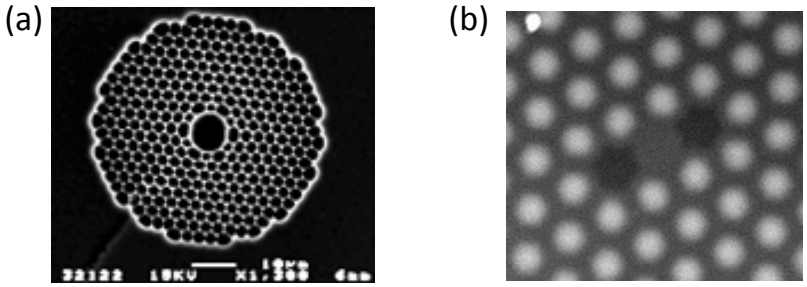

Figure 1.2: (a) SEM image of the HC-PCF. (b) SEM image of the SC-PBG. Courtesy of B. J. Mangan, Crystal Fibre A/S.

1.1.3 Photonic Crystal Fibers

PCFs were first experimentally demonstrated in the mid-90's by J. C. Knight [13]. With the rapid development of technology, today PCFs are already manufactured as commercial products [14] and PCF technology is by far the most mature of the various photonic crystal technologies currently investigated [15]. PCF is an optical fiber which has a transverse refractive index profile with a structure on the um scale. It is more complicated than the radially symmetric index distributions of conventional fibers. Generally, the transverse microstructure includes an array of airholes running along the length of the fiber, but the term PCF also covers fibers comprising other combinations of materials with different refractive indexes. Two types of fabricated PCF geometries are shown in Figure 1.2.

The periodic modulation of the refractive index in a PCF can result in photonic band gaps which prohibits the photons of certain wavelengths. The core for guiding light can be created by introducing a defect into the periodic structure. Light of certain wavelengths is then confined to this core if the surrounding structure exhibits a bandgap at these wavelength [16]. This term of fibers are called photonic bandgap fibers.

According to different applications, PCFs can be sorted into: large mode-area PCFs, small mode-area PCFs and solid-core photonic bandgap fibers. The large mode-area fibers are of interest for applications where nonlinear effects need to be suppressed, e.g. the dispersion compensation application for high power fiber lasers. The large mode area also helps to increase the power threshold for breakdown of the glass. The detail can be seen on Chapter 4 and 5. If the mode area of an

optical fiber is scaled down to very small values, the nonlinear coefficient becomes large. This kind of fibers are of interest for applications using nonlinear effects, e.g. signal processing and frequency conversion. One example of this application is shown on Chapter 7. Solid-core photonic bandgap fibers achieve bandgap effect by an 'inverted' PCF design where the airholes are replaced by regions of a higher refractive index and the core becomes a low index defect. Such a structure can be made either by stacking elements of doped silica into a preform, or by infiltrating the airholes of a standard index-guiding PCF with a high-index liquid [15]. The main advantage of this kind of fibers are on the dispersion prosperities since they have a very strong anomalous waveguide dispersion. Therefore, solid-core PBG fibers can be used to obtain net anomalous or zero dispersion at wavelengths where the material dispersion of silica is strongly normal. Meanwhile, such fibers still have similar core area as normal fiber which is easy to couple and does not have excessive nonlinear effects. Chapter 5 shows an example of such fiber for dispersion compensation in the fiber laser cavity. The intrinsic filtering effect of PBG fibers also offers applications on filtering unwanted wavelengths in fiber amplifiers.

1.2 Outline of this Thesis

The present thesis is composed of two main parts. In the first part, a fundamental introduction to mode-locked lasers is given. In the second part, the author's works are described. Hopefully, the first part of this thesis can give readers a clear introduction, even if they know nothing about ultrashort lasers; the second part can give a clear summary to the author's work.

The first part contains three chapters. In chapter 2, pulse propagation in optical and mode-locking mechanisms are introduced. In chapter 3, the relevant characterization techniques for mode-locked lasers are described.

The second part contains four chapters. Chapter 4 presents one all-fiber laser stabilized with a narrow band FBG. Chapter 5 presents one highly-stable self-starting femtosecond fiber laser system based on photonic crystal fibers. Chapter 6 presents the quantum well SESAM with electrical control of modulation depth. Chapter 7 presents the applications of mode-locked fiber lasers.

Conclusions, future work, and summary of the author's contributions to the published papers, are given in chapters 8.

Chapter 2

Theory

2.1 Introduction

Light propagation in fibers can be modeled well and can have high accuracy on simulation of its interaction with the surroundings. The model described in this chapter is based on Maxwell's equation for electromagnetic radiation. Approximations are made due to the complexity of the system. GNLSE which can accurately model nonlinear pulse propagation in optical fibers is introduced in the first part. The second part of this chapter presents the mode-locking mechanisms of lasers.

2.2 Pulse Propagation in Fibers

The GNLSE has become a standard tool for simulating the optical pulses propagation in optical fibers [17]. The GNLSE has been found to be highly useful not only in the predictions of nonlinear experiments in standard optical fibers, but also in the description of extreme complex phenomena such as supercontinuum generation in small-core photonic crystal fibers [18]. This chapter will introduce the theory for the mode-locking lasers. Like all electromagnetic phenomena, the optical pulses propagation is also governed by Maxwell's equations. In differential form these are [19]

$$\nabla \times \mathbf{E} = -\frac{\partial \mathbf{B}}{\partial t}, \tag{2.2.1}$$

$$\nabla \times \mathbf{H} = \frac{\partial \mathbf{D}}{\partial t} + \mathbf{J}, \tag{2.2.2}$$

$$\nabla \cdot \mathbf{D} = \rho, \tag{2.2.3}$$

$$\nabla \cdot \mathbf{B} = 0, \tag{2.2.4}$$

where $\mathbf{E}$ and $\mathbf{H}$ are electric and magnetic field vectors in $[\mathbf{V}/m]$ and $[\mathbf{A}/m]$ respectively, $\mathbf{D}$ and $\mathbf{B}$ refer to electric and magnetic induction in $[\mathbf{C}/m^2]$ and $[\mathbf{Wb}/m^2]$, $\mathbf{J}$ is the electric current density in $[\mathbf{A}/m^2]$ and ρ is the electric charge density in $[\mathbf{C}/m^3]$. In our interested mode-locking laser systems, free charges are negligible, $\mathbf{J} = 0$ and $\rho = 0$.

The electric and magnetic induction $\mathbf{D}$ and $\mathbf{B}$ are related to electric and magnetic fields $\mathbf{E}$ and $\mathbf{H}$ through the constitutive relations

$$\mathbf{D} = \varepsilon_0 \mathbf{E} + \mathbf{P}, \tag{2.2.5}$$

$$\mathbf{B} = \mu_0 \mathbf{H}, \tag{2.2.6}$$

where $\varepsilon_0 = 8.854 \cdot 10^{12}\ \mathbf{F}/m$ is the vacuum permittivity and $\mu_0 = 4\pi \cdot 10^{-7}\ \mathbf{H}/m$ is the vacuum permeability. And here it should be noticed that we assume the induced magnetic polarization $\mathbf{M} = 0$ for our system which should be added to the right part of Eq. (2.2.6).

From Eq. (2.2.1), (2.2.2), (2.2.3), (2.2.5) and (2.2.6) and using $\nabla \times \nabla \times \mathbf{E} \equiv \nabla(\nabla \cdot \mathbf{E}) - \nabla^2 \mathbf{E}$, we can obtain

$$\nabla^2 \mathbf{E} = \frac{1}{c^2} \frac{\partial^2 \mathbf{E}}{\partial t^2} + \mu_0 \frac{\partial^2 \mathbf{P}}{\partial t^2}, \tag{2.2.7}$$

where $\mathbf{E}$ and $\mathbf{P}$ are in time domain $\mathbf{E}(\mathbf{r}, t)$ and $\mathbf{P}(\mathbf{r}, t)$ respectively.

And the induced polarization can be expressed as

$$\mathbf{P} = \mathbf{P}_L + \mathbf{P}_{NL} = \varepsilon_0 \chi^{(1)} : \mathbf{E} + \varepsilon_0 \chi^{(2)} : \mathbf{EE} + \varepsilon_0 \chi^{(2)} : \mathbf{EEE} + \ldots, \tag{2.2.8}$$

where the linear and nonlinear induced electric polarization parts $\mathbf{P}_L$ and $\mathbf{P}_{NL}$ are related to the electric field $\mathbf{E}$, and $\chi^{(1)} \ldots \chi^{(n)}$ are susceptibilities.

When fiber as the transmission medium, we consider the induced electric polarization only the principles of local response and time invariance. The real part of $\chi^{(1)}$ is related to the real part of the refractive index of the material and relates to linear phase changes. The imaginary part relates to the linear losses and gains. Because of the microscope inversion symmetry of SiO_2, all the even order susceptibilities are zero. Higher odd $\chi^{(n)}$, $n > 3$ are very weak, and hence only $\chi^{(3)}$ is the significant nonlinear term.

When we solve Eq.(2.2.7) in fibers, there are three assumptions: 1) $\mathbf{P}_{NL}$ is treated as a small perturbation to $\mathbf{P}_L$; 2) the electric field is linearly polarized which is the case since PM fibers used in our mode-locking laser systems; 3)the optical is assumed to be quasi-monochromatic which is valid for pulses as short as 100 fs.

In order ro adopt slowly varying envelope approximation, the rapidly varying part of the electric field is seperated out:

$$\mathbf{E}(\mathbf{r},t) = \frac{1}{2}\hat{x}[E(\mathbf{r},t)exp(-iw_0t) + c\cdot c\cdot], \tag{2.2.9}$$

where $\hat{x}$ is the polarization unit vector, $E(\mathbf{r},t)$ is a slowly varying function of time and w_0 is the carrier or central frequency. The induced nonlinear polarization components $\mathbf{P}_{NL}$ can also be expressed in the similar way:

$$\mathbf{P}_{NL}(\mathbf{r},t) = \frac{1}{2}\hat{x}[P_{NL}(\mathbf{r},t)exp(-iw_0t) + c\cdot c\cdot]. \tag{2.2.10}$$

Then using the Fourier transforms:

$$E(\mathbf{r},w-w_0) = \int_{-\infty}^{\infty} E(\mathbf{r},t)exp[i(w-w_0)t]dt, \tag{2.2.11}$$

and combine with Eq.(2.2.8), Eq.(2.2.7) can be written in the frequency domain:

$$\nabla^2 E(\mathbf{r},w) + \varepsilon(w)\frac{w^2}{c^2}E(\mathbf{r},w) = -\mu_0 w^2 FT\{(1+\frac{2i}{w_0}\frac{\partial}{\partial t})P_{NL}(\mathbf{r},t) - \frac{1}{w_0^2}\frac{\partial P_{NL}^2}{\partial t^2}\}, \tag{2.2.12}$$

where $\varepsilon(w) = 1+\chi^{(1)}(w)$ and $\chi^{(1)}(w)$ is the Fourier transform of $\chi^{(1)}(t)$.

With the method of separation of variables, we can assume a solution of the slowly varying part of the electric field $E(\mathbf{r},w)$ in frequency domain:

$$E(\mathbf{r},w) = F(x,y)A(z,w)exp(i\beta_0 z), \tag{2.2.13}$$

where $A(z,w)$ is a slowly varying function of z and $F(x,y)$ is the transversal dependence function.

When Eq.(2.2.9) is substituted in the third order of the induced nonlinear polarization Eq.(2.2.8), only non-resonant, incoherent nonlinear effects need to be considered since there is barely phase-matching satisfied for the third-harmonic generation and four-wave mixing. Then $P_{NL}(\mathbf{r},t)$ can be approximated as:

$$P_{NL}(\mathbf{r},t) = \varepsilon_0 \chi^{(3)} E(\mathbf{r},t) \int_{-\infty}^{t} R(t-t_1)|E(\mathbf{r},t)|^2 dt_1, \tag{2.2.14}$$

where it assumes that the electric field and the induced polarization vector point along the same direction and $\int_0^\infty R(t)dt = 1$.

In order to have the dispersion effect clearly, the mode-propagation constant $\beta(w)$ can be expanded in a Taylor series about the carrier frequency w_0 as:

$$\beta(w) = n(w)\frac{w}{c} = \beta_0 + \beta_1(w-w_0) + \frac{1}{2}\beta_2(w-w_0)^2 + \frac{1}{6}\beta_3(w-w_0)^3 + \ldots, \tag{2.2.15}$$

where

$$\beta_m = (\frac{d^m\beta}{dw^m})_{w=w_0} \quad (m = 0,1,2,\ldots). \tag{2.2.16}$$

The higher-order terms in this expansion are generally negligible if the spectral width $\triangle w \ll w_0$.

Substituting Eq.(2.2.13–2.2.15) into Eq.(2.2.12) and after some algebra:

$$\frac{\partial A}{\partial z} + \frac{\alpha A}{2} + \beta_1\frac{\partial A}{\partial t} + \frac{i\beta_2}{2}\frac{\partial^2 A}{\partial t^2} - \frac{\beta_3}{6}\frac{\partial^3 A}{\partial t^3} = i\gamma(1+\frac{i}{w_0}\frac{\partial}{\partial t})(A(z,t)\int_{-\infty}^{\infty} R(t')|A(z,t-t')|^2 dt'). \tag{2.2.17}$$

In Eq.(2.2.17) the nonlinear parameter γ is defined as:

$$\gamma = \frac{n_2 w_0}{cA_{eff}}, \tag{2.2.18}$$

where A_{eff} is the effective core area and n_2 is the nonlinear refractive index which is related to the real part of $\chi^{(3)}$. And if $A(z,t)$ is normalized with the units of $W^{\frac{1}{2}}$, n_2 is expressed in the units of m^2/W.

The first-order time derivative of P_{NL} on the right-hand side of Eq.(2.2.17) is responsible for self-steepening and shock formation at a pulse edge [20, 21] and this term also includes the nonlinear energy loss because of intrapulse Raman scattering.

When also considering the Raman contributions, the response function $R(t)$ includes both the electronic and vibrational parts which can be written as [19]:

$$R(t) = (1 - f_R)\delta(t) + f_R h_R(t), \tag{2.2.19}$$

where f_R is the fractional contribution to the delayed Raman response, $h_R(t)$ is Raman gain. For ultrashort however long enough to contain many optical cycles pulses, we can approximate Eq.(2.2.17) as:

$$\frac{\partial A}{\partial z} + \frac{\alpha A}{2} + \frac{i\beta_2}{2}\frac{\partial^2 A}{\partial T^2} - \frac{\beta_3}{6}\frac{\partial^3 A}{\partial T^3} = i\gamma(|A|^2 A + \frac{i}{w_0}\frac{\partial}{\partial T}(|A|^2 A) - T_R A\frac{\partial |A|^2}{\partial T}), \tag{2.2.20}$$

where group velocity v_g is used by making the transformation:

$$T = t - \frac{z}{v_g} = t - \beta_1 z. \tag{2.2.21}$$

The term proportional to β_3 is responsible for the third-order dispersion which is important for the ultrashort pulses because of their wide bandwidth. This effect can explain the pulse compensation in chapter 4 and 5; the term proportional to w^{-1} is responsible for the pulse self-steepening and shock formation; and the last term proportional to T_R indicates the delayed Raman response and is responsible for the self-frequency shift. The last two terms normally can be neglected in the fiber laser cavities mentioned in this thesis excepted for the high power amplifier described in chapter 7.

2.3 Analytical Solutions

2.3.1 Dispersion

GVD is the phenomenon of group velocity depends on the optical frequency w through the frequency dependence of the refractive index $n(w)$. In Eq.(2.2.15),

$$\beta_1 = \frac{1}{v_g} = \frac{n_g}{c} = \frac{1}{c}(n + w\frac{dn}{dw}), \tag{2.3.1}$$

$$\beta_2 = \frac{1}{c}(2\frac{dn}{dw} + w\frac{d^2 n}{dw^2}), \tag{2.3.2}$$

where β_2 is the GVD parameter. In the fiber-optics, dispersion parameter D is commonly used by the relation to β_2

$$D = \frac{d\beta_1}{d\lambda} = -\frac{2\pi c}{\lambda^2} \approx \frac{\lambda}{c}\frac{d^2 n}{d\lambda^2}, \tag{2.3.3}$$

which is contributed to the fiber material and the structure of the waveguide.

To illustrate the effects of dispersion on a pulse, a simple analytical calculation can be done if all other terms in Eq. (2.2.20) but the group velocity dispersion are neglected:

$$\frac{\partial A}{\partial z} = -\frac{i\beta_2}{2}\frac{\partial^2 A}{\partial T^2} + \frac{\beta_3}{6}\frac{\partial^3 A}{\partial T^3}. \tag{2.3.4}$$

If only GVD is considered, a initial transform-limited Gaussian pulse with FWHM T_{FWHM} is assumed:

$$A(0,t) = A_0 exp(-2ln(2)(\frac{t}{T_{FWHM}})^2). \tag{2.3.5}$$

After propagation through a fiber of length L, only considering the second-order dispersion β_2, the output can be calculated from Eq.(2.3.4) as:

$$A(L,t) = A_0 \frac{T_0}{(T_0^2 - I\beta_2 L)^{1/2}} exp(-\frac{T^2}{2(T_0^2 - I\beta_2 L)}), \tag{2.3.6}$$

where

$$T_0 = T_{FWHM}/[2(ln2)^{1/2}]. \tag{2.3.7}$$

Thus the Gaussian pulse still maintains its shape but its pulse duration has increased as:

$$T(L) = T_0[1 + (|\beta_2|L/T_0)^2]^{1/2}, \tag{2.3.8}$$

which also shows that the spectrum frequency changes linearly across the pulse while the power spectrum keeps the same:

$$A(L,w) = exp(i\frac{\beta_2}{2}L(w - w_0)^2)A(0,w). \tag{2.3.9}$$

Figure 2.1 shows the pure GVD temporal broadening of a 30 fs unchirped Gaussian pulse propagating through an optical fiber with dispersion 40 $ps/(nm \cdot km)$.

In order to avoid the pulse temporal broadening caused by GVD, dispersion compensation can be applied. Dispersion compensation consists of combining fibers with different characteristics so that the total average GVD of the entire fiber link is quite low. When the average GVD is set to zero, dispersion is totally compensated. If a fiber link consists of two types of fibers with dispersion D_1 and D_2, length L_1 and L_2 respectively. The condition for dispersion compensation can be written as:

$$D_1 L_1 + D_2 L_1 = 0. \tag{2.3.10}$$

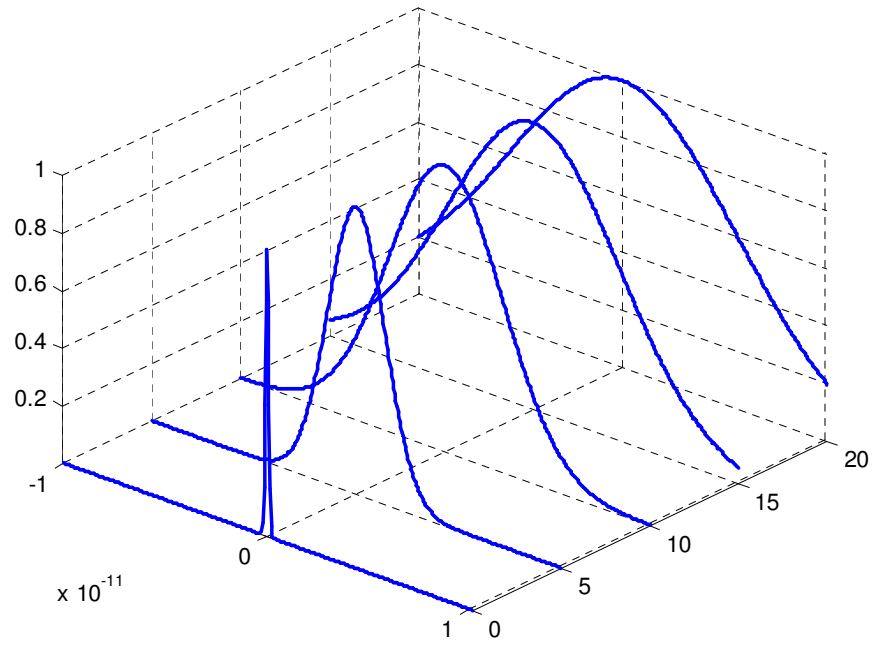

Figure 2.1: Dispersion induced temporal broadening of a Gaussian pulse inside a fiber with dispersion 40 $ps/(nm \cdot km)$.

Normally it does not need to consider high order dispersion part in Eq.(2.3.4) but in ultrashort pulse generation, higher order dispersion will be the major limitation [22]. Figure 2.2 shows evolution of an unchirped super-Gaussian pulse at the zero-dispersion wavelength and it is clear that pulse shapes can vary widely depending on the initial conditions. In this case, for a fiber link consists of two types of fibers with length L_1 and L_2, the conditions for broadband dispersion compensation are given by:

$$\beta_{21}L_1 + \beta_{22}L_2 = 0 \ \ and \ \ \beta_{31}L_1 + \beta_{32}L_2 = 0, \tag{2.3.11}$$

where β_{2j} and β_{3j} are the GVD and TOD parameters for fiber of lengh $L_j (J = 1, 2)$. However, for a pulse with broadband spectrum, it is generally difficult to satisfy both conditions simultaneously. That's why it is not easy to get an transform-limited pulse by monolithic fiber lasers.

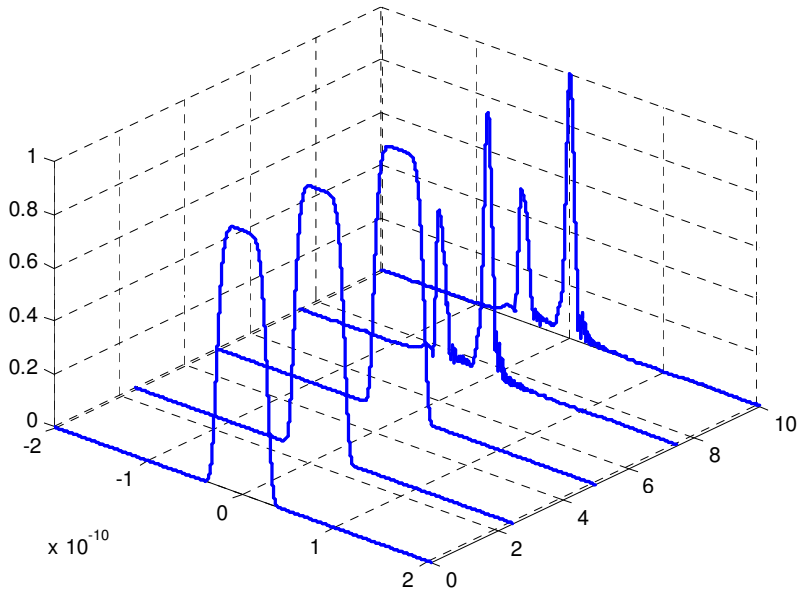

Figure 2.2: Evolution of a super-Gaussian pulse along the fiber length for the case of $\beta_2 = 0$ and $\beta_3 > 0$. TOD is responsible for the oscillaroty structure near the edge of the pulse.

2.3.2 Self Phase Modulation

For pulses propagating in optical fibers, one of the most important nonlinear effect is SPM which leads to spectral broadening. SPM is the temporal analog of self-focusing and was first observed in 1967 by Fujio Shimizu [23]. The earliest observation of SPM in optical fibers was appeared in 1974 [24].

To illustrate the effects of SPM, all the other terms in Eq. (2.2.20) are neglected again:

$$\frac{\partial A}{\partial z} = i\gamma |A|^2 A. \tag{2.3.12}$$

After propagation in the optical fiber of length L, the output can be calculated as:

$$A(L,t) = exp(i\gamma L|A(0,t)|^2)A(0,t). \tag{2.3.13}$$

If consider the initial pulse as an transform-limited Gaussian pulse described in

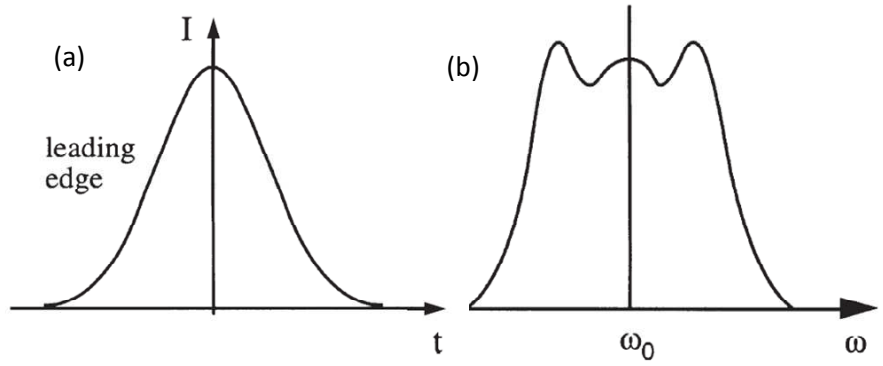

Figure 2.3: (a) The output temporal shape after SPM with initial an unchriped Gaussian pulse. (b) The output broadening spectrum due to SPM with initial an unchriped Gaussian pulse.

Eq.(2.3.5) again, from Eq.(2.3.13) we can see that nothing would happen to the temporal shape of the pulse as shown in Figure 2.3 (a) but the phase chirp is no longer linear temporal dependence. So the spectrum is no longer Gaussian and is spectrally broadened as shown in Figure 2.3 (b). Since the chirped phase is power dependent, the shape of the SPM broadened spectrum depends on the initial pulse shape and the initial pulse chirp.

2.3.3 Combination of Dispersion and SPM

When pulse propagating through an optical fiber, new qualitative features arise from an interplay between GVD and SPM. Eq. (2.2.20) can be written as:

$$\frac{\partial A}{\partial z} = -\frac{i\beta_2}{2}\frac{\partial^2 A}{\partial T^2} + i\gamma|A|^2 A. \tag{2.3.14}$$

When an initially unchirped Gaussian pulse in the normal-dispersion regime ($D > 0$), the qualitative behavior is quite different from the expected when either GVD or SPM dominates. Particularly, the pulse broadens much more rapidly compared with SPM neglected. This can be understood by noting that SPM generates new frequency components that are red-shifted near the leading edge while the bule-shifted near the trailing edge. As the low frequency part travel faster than the high frequency part in the normal dispersion regime, SPM leads to an enhanced rate of the pulse broadening.

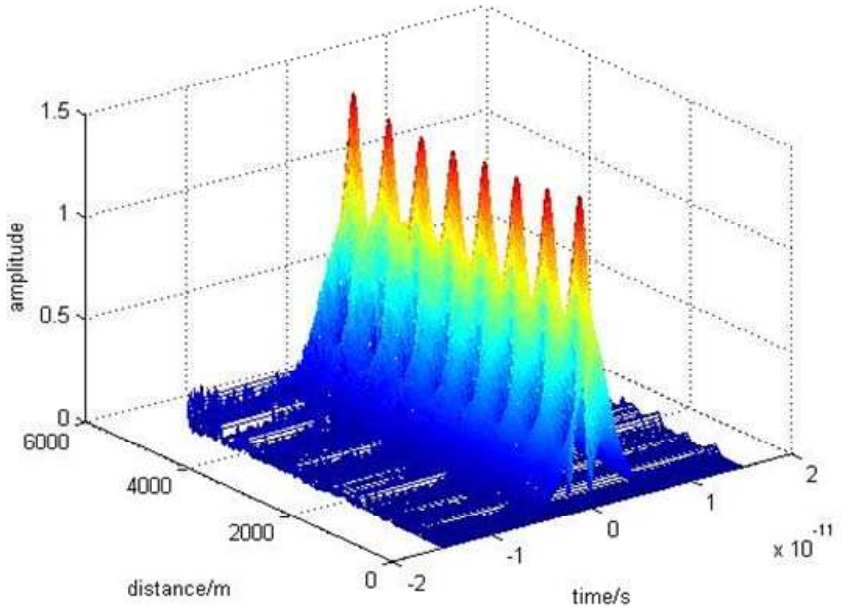

Figure 2.4: One second-order soliton induced by the interplay anomalous GVD and SPM.

The situation is different for the pulse propagating in the anomalous dispersion regime($D < 0$). Still consider an unchirped Gaussian pulse as the initial input pulse, the pulse broadens first at a rate much slower than that expected with the GVD only and then appears to reach a steady state. At the same time, the spectrum narrows rather than exhibiting broadening expected by SPM alone. This can be understood by noting that the SPM induced chirp is positive while the dispersion induced chirp is negative in the anomalous dispersion regime. When the two chirp contributions cancel each other, the pulse shape can adjust itself during propagation through the fiber. This situation is called as soliton. The fundamental soliton is a solution of Eq. 2.3.14 which perserves both the temporal and spectral shape when propagating in the fiber. The fundamental soliton occurs when nonlinearities are exactly balanced by dispersion in the fiber which is characterized by a very characteristic sech shape:

$$|A(z,t)| = (\frac{|\beta_2|}{\gamma t_0^2})^{1/2} sech(t/t_0.) \tag{2.3.15}$$

High-order solitons are various combinations of the eigenvalues and residues of Eq.2.3.14. Figure2.4 shows an example of second-order soliton propagating through an optical fiber due to the combination of anomalous GVD and SPM.

2.3.4 Nonlinear Polarization Rotation

For high birefringence or PM fiber, there are two orthogonally polarized states and the mode-propagation constant β becomes slightly different in the x and y directions. The strength of modal birefringence is defined as:

$$B_m = \frac{|\beta_x - \beta_y|}{k_0} = |n_x - n_y|. \tag{2.3.16}$$

And beat length can be written as:

$$L_B = \frac{2\pi}{|\beta_x - \beta_y|} = \frac{\lambda}{B_m}. \tag{2.3.17}$$

If a general elliptically polarized pulse is launched into a fiber or a linear polarized light is launched into a high birefringence or PM fiber with an angle to the orthogonally polarized states, and when the nonlinearities are present, it will experience the NPR.

Consider an electric field consisting of a single frequency, i.e.

$$\mathbf{E} = \frac{1}{2}\{(1_x E_x + 1_y E_y)e^{-iw_0 t}\}, \tag{2.3.18}$$

and then the induced third order polarization along the x-axis is:

$$P_x = \epsilon_0 \frac{3}{4}[\chi^3_{xxxx} E_x E_x^* E_x + \chi^3_{xxyy} E_x E_y^* E_y + \chi^3_{xyyx} E_y E_y^* E_x + \chi^3_{xyxy} E_y E_x^* E_y]. \tag{2.3.19}$$

Assuming that the fiber is linearly birefringent which means that the two principle axes long which linearly polarized light remains linearly polarized in the absence of nonlinear effect. We can get:

$$P_x = \epsilon_0 \frac{3}{4}\chi^3_{xxxx}[(|E_x|^2 + \frac{2}{3}|E_y|^2)E_x + \frac{1}{3}(E_y^2 E_x^*)], \tag{2.3.20}$$

$$P_y = \epsilon_0 \frac{3}{4}\chi^3_{xxxx}[(|E_y|^2 + \frac{2}{3}|E_x|^2)E_y + \frac{1}{3}(E_x^2 E_y^*)]. \tag{2.3.21}$$

From Eq.(2.3.20) and (2.3.21), the nonlinear refractive index along the x and$y$ axis can be evaluated. Along the x-axis, the nonlinear refractive index equals:

$$\Delta n_x = n_2\{|E_x|^2 + \frac{2}{3}|E_y|^2\}, \tag{2.3.22}$$

and it is similar for Δn_y by exchange index x and y in the expression of Δn_x. The example of NPR is shown in Chapter 7.

2.3.5 Raman Effect

The raman effect originates from inelastic scattering on the optical phonos in the fiber. The process of Raman scattering may be described as a dipole that is excited through the pump wave interacting with phonons [25]. More specifically, the bound electrons oscillate at the optical frequency of the excitation. This induced oscillating dipole moment produces optical radiation at the same frequency as the incident optical field while the molecular structure itself is also oscillating. Therefore the induced oscillating dipole moment also contains the sum and difference frequency between the optical and vibrational frequencies and these new frequencies are the Raman scattered light. Physically, the radiated power from the dipole is recaptured by the fiber.

Raman effect effectively corresponds to a gain on the red side of the pulse and for a silica fiber, the peak of this Raman gain is centered at about 13.2 THz from the central wavelength of the pulse. Starting from the noise, a new pulse will start to build up at Raman wavelength and will eventually drain most of the energy from the original pulse. This is referred as SRS. The created pulse is called 1th Stokes pulse and when its peak power strong enough, the 2nd Stokes pulse will be generated, and so on. SRS is shown in the high power amplifier output described in Chapter 7.

Since SRS is dependent on the input pulse peak power, fiber length, transmission loss, etc., a peak power threshold can be calculated [26]:

$$P^{th} \approx \frac{16A_{eff}}{gL}\frac{\alpha L}{1-e^{-\alpha L}}, \tag{2.3.23}$$

where A_{eff} is the effective area of the fiber, g is the Raman gain around $10^{-13}m/W$, α is the power loss per unit length and L is the fiber length. P^{th} is relatively high for mode locking lasers with short fiber length and only high power lasers or amplifiers can observe SRS.

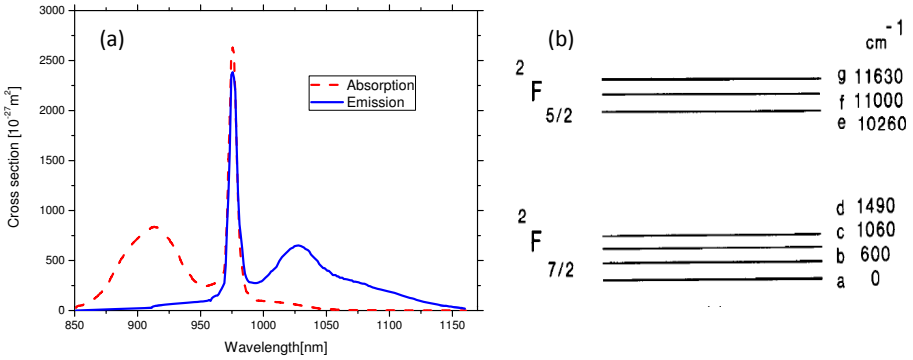

Figure 2.5: (a) The absorption and emission cross section for Yb^{3+}-doped silica. (b) Energy band diagrams of ytterbium.

2.3.6 Gain

All the fiber lasers mentioned in this thesis are based on ytterbium doped fibers as the gain medium. After the first report in 1962 of laser action in Ytterbium-doped silicate glass [27], $Yb3+$ has attracted relatively little interest as a laser-active ion. It has been overshadowed by the $Nd3+$ ion with its important advantage of a four level transition, whereas Yb3+ has only three level and quasi-three level transitions, see in Figure2.5 (b). In fact, the most important role of the $Yb3+$ ion has so far been as a sensitizer ion, absorbing pump photons over a wide spectral range and then transferring the excitation to an acceptor ion which then acts as the laser-active ion. So it has attracted more and more interest now by virtue of its amplification over the very broad wavelength range from 975 to 1200 nm. Figure 2.5 (a) shows the absorption and emission cross section of ytterbium.

Apart from their broad-gain bandwidth, Yb-doped fiber amplifiers can also offer high output power and excellent power conversion efficiency. Many of the complications which are well-known from erbium-doped amplifiers are avoided: excited state absorption and concentration quenching by interionic energy transfer do not occur, and high doping levels are possible, leading to high gain in a short length of fiber [28].The broad bandwidth is ideal for the amplification of ultrashort pulses, and the high saturation fluency allows for high pulse energies. There is also a wide range of possible pump wavelengths (860 nm 1064 nm), allowing a variety of pumping schemes, including the use of diode lasers or even high-power Nd lasers.

For short piece of Yb-doped fiber, the pump and laser intensity profiles are

regarded to be uniform over the area A of the core and a uniform Yb dopant distribution within the core. Steady-state conditions are also assumed. The total populations of the ${}^2F_{5/2}$ and ${}^2F_{7/2}$ manifolds are designated N_1 and N_2, respectively [29]. The total population N is:

$$N = N_1 + N_2, \tag{2.3.24}$$

which corresponds to a small-signal absorption. In our experiments, the small-signal absorption at a pump wavelength of 976 nm is around 300 dB m^{-1}.

And the total gain of the active fiber is given by [30]:

$$G(w) = exp\{(\sigma_e(w)N_2 - \sigma_a(w)N_1)L_g\}, \tag{2.3.25}$$

where $\sigma_a(w)$, $\sigma_e(w)$ are the absorption and emission cross section of Yb respectively, L_g is the amplifier length. For a quick calculation of pulse shapes and double-pulse thresholds the level populations N_1 and N_2 are relaxed according to the formula [30]:

$$N_2 = \frac{N_t}{2 + \bar{E}_p/E_{sat}}, \tag{2.3.26}$$

where E_{sat} is a model parameter controlling the equilibrium pulse energy and $\bar{E}_p$ is the pulse energy averaged over the entry and exit points of the amplifier. When the pump power is assumed to be fully absorbed by the Yb-doped fiber, the evolution of N_2 can be written as:

$$\frac{dN_2}{dt} = \frac{P_p}{\hbar w_p A_{eff} L} - \frac{N_2}{\tau}, \tag{2.3.27}$$

where w_p is the pump frequency, A_{eff} is the amplifier effective area, τ is the Yb spontaneous-emission lifetime. The effective mode field diameter Yb-doped fiber used in our experiments is around 6 um [31]. The lifetime of the upper level typically is around 0.8 ms varied by about 30% [29]. The pump frequency is 976 nm.

In the absence of the nonlinearity, the gain and output spectrum can be calculated when knowing the input pulse spectrum (green line in Figure 2.6). The shape of output spectrum changes little. However, for short pulse amplified by Yb-doped fiber, the nonlinear effects has to be considered.

Figure 2.7 shows the amplification of unchirped input pulse and the spectrum broadening is significant due to SPM induced by high peak power. Figure 2.8 shows the amplification of the chirped pulse after propagation 5.7 m PM PANDA fiber

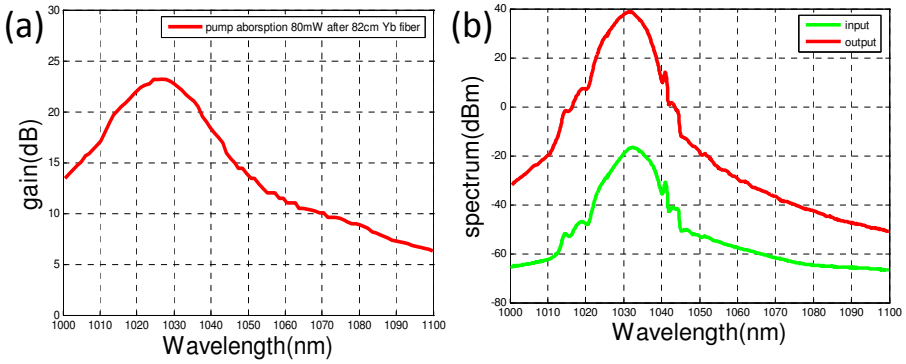

Figure 2.6: (a) the calculated gain of 82cm Yb fiber. (b) green line is the experimental input pulse spectrum, red line is the calculated output spectrum after 82cm Yb fiber in the absence of nonlinear effects.

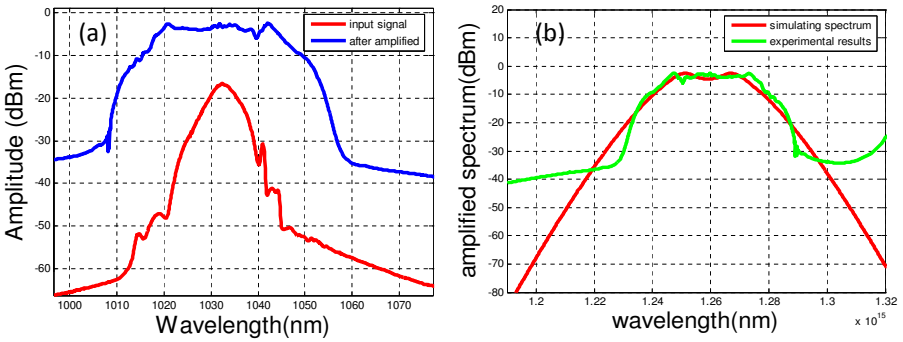

Figure 2.7: (a) the experimental results after stretching and then amplified, red line - input laser spectrum, blue line - amplified spectrum. (b) Simulating result comparing with experimental results.

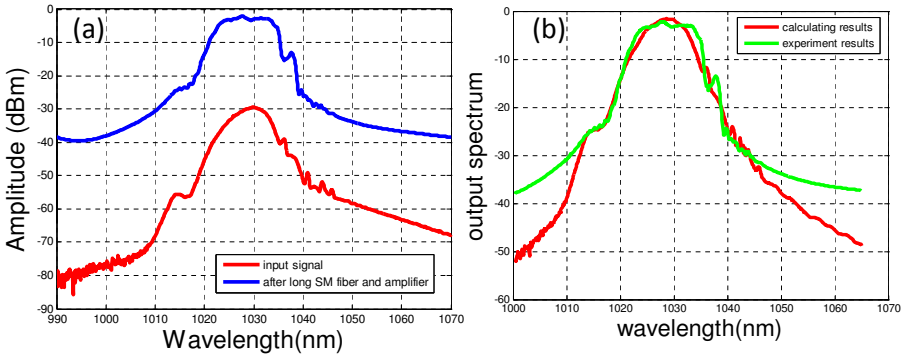

Figure 2.8: (a) the experimental results, red line - input laser spectrum, blue line - amplified spectrum. (b) Simulating result comparing with experimental results.

with dispersion at 1030nm around -35ps/nm/km. The difference comparing with Figure 2.7 is that when propagating throng the 5.7 m PM PANDA fiber, the pulse is temporal broadened due to the normal fiber dispersion and when amplified with same pump power, its nonlinear effects get much smaller.

2.3.7 Numerical Methods

The GNLSE [Eq.(2.2.20)] can't get analytic solutions except for some specific cases because it is a nonlinear partial differential equation. So numerical approach is needed for understanding of the pulses propagation in optical fibers. The one method used in this thesis is the split-step Fourier method. Eq.(2.2.20) can be written by separate the linear and nonlinear effects into two parts:

$$\frac{\partial A}{\partial z} = (\hat{D} + \hat{N})A, \tag{2.3.28}$$

where $\hat{D}$ accounts for the linear effects such as dispersion and absorption and $\hat{N}$ accounts for the nonlinear effects such as SPM and so on.

First of all, the optical fiber length L for the pulses propagation can be divided into N short segments of width l, which is $L = Nl$. The split-step Fourier method assumes that when propagating in the optical fiber over one segment l, the linear and nonlinear effects can be pretended to act independently – the linear effect acts alone for the fist $l/2$ and nonlinear effect acts alone for the followed $l/2$. Figure2.4

is an simple example result of the split-step Fourier method.

2.4 Mode-Locking Mechanisms

As mentioned in chapter 1, there are two kinds of mode-locking mechanisms: active mode-locking and passive mode-locking. Active mode-locking is an external modulation to the laser cavity. It can be realized by either of the cavity losses (by inserting an acousto-optical crystal inside the cavity, for instance) or of the gain of the amplifying medium (for example by pumping this medium with another mode-locked laser). Such an electronically driven loss modulation produces a sinusoidal loss modulation with a period given by the cavity round trip time [32]. The saturated gain at steady state then only supports net gain around the minimum of the loss modulation and only supports pulses that are significantly shorter than the cavity round trip time. Passive mode-locking is obtained from a SA [22] which can be either the insertion of a real saturable absorbing medium into the cavity [22] or created by the mode-locking mechanism i.e. KLM and NPR [33] in order to select one single pulse. In order to make the mode-locking self-starting, the following conditions are needed [11]:

The pulsed regime should be favored over the continuous regime; The overall system should possess the property of pulses shortening; There should be mechanism to initiate the mode-locking process.

In this thesis, only passive mode-locking mechanisms are considered.

2.4.1 Nonlinear Polarization Rotation

One widely designed mode-locking lasers is to use NPR in conjunction with a polarizer [34, 35]. By controlling the polarization state in the fiber e.g. with a set of wave-plate, the transmission power through the polarizer will be power dependent and when the transmission increasing at increasing the peak power, the mode-locking can be obtained. For a more extensive overview of mode-locking lasers with NPR see e.g. [36, 37, 38]. One example of NPR is shown in chapter 7.

2.4.2 SESAM

SESAM is a saturable absorber that operates in reflection and the reflectivity increases with higher incoming pulses [32]. SESAMs are now both commercially [39] and fundamental [40] available for mode-locking lasers.The mode-locking lasers described in chapter 4 and 5 are based on SESAM mode-locking.

A SESAM consists of a Bragg-mirror on a semiconductor wafer like GaAs, covered by an absorber layer and a more or less sophisticated top film system, determining the absorption. The saturable absorber layer consists of a semiconductor material with a direct band gap slightly lower than the photon energy [39]. In general, GaAs/AlAs is used for the Bragg mirrors and InGaAs Quantum Wells for the saturable absorber material. during the absorption, electron-hole pairs are created in the film. As the number of photons increases, more electrons are excited, however only a certain number of electron-hole pairs can be created which induce the absorption saturating. The electron-hole pairs recombined non-radiatively and after a certain period of time, SESAM are ready to absorb photons again. The key parameters for a saturable absorber are its dynamic response - recovery time, wavelength range, saturation intensity, modulation depth and the non-saturable losses.

The modulation depth ΔR and non-saturable losses ΔR_{ns} in reflectivity are defined as [41]:

$$\Delta R = R_{ns} - R_{lin}, \tag{2.4.1}$$

and

$$\Delta R_{ns} = 1 - R_{ns}. \tag{2.4.2}$$

Here, R_{lin} is the linear reflectivity for pulse with zero pulse energy fluence and R_{ns} is the reflectivity for infinitely high pulse energy fluences when all saturable absorption is bleached. R_{lin} and R_{ns} are not experimentally accessible but can be extrapolated from the measure data using a proper model function. The SESAM modulation depth used in the fiber lasers in this thesis is around 0.24.

The saturation fluence F_s is the fluence required to begin absorption saturation. For an infinitely thin absorber, the reflectivity for a pulse with fluence $F_p = F_s$ is increased by $1/e$ of ΔR with respect to R_{lin}, where F_p is the incident pulse energy per unit surface area. In our case, $F_s = 70\,uJ/cm^2$.

The action of the SESAM is normally described in the time domain, according

to equations [30]:

$$A(t) \rightarrow A(t)\sqrt{1 - A_0 - N_1^s(t)\sigma_s} \tag{2.4.3}$$

and

$$\frac{dN_1^s}{dt} = -\frac{dN_2^s}{dt} = \frac{N_2^s}{\tau_s - \frac{N_1^s |A(t)|^2}{A_{eff}^s F_s}}, \tag{2.4.4}$$

where N_1^s, N_2^s are the per area concentrations in the ground and excited states respectively, σ_s is the absorption cross section, τ_s is their relaxation time and A_0 is the unsaturable absorption. $A(t)$ has been normalized so that $|A(t)|^2$ corresponds to the instantaneous pulse power. A_{eff}^s is an effective focusing area of the laser spot on the sesam. F_s denotes the saturation fluence. The parameters σ_s and $N_0^s = N_1^s + N_2^s$ can be calculated from the saturation fluence and saturable absorption, ΔR, of SESAM according to

$$\sigma_s = \frac{\hbar w_0}{F_s}, \;\; N_0^s = \frac{\Delta R}{\sigma_s}. \tag{2.4.5}$$

The low value of τ_s implies that the reflectivity of SESAM can be describes by:

$$R_s(t) = 1 - A_0 - \frac{\Delta R}{1 + P(t)/P_{sat}}, \;\; P_{sat} = \frac{F_s A_{eff}^s}{\tau_s}. \tag{2.4.6}$$

Chapter 3

Characterization Techniques

This chapter describes some technics developed for characterization of PM fiber and ultrafast fiber lasers. First of all, the fiber dispersion measurement was demonstrated. This setup was used to measure all the fibers used in the fiber lasers described in Chapter 4 and 5. It can not only measure the pure fiber dispersion but also other dispersions, for example, the dispersion of fiber injected with liquid crystal. The noncollinear intensity autocorrelation was also introduced in this chapter which is one of the most useful methods for pulse duration characterization in our work. Finally, the concept of FROG is also discussed and this can tell us more information of ultrashort pulses.

3.1 Fiber Dispersion Measurements

3.1.1 Introduction

As mentioned in Chapter 2, fiber dispersion originates from the variation of refractive index of an optical fiber as a function of wavelength. The knowledge about dispersion of a fiber is key important for the mode-locking fiber laser design since it influences the pulse propagation in the fiber.

The fiber dispersion can be measured in several ways. The classical pulse-delay method measures the differential-mode delays of optical pulses with various wavelength [42]. Though this is simple and inexpensive, the temporal pulse broadening

through fiber makes it difficult to accurately determine the arrival time of the pulse and the measurements accuracy degrades. The commercial available systems for the telecommunication industry use the differential phase shift method, where light from a broadband light source is intensity modulated at high frequency and sent through a long sample of an optical fiber [43]. Even though the commercial is a stand technique adapted in most of fiber manufacturing companies, it is restricted in our experiments. It requires a complicated experimental setup and expensive equipment such as a high-speed optical modulator and an optical tunable filter. The most important is that it can not measure the dispersion of a short fiber sample which is the case in our setup. A temporal white-light interferometry and a spectral white-light interferometry method have been used for measuring the dispersion of short fibers [43] by using a standard Michelson or Mazh-Zehnder interferometer. In a temporal white-light interferometry method, the cross correlation interferogram is Fourier transformed to obtain phase information about the different spectral components present in a broadband source [44]. This method can measure the dispersion value for a short piece optical fiber and for other optical devices such as photonic crystal fibers, fiber Bragg gratings and arrayed waveguide gratings. This method needs a very high stability over the rather long recording time and is very sensitive to external effects such as temperature and air fluctuations. The resulting additional noise in a measured interferogram decreasing its accuracy [45]. A spectral white-light interferometry method combined with an optical broadband source and a spectrometer can be used to obtain the spectral interferogram without involving any moving components. This accurate and reliable method for obtaining an interferogram has been used in various applications [44, 46]. This is what we used for our fiber dispersion. It should be noted that careful experimental conditions need to be satisfied to obtain a stationary phase point or a central zeroth-order fringe point when the refractive index or the dispersion of a fiber is measured with this method.

3.1.2 Experimental Setup and Theory

Figure 3.1 shows a diagram of the experimental setup. The configuration was based on a fiber Mach-Zehnder interferometer with a broadband light source and an OSA. A SLD is used as the broadband source with a central wavelength of 1055 nm and FWHM of 50 nm. Except for the tested fiber, all the fibers in this setup are PM PANDA fibers. The first 50/50 fiber is used to split light into two different paths. The tested fiber is spliced to one arm of the interferometer. Both arms have free space propagation with two fiber collimators. The half wave plate and polarizer

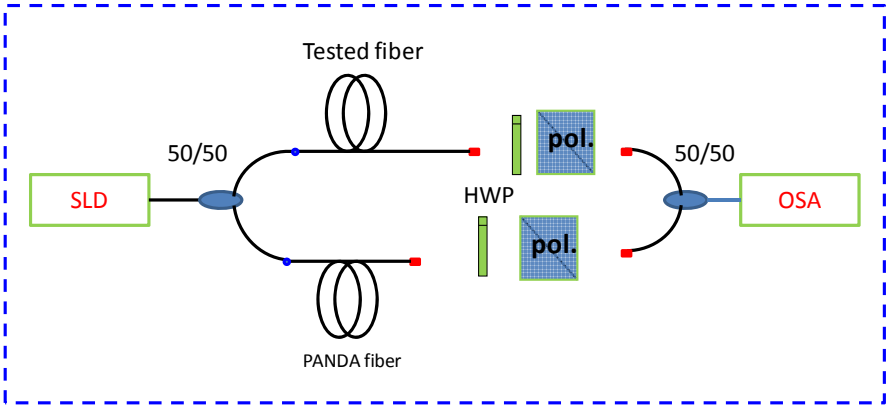

Figure 3.1: Experimental layout for the chromatic dispersion measurement of an optical fiber. All the fibers in the setup are PM fibers.

are used to control the light power and polarization direction in order to get the maximum visibility in an interferometric fringe pattern. The length of one free space delay line can be adjusted by a translating stage driven with a micrometer on which a fiber collimator was mounted as shown in Figure 3.2 and 3.3. The modulation period in the measured interferogram can be varied by changing path length in the reference arm. Two transmitted optical signals are combined to form a cross-correlation interferogram. The optical interference signal in the spectral domain was measured with an OSA.

The measured spectrogram contains the spectral phase information of a sample as a function of optical frequency which can be written as [46]:

$$\langle I(f)\rangle = \langle |E(f)|^2\rangle + a^2\langle |E(f)|^2\rangle + 2a\langle |E(f)|^2\rangle cos(\psi(f)), \tag{3.1.1}$$

where $\langle\rangle$ denotes an ensemble average, f is optical frequency, $\langle |E(f)|^2\rangle$ is the spectral intensity, a^2 is relative optical power for the transmitted optical signal trough the test fiber, $\psi(f)$ is relative phase between a reference signal and a transmitted signal through a tested fiber. $a^2 = 1$ is realized by adjusting the half wave plates in both arms. the relative phase ban be expressed as:

$$\psi(f) = \beta(f) \cdot L - \beta_0 \cdot L_0, \tag{3.1.2}$$

where $\psi(f)$ is the propagation constant of transmitted light in a tested fiber, L is the length of tested fiber, β_0 is the propagation constant in vacuum and L_0 is the

length of reference arm.

$$\beta(f) = \frac{2\pi}{c} n(f) f, \tag{3.1.3}$$

and

$$\beta_0 L_0 = \frac{2\pi}{\lambda} L_0 = 2\pi\tau_0 f, \tag{3.1.4}$$

where λ is the wavelength corresponding to frequency f and τ_0 is the delay time associated with the reference arm of an interferometer which is defined as $\tau_0 = L_0/c$. τ_0 can be controlled by adjusting a translation stage in the reference arm. The relative phase can be calculated as:

$$\phi(f) = \beta(f)L - 2\pi\tau_0 f. \tag{3.1.5}$$

The derivation of the relative phase with respect to optical frequency can be expressed as:

$$\frac{1}{2\pi}\frac{d\phi(f)}{df} = \tau_g(f) - \tau_0, \tag{3.1.6}$$

where $\tau_g(f)$ is the group delay after transmitting through the tested fiber. $\tau_g(f)$ can be calculated as:

$$\tau_g(f) = \frac{L}{v_g(f)} = \frac{L}{2\pi}\frac{d\beta(f)}{df}, \tag{3.1.7}$$

where $v_g(f)$ is the group velocity of light in the tested fiber.

The chromatic dispersion coefficient $D(\lambda)$ is the variation in the group delay with respect to wavelength per unit length of a fiber and can be written as:

$$D(\lambda) = \frac{1}{L}\frac{\partial\tau_g(\lambda)}{\partial\lambda}. \tag{3.1.8}$$

In our experiments, the phase $\phi(f)$ is directly retrieved from the spectral interferogram $\langle I(f)\rangle$ and then the group delay and fiber dispersion can be calculated.

3.1.3 Experimental Results

Figure 3.2(b) shows a measured spectral interference pattern for PM PANDA fiber which is the normalized spectral interferogram obtained by the OSA. From Eq. (3.1.1), the phase difference between adjacent positive fringe peaks becomes 2π. All

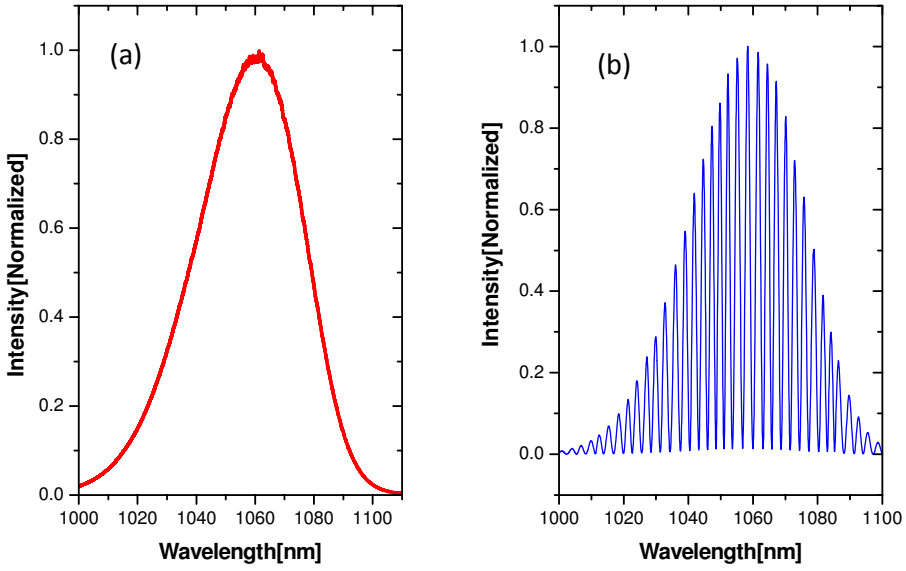

Figure 3.2: (a) Input light source. (b) A measured spectral interferogram of PANDA fiber by an OSA.

peak positions were calculated directly from the spectral fringe interferogram. After finding the wavelength of each positive oscillation peak, a discrete relative phase function $\phi(\lambda)$ with respect to wavelength was generated. Afterwards, the calculated relative phase function was converted from the wavelength into frequency to obtain $\phi(f)$. A cubic spline fitting process is used to calculate a regularly spaced phase function in the frequency. A least square algorithm for a simple 3rd order Taylor expansion is used for fitting the phase curve:

$$\phi(f) = 2\pi(\phi_0 + \phi_1 f + \frac{1}{2}\phi_2 f^2 + \frac{1}{6}\phi_3 f^3), \tag{3.1.9}$$

in which the group delay is proportional to the first derivative of the calculated phase shift and dispersion is dependent on the second derivation. Then the relative phase function can be written as:

$$\tau_g(f) \approx \tau_0 + \phi_1 + \phi_2 f + \frac{1}{2}\phi_3 f^2. \tag{3.1.10}$$

The zero-dispersion frequency f_0 is the frequency at which the group delay is

minimum and can be calculated to be:

$$f_0 = -\frac{\phi_2}{\phi_3}. \tag{3.1.11}$$

When replace f with c/λ in Eq. 3.1.10 and take the first order derivative with respect to λ, the dispersion of tested fiber has the expression as:

$$D(\lambda) \approx -\frac{c}{L}\left(\frac{\phi_2}{\lambda^2 + \frac{c\phi_3}{\lambda^3}}\right). \tag{3.1.12}$$

The purple line in Figure 3.4 shows the chromatic dispersion of PM PANDA fiber obtained with the proposed method. The measurement result has a good agreement with those of the conventional measurement method.

The dispersion of photonic crystal fibers are also measured. Figure 3.3 (a) is the normalized spectral interferogram of HC-PCF fiber (see in Figure 1.2 (a)) and Figure 3.3 (b) is the close-up view of 3.3 (a) near 1055 nm wavelength. The calculated dispersion of HC-PCF is the red line in Figure 3.4. Figure 3.3 (c) is the normalized spectral interferogram of SC-PBG fiber (see in Figure 1.2 (b)) and the blue line in 3.4 is the measured dispersion.

3.2 Pulse Duration Measurements

The characterization of the temporal profile of the laser pulse including intensity and phase is the basis of any measurements in ultrashort pulse laser techniques [11]. As ultrashort pulses are much faster than the photoelectric response time, the photo diodes can not resolve the temporal shape of the pulse, an alternative approach has to be taken. The temporal duration of a pulse can be retrieved by correlation function, and most conveniently from the interference with itself which is called as autocorrelation. The setup for this measurement is known as autocorrelator and the output as an autocorrelation trace. Though autocorrelation measurements can easily tell us the intensity of the pulse, for more understanding, FROG is introduced for pulse characterization.

3.2.1 The Intensity Autocorrelation

The intensity autocorrelation $A^2(\tau)$ is an attempt to measure the pulse's intensity vs. time [47]. It is what results when the pulse is interfered with itself in the

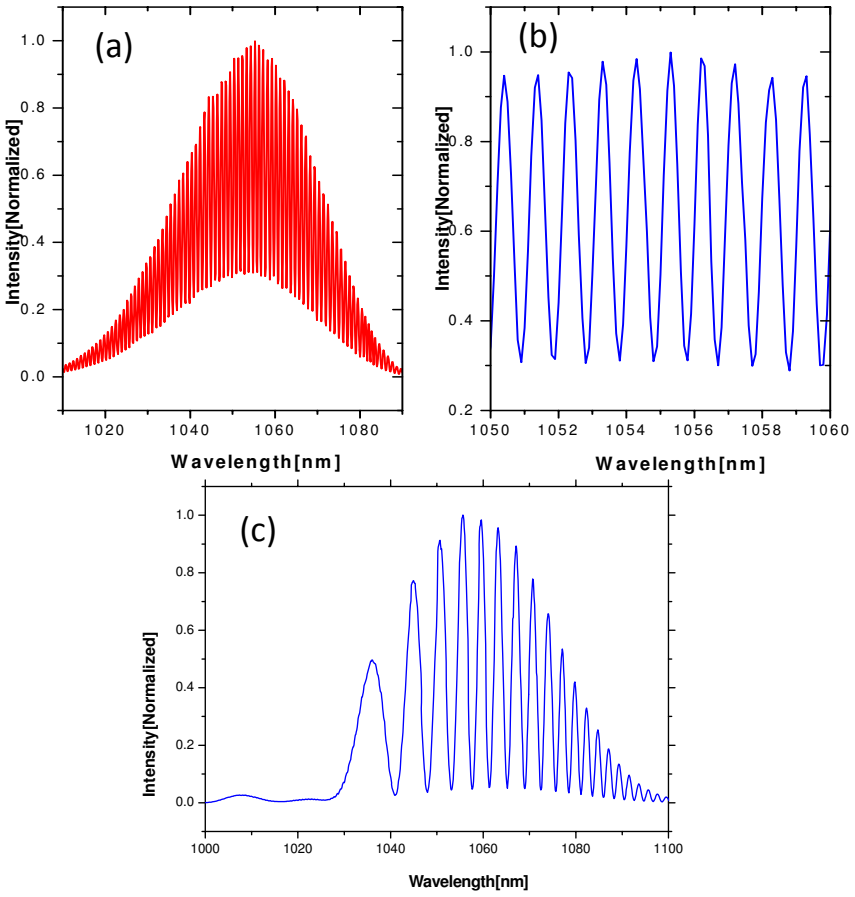

Figure 3.3: (a) A measured spectral intergerogram of HC-PCF obtained by an OSA. (b) the close-up view of (a) at about 1055 nm wavelength. (c) A measured spectral interferogram of SC-PBG fiber obtained by an OSA.

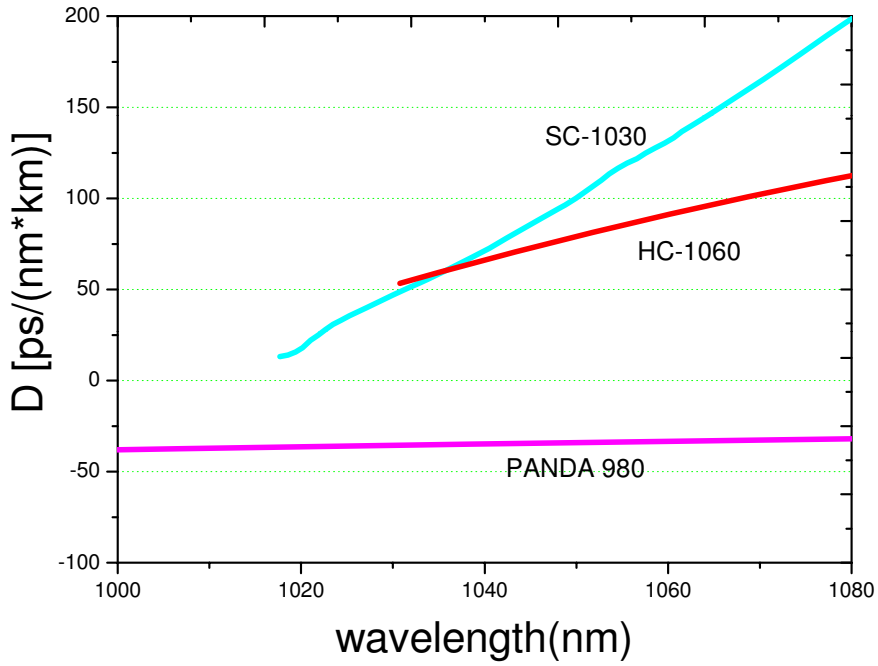

Figure 3.4: The calculated chromatic dispersion of PANDA fiber, HC-PCF and SC-PBG from experimental results.

time domain [48]. The measured pulse is split into two, one is variably delayed with respect to the other and then are spatially overlapped in one nonlinear-optical medium, such as SHG crystal shown in Figure 3.5. On the output side, three beams emerge. After one high-pass filter, only middle interference second-harmonic signal is detected by the photodetector, so that it appears without background. This setup is called as background free intensity autocorrelator. The advantage of background free intensity autocorrelator is that it can easily extract can directly give the average intensity autocorrelation [11].

In our experiment, 150 ps delay can be reached which enables both high resolution autocorrelation measurements and long range autocorrelation traces. One 1 mm thickness BBO crystal is used as the SHG crystal which can produce light as twice the frequency of input light. The output electric field is given by:

$$E_{sig}^{SHG}(t,\tau) \propto E(t)E(t-\tau), \tag{3.2.1}$$

where τ is the delay. This field has an intensity that's proportional to the product

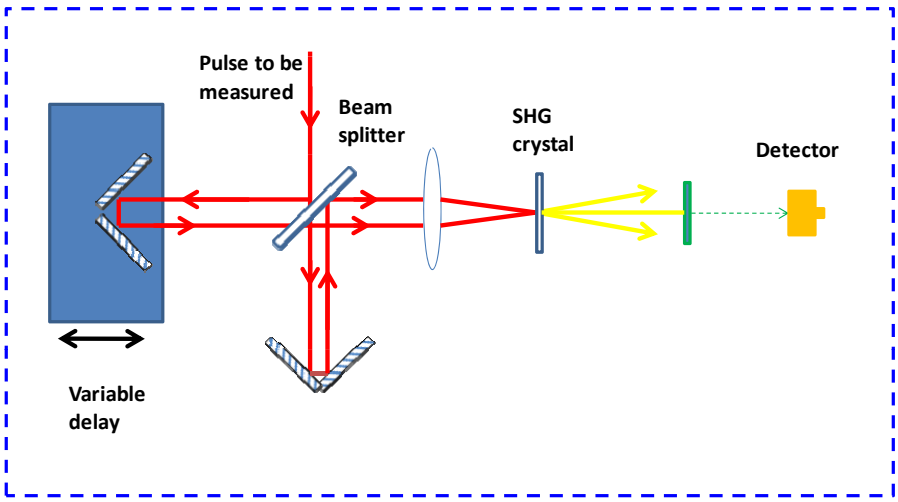

Figure 3.5: Experimental layout for an intensity autocorrelator using second-harmonic generation.

of the intensities of the two input pulses:

$$I_{sig}^{SHG}(t,\tau) \propto I(t)I(t-\tau). \tag{3.2.2}$$

Since photodectors are too slow to the time resolve $I_{sig}^{SHG}(t,\tau)$, this measurement produces the time integration of signal:

$$G^2(\tau) = \int_{-\infty}^{\infty} I(t)I(t-\tau)dt, \tag{3.2.3}$$

which is the definition of the intensity autocorrelation.

By changing variables in Eq. (3.2.3) from t to $t-\tau$, it can prove that the autocorrelation is always symmetric.As a result, the autocorrelation can not distinguish a pulse from its mirror image [48].

The ratio between the FWHM of the autocorrelation trace and the FWHM pulse duration is known as the deconvolution factor which depends on the temporal shape of the detected pulse. For a Gaussian pulse, the deconvolution factor is $\sqrt{2}$ and for $sech^2(t)$ intensity, the deconvolution factor is 1.543. For pulses of unknown temporal shape, the best way is to measure the spectrum and calculate the Fourier transform of the square of it as shown in Figure 3.6.

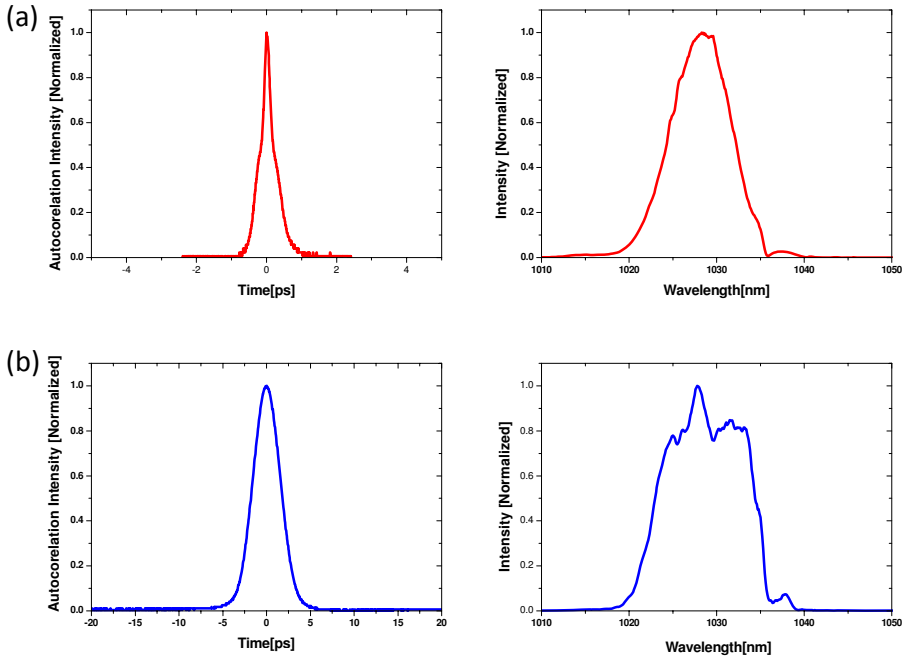

Figure 3.6: (a) and (b) Left: measured autocorrelation from the oscillator and first amplifier described in Chapter 5. Right: measured sepctrum respectally.

3.2.2 FROG

From last section, we already known that autocorrelation can easily extract the pulse intensity which is very important for ultrafast pulse's measurement. However, it can neither tell the exact pulse shape nor the phase since it's only operated in time domain. In order to get more information of ultrashort pulses, FROG which operates in both time and frequency domains is demonstrated.

There are several kinds of FROG technique and the simplest form is the autocorrelation-type measurement in which the autocorrelator signal beam is spectrally resolved [49]. The measurement scheme is shown in Figure3.7. The setup is similar to the autocorrelation measurement and the differences are that the delay line and detector. The detected input pulse is split into two beams and one is time shifted by an optical delay line. The delay line consists of a retro reflector positioned on a motorized translation stage with a 25 cm scanning range [50]. The SHG signal is detected by a grating spectrometer with a 0.22 nm resolution. Both the translation

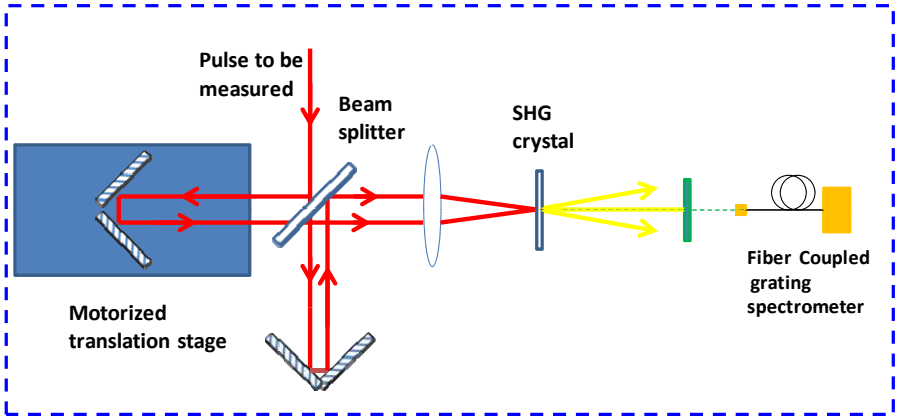

Figure 3.7: Experimental setup for SHG-FROG.

stage and spectrometer are controlled by computer. The main advantage of SHG FROG is sensitivity since it only involves a second-order nonlinearity.

From Eq.(3.2.1), the spectrum detected by the spectrometer can be expressed:

$$I_{FROG}^{SHG}(w,\tau) = |\int_{-\infty}^{\infty} E(t)E(t-\tau)exp(-iwt)dt|^2. \tag{3.2.4}$$

The measured time and frequency data are the spectrogram of the pulse which contains all information about the pulse and it gives a graphical representation on the pulse. And it is the same as intensity autocorrelation that the measured data is symmetric in time which means it can not tell a pulse transmitting forward or backward either. The output electric field can be retrieved from the spectrogram in an iterative phase retrieval process. The software FROG3 from Femtosoft Technoloties [51] is used for retrieval of the intensity and phase of pulses.

In order to retrieve both the intensity and phase of the pulse correctly, the measured data should have appropriate sampling rate [52]. For the FROG trace with $N \times N$ points where N is the grid size, the optimum sampling rate M is defined as the rate that samples the electric field at the same rate in both the time and frequency. A simple caculation is :

$$M \approx \sqrt{\frac{\Delta t_{FWHM}\Delta\lambda_{FWHM}Nc}{\lambda_0^2}}, \tag{3.2.5}$$

where Δt_{FWHM} and $\Delta\lambda_{FWHM}$ are the pulse temporal and spectral FWHM separately, and c is the optical velocity in vacuum.

For a transform-limited Gaussian pulse, Eq. (3.2.5) can be simplified to:

$$M \approx \sqrt{\frac{2NLn(s)}{\pi}}. \tag{3.2.6}$$

The time step and spectrum step can be calculated as:

$$\Delta t = \Delta t_{FWHM}/M, \tag{3.2.7}$$

and

$$\Delta\lambda = \Delta\lambda_{FWHM}/M. \tag{3.2.8}$$

For example, $M = 5.3$ for a transform-limited Gaussian pulse with a 100 fs FWHM to get a 64×64 trace. In real experiments, the grid size is usually chosen as 128 or 256. The larger grid size will make the retrieval algorithm slower. For heavily chirped pulse, $\Delta\lambda_{FWHM}$ is not broad enough and sometimes $\Delta\lambda$ is even smaller than the spectrometer's resolution 0.22 nm. In this case, data progress by matlab is needed to get the required spectrum step.

When aligning the SHG FROG setup, it has to be ensured that the actual pulse is measured. The marginal should look like the SHG spectrum that is expected from measurements of the spectrum of the input pulse. Besides of making sure the retrieved FROG in good agreement with the measured spectrogram, we also compared the retrieved autocorrelation to the autocorrelation measured by intensity autocorrelator mentioned in the last section.

Figure 3.8 shows an example of a SHG FROG trace of a linearly chirped pulse from the monolithic fiber laser described in chapter 5 [53, 54] but without the final pulse dispersion compensation. Figure 3.8 (a) and (b) show a good agreement between experimental and retrieved traces and the retrieved pulse yields a FROG error of 0.5% which indicated a very accurate measurement. The retrieved pulse intensity and phase is shown in Figure 3.8 (c). It is noted that the saved output of retrieved phase by software FROG3 is reversed sign (observed by Morten Bache) and has been changed back in this thesis. The retrieved autocorrelation is also compared with the one measured by intensity autocorrelation setup and has a good match which also indicates the accuracy of the SHG FROG measurements. On the other side, the retrieved pulse intensity by SHG FROG also proofed the accuracy of pulse duration predicted by the intensity autocorrelation measurements which

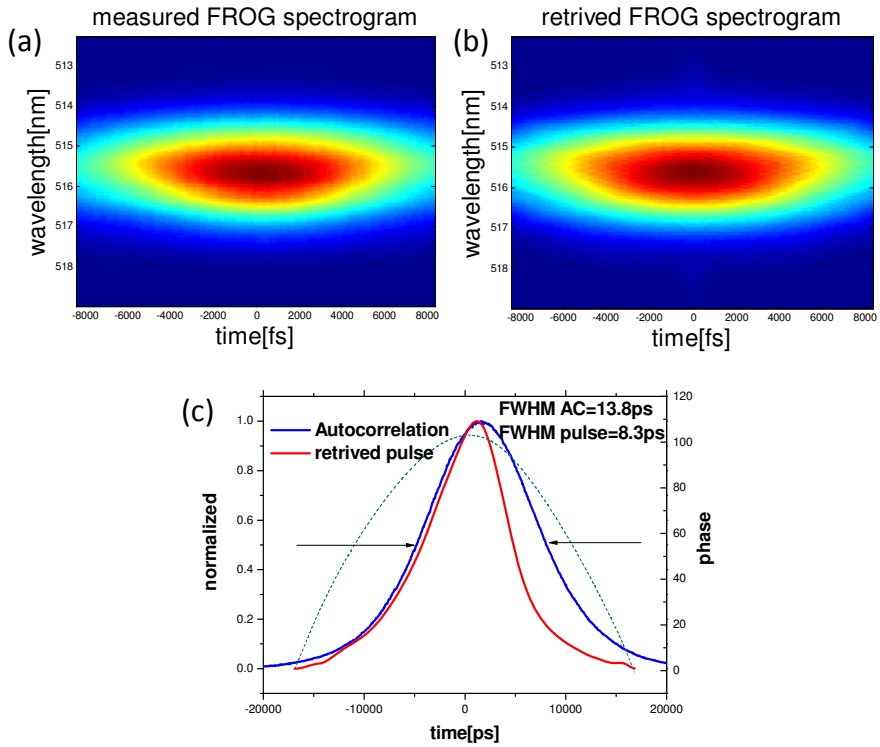

Figure 3.8: (a) Measured SHG FROG trace from one monolithic fiber laser described in chapter 5. (b) Computed SHG FROG trace of the retrived pulse. (c) Retrived intensity (red line), autocorrelation (blue line) and phase (dash) vs. time. FROG error 0.5%.

ensure correctness of the results described in chapter 4 and 5 even if only with the intensity autocorrelation measurements.

Chapter 4

Monolithic All-PM Femtosecond Yb-Fiber Laser Stabilized with a Narrow-Band FBG

This chapter describes one environmentally stable monolithic all-PM femtosecond Yb-fiber laser, stabilized against Q-switching by a narrow-bandwidth FBG and mode-locked by SESAM [55]. After amplifier, the laser output is compressed in a spliced-on hollow-core PM photonic crystal fiber [56], thus providing direct end-of-the-fiber delivery of femtosecond pulses of around 400 fs pulse duration and 4 nJ energy with high mode quality.

4.1 Introduction

Mode-locked femtosecond Yb-fiber lasers find nowadays numerous applications and compete successfully with their solid state counterparts, such as Ti:Sa oscillators. Different laser cavity designs and mode-locking principles have been demonstrated [57, 58, 59, 60], however only a few of the Yb-fiber lasers were realized in a truly all-fiber, i.e. monolithic format . To the best of our knowledge, an all-PM monolithic nJ-level Yb-fiber laser with direct end-of-the-fiber delivery of femtosecond pulses

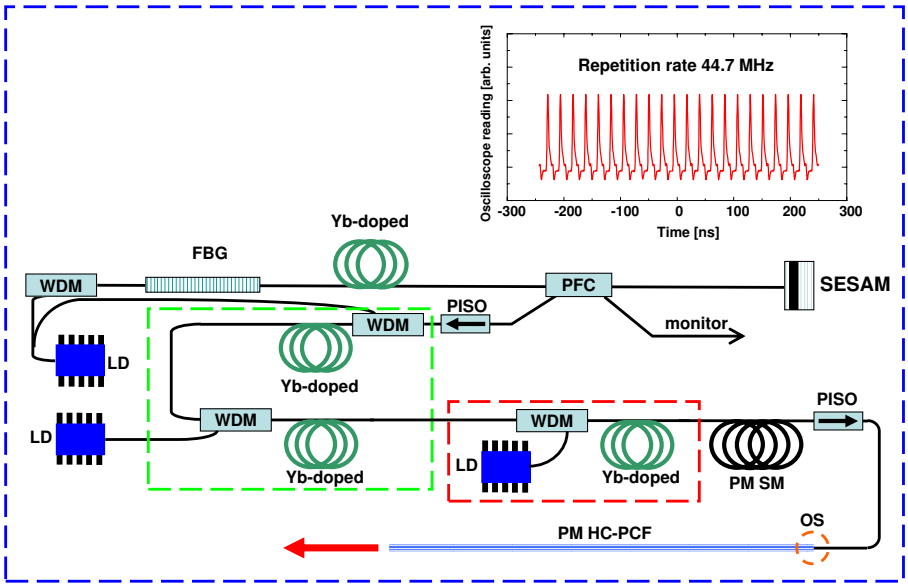

Figure 4.1: General layout of the laser. FBG - fiber Bragg grating, SESAM - semiconductor saturable absorber mirror, WDM - 980/1060 nm wavelength division multiplexer, PFC - 20/80 polarization filter coupler, LD - pump laser diode at 976 nm, PISO - polarization-maintaining isolator, PM SM - polarization-maintaining single-mode fiber. PM HC-PCF - polarization-maintaining hollow-core photonic crystal fiber, OS - optimized splice. Inset: oscilloscope reading of the mode-locked pulse train.

has not been demonstrated so far.

Mode-locking stability is yet another critical issue, which is not often commented upon in the literature. Nevertheless, mode-locking stability is a key parameter for most laser applications, especially for the applications where further amplification of the laser is required. In this case the integration of all-fiber components to make a monolithic guided-wave laser that resists environmental abuse [61] is needed.

4.2 Experimental Setup and Results

Mode-locked lasers operate in two mode-locking regimes - stable mode-locking with a minimized pulse-to-pulse fluctuations, and Q-switch mode-locking, where spon-

taneous increase in pulse intensity leads to depletion of inversion in active medium by a few laser pulses followed by subsequent inversion recovery. Therefore the Q-switch mode-locked laser output intensity will be chaotically time-modulated by the gain depletion-recovery dynamics. This results in enormous pulse-to-pulse intensity fluctuations at relatively constant time-averaged output intensity of the laser, i.e. some of the pulses will have giant peak intensities.

Q-switch mode-locked lasers are prone to fast degradation of cavity elements, and their amplification often leads to destruction of amplifier components. Also, Q-switching lasers are obviously not suitable for such applications as medicine and metrology, where high control over the laser performance is needed.

Below we will demonstrate a self-starting, fully monolithic linear cavity all-PM-fiber solution for a nJ-level fs laser which is stable against Q-switch mode-locking regime in a wide range of intracavity pulse energies. This is achieved by using a combination of narrow-bandwidth FBG and a SESAM with high modulation of reflectivity.

4.3 Operational Principles and Theoretical Modelling

Here we will describe the operational principle of our laser. In consists of a mode-locked oscillator, a series of pre-amplifiers, a power amplifier, and a spliced-on HC-PCF, in which the output laser pulse is compressed down to femtosecond duration with low loss and high degree of polarization stability. The oscillator has a linear cavity consisting of PM SM passive and Yb-doped fibers, confined between a SESAM and FBG, as shown in the Figure 4.1. Pumping of the oscillator by single mode 976 nm LD is achieved via 980/1060 nm polarization-maintaining wavelength division multiplexer (PM WDM). The laser signal is outcoupled via polarization-maintaining 20/80 filter coupler (PFC).

SESAM supports the intensity fluctuations in the laser cavity so, that the signals with higher peak intensities will experience lower cavity loss. This results in the situation, where the pulsed operation of the laser is preferable, and thus the self-starting mode-locking is achieved. On the other hand, since the spontaneous increase in the pulse peak intensity as a result of pulse-to-pulse intensity fluctuations within the mode-locked pulse train will still lead to lower cavity loss due to the nature of SESAM, these fluctuations may lead to chaotic Q-switch mode-locking regime of the laser.

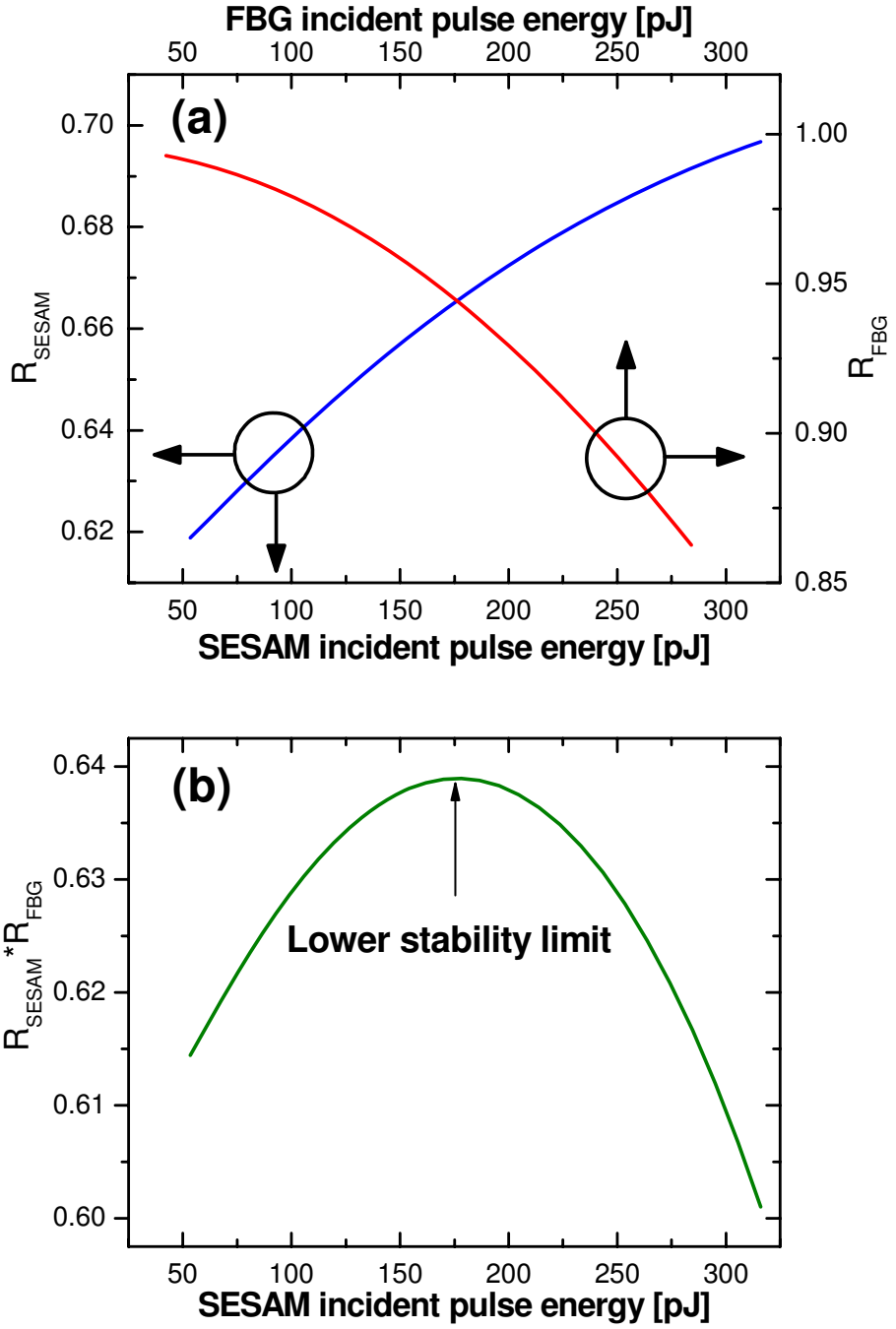

Figure 4.2: (a) Reflectivity of SESAM and FBG in dependence on the respective incident pulse energy. (b) Combined reflectivity of SESAM and FBG in dependence on the energy of the pulse incident on SESAM.

In order to stabilize and dispersion-manage the cavity, we employ a uniform narrow-bandwidth FBG. Stronger pulses in optical fibers undergo substantial SPM, which leads to an increase in the spectral bandwidth of the pulse. Thus, the excess energy of the pulse will be spectrally redistributed to shorter and longer wavelength sides of the pulse spectrum in respect to the central wavelength of the laser pulse. Therefore, if the laser cavity is accomplished by a narrow-band FBG serving as an end mirror, the excess pulse energy resulting from a strong fluctuation will not be reflected back into the cavity, and will leave the cavity past the FBG.

Bragg gratings, even uniform ones, also have positively and negatively chirping spectral regions. Thus, apart from enforcing the central wavelength of the laser, an FBG can be used as the means of dispersion management in the cavity, balancing the effect of pulse propagation through the long positively chirping single-mode fibers.

A numerical modeling of our laser based on the model is presented in [30].

The combined action of SESAM and narrow-band FBG on the total cavity loss is illustrated in Figure 4.2. In Figure 4.2 (a) separate contributions of the SESAM and FBG are shown. While SESAM provides growing reflectivity as a function of incident pulse energy, the FBG reflectivity decreases as a result of more self-phase modulated spectral bandwidth of the pulses being dumped away from the cavity. The SESAM and FBG reflectivities are shown on different incident energy scales because the 20% outcoupling of the laser pulse occurs in between the reflection events in each of these elements. In Figure 4.2 (b) the combined reflectivity of SESAM and FBG is shown as a function of the pulse energy incident on the SESAM. It has a clear maximum at around 175 pJ incident pulse energy. This maximum marks the lower stability limit of the laser in terms of incident pulse energy. When the incident pulse energy will reach twice this value, i.e. 350 pJ, the conditions for formation of double pulses in the cavity will be achieved. This energy will correspond to the upper stability limit of the laser. We do not present the calculated results in this pulse energy region because the model [30] breaks down.

In Figure 4.3 a detailed performance of the FBG as both a pulse energy stabilizer and an intra-cavity dispersion management element is illustrated. The pulse energy dependencies of reflectivity and transmission spectra of the FBG is shown in the Figure 4.3 (a,b) on a normalized 30 dB scale.

One can see that while the FBG-reflected spectrum (Figure 4.3 (a)) slowly broadens and then stabilizes as the incident pulse energy grows, the FBG-transmitted

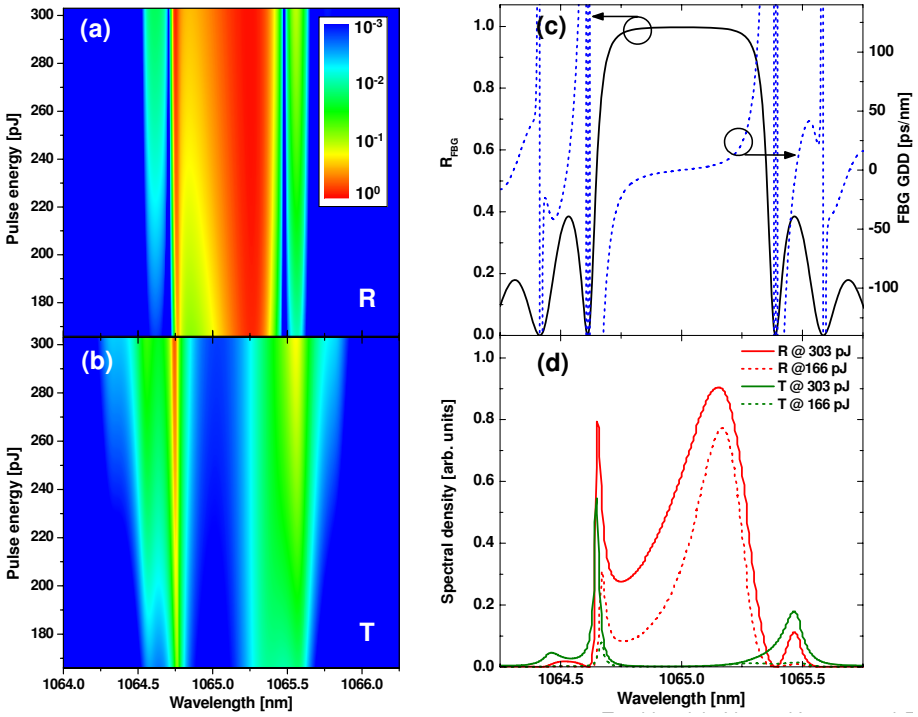

Figure 4.3: Calculated spectra of the (a) pulses, reflected back into the cavity and (b) pulses, dumped away from the cavity by the FBG in dependence on incident pulse energy. Spectral intensity is shown on a 30 dB scale, normalized to the maximum of the strongest reflectivity spectrum. (c) Power reflectivity and group delay dispersion of the FBG. (d) Calculated spectra of the pulses reflected back into the cavity (red) and dumped away from the cavity (green) by the FBG for the pulse energies of 166 pJ and 303 pJ.

spectrum (Figure 4.3 (b)) always demonstrates substantial spectral broadening. This indeed will lead to the optical limiting behavior of the FBG, as the even higher fraction of the incident pulse energy will be dumped away from the cavity as illustrated in the Figure 4.2.

In Figure 4.3 (c) we show the calculated reflectivity and GVD of the FBG. Even though this FBG is a uniform one, it is positively chirping (i.e. has negative GVD) on the shorter-wavelength part of its spectrum, and is negatively chirping (i.e. has positive GVD) on the longer-wavelength part of its spectrum. In the center of a reflection band the FBG is dispersionless. Thus, the longer-wavelength part of the FBG can be successfully employed for the dispersion compensation of otherwise positively chirping laser cavity.

The spectra of FBG-reflected and FBG-transmitted laser pulses in the cavity are shown in Figure 4.3,(d) for two incident pulse energies. One can see that the FBG-reflected (i.e. supported by the cavity) laser pulse is mostly formed on the longer-wavelength, negatively-chirping side of the FBG reflectivity spectrum. Thus we demonstrated that the stable pulse formation in our laser is totally governed by the FBG performance.

In Figure 4.4 the calculated pulse shapes for the pulses of various energies are presented. The pulse always consists of a strong peak followed by a weak damped oscillating trail. This trail is formed by the spectral weight in the normal-dispersion region of the FBG. In the inset of Figure 4.4 we present the pulse duration at FWHM of the main peak in dependency on the pulse energy. It is decreasing with increase in the pulse energy, as a result of more bandwidth present in the stronger pulse (see In Figure 4.3 (a)). The decrease is weak, however, due to the strong bandwidth-limiting effect of the FBG.Indeed, the sub-nm bandwidth of the oscillator-generated pulses does not allow for their resulting femtosecond. The pulses oscillator pulses are near-bandwidth-limited to picosecond duration, as shown in Figure 4.4. In our approach a higher bandwidth of the oscillator pulse was sacrificed for the excellent stability properties of the oscillator. Nevertheless, further amplification and consequent spectral expansion of a very stable oscillator pulse up to several THz of bandwidth is straight-forward, as will be demonstrated below.

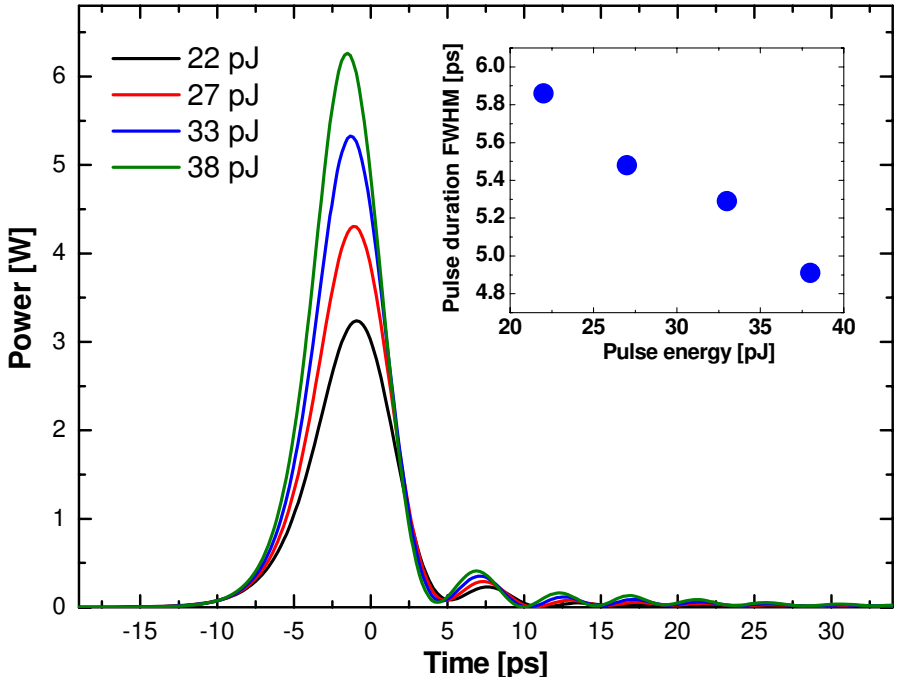

Figure 4.4: Calculated shapes of the out-coupled pulses of different pulse energies. Inset: pulse duration at FWHM in dependence on the pulse energy.

4.4 Experimental Results

The oscillator cavity consisted of 2.3 m of Nufern PM Panda fiber [62], of which 0.3 m was Yb-doped [31] (see Figure 4.1). This cavity length provides the oscillator repetition rate of 44.7 MHz. The cavity was confined between an FBG with the center of the reflection band at 1065 nm, and a SESAM with 24% saturable loss. We have also successfully tested several other cavity lengths, which resulted in the repetition rates ranging between 34 MHz and 80 MHz. The stable mode-locking without entering the Q-switching mode was maintained for more than 18 hours.

The central wavelength of 1065 nm was chosen to match the wavelength of minimum third-order dispersion in the Crystal Fibre A/S HC-1060-02 PM HC-PCF [63], which is used for monolithic compression of the output of our laser down to femtosecond pulse duration. PM HC-PCF are the fibers of natural choice for low-loss high-PM monolithic fiber laser pulse compression [56], since they demonstrate the unique combination of the properties needed for this task: high and and rela-

tively flat anomalous dispersion, low third-order dispersion, and low loss in a wide wavelength range, and low Kerr nonlinearity.

The oscillator showed stable self-starting and long-lasting mode-locking in the range of pump powers of 30-45 mW provided by the single-mode laser diode operating at 976 nm. The oscilloscope-measured mode-locked pulse train produced by the oscillator is shown in the inset of Figure 4.1. At 32 mW of pump power the output pulse energy of the oscillator was 20 pJ as measured after the PISO.

The oscillator output wa sequentially preamplified in a series of single-mode amplifiers up to the level of 600 pJ, before entering an end amplifier. Sequential preamplification was required in this case to bring the contrast between the laser light around 1065 nm and ASE in Yb at around 1040 nm to the level of > 30 dB before end amplification. The end amplification in yet another single-mode amplifier with the slope efficiency of 0.61 brought the output pulse energy to the level of 10.2 nJ. At this final stage the contrast between the laser output and ASE was reaching the values of > 20 dB.

The laser output was launched into a long piece of PM SM fiber, where the spectrum was broadened up to the bandwidth of 11 nm at FWHM due to the self-phase modulation. The broadband output was then isolated in yet another PISO with the insertion loss of 2.7 dB, before launching into a compression HC-PCF.

In Figure 4.5 (a) the normalized output spectra measured at the output of the oscillator, after the PISO accomplishing the spectral-broadening fiber, and at the end of the laser after 9.5 m of compression HC-PCF are shown, along with the GVD of the HC-PCF. It can be seen that the spectral broadening in the long piece of PM SM fiber by a factor of > 10 was achieved while still retaining the acceptable spectral shape with minimum number of fringes. The spectrum of the laser pulse stays practically unchanged after the propagation through nearly 10 m of HC-PCF, which demonstrates a very low Kerr nonlinearity of such a fiber.

In order to estimate the length of the HC-PCF needed to compress the pulse of such a duration and with the spectrum shown in 4.5 (a), we performed a numerical modelling of the pulse propagation, taking into account the GVD of the fiber, shown in the same figure. The calculations results are shown in the 4.6 (a), as a function of HC-PCF length. This calculation results in the shortest pulse duration after propagation through 10.8 m of the fiber.

We have performed and optimized splice between the PM SM pigtail of the end PISO and a piece of PM HC-PCF, using the procedure described in [56]. Such an approach allows for the PM-SM-to-HC-PCF splice loss of only 0.62 ± 0.24 dB,

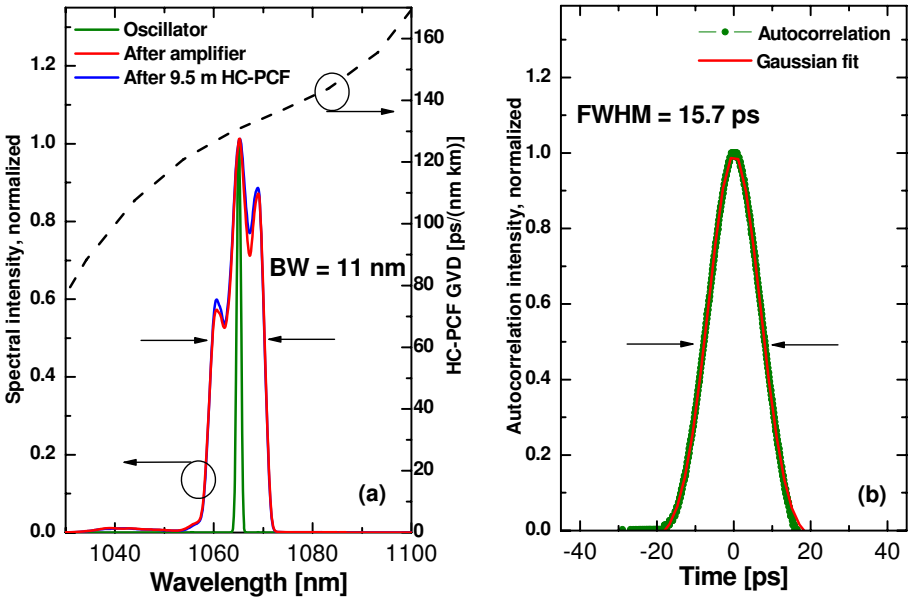

Figure 4.5: ((a) Normalized spectra measured at the output of the oscillator, end amplifier, and after 9.5 m of HC-PCF. HC-PCF group velocity dispersion (from [63]). (b) Intensity autocorrelation of the pulse measured after the end amplifier, and its Gaussian fit.

and polarization extinction ratio (PER) of 19 ± 0.68 dB. As was shown in [56], low splice loss is a key prerequisite in achieving high PM properties of the splice, and thus of the whole fiber assembly. The group birefringence of HC-1060-02 PCF was measured to be of $\Delta n = 1.65 \cdot 10^{-4}$ [56], which ensures its high PM properties.

The noncollinear intensity autocorrelation of the isolated output of the laser before the compression is shown in the Figure 4.5 (b). The shape of the autocorrelation signal is a near-perfect Gaussian with the FWHM of 15.7 ps. The deconvoluted pulse duration at FWHM is in this case 11.1 ps [64].

A noncollinear intensity autocorrelation of the compressed laser output at the end of the long piece of the HC-PCD was measured, and a series of cutbacks was performed in order to achieve the shortest pulse duration. We have found that the shortest output pulse corresponds to 9.5 m of the HC-PCF length, which is in a very good agreement with our theoretical estimate of 10.8. The autocorrelation has a near-Lorentzian shape with the FWHM of 615 fs, and the pulse energy was 4 nJ. This decrease of the pulse energy from 10.2 nJ measured right after the end amplifier

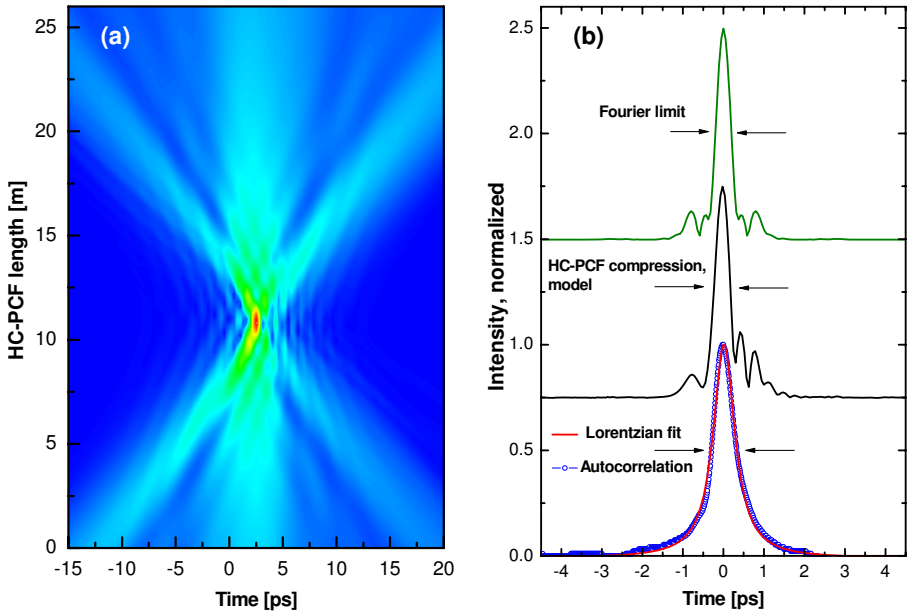

Figure 4.6: (a) Calculated pulse shapes in dependence on the HC-PCF length. Initial pulse shape is defined by the amplifier output spectrum and the deconvoluted pulse duration from the Figure 4.5. (b) Calculated pulse shapes in Fourier limit and at shortest pulse duration from the HC-PCF propagation model; Measured intensity autocorrelation after propagation through 9.5 m of HC-PCF, and its Lorentzian fit.

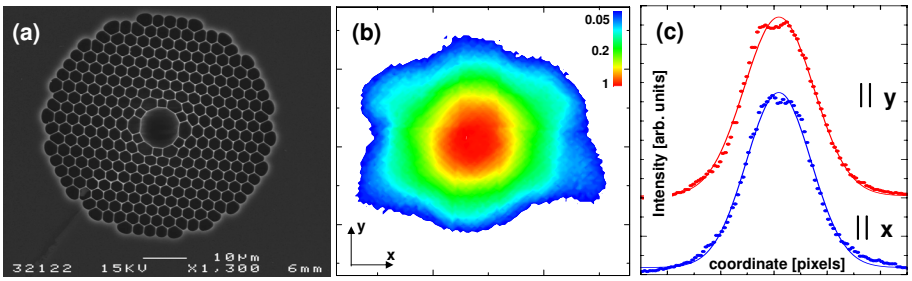

Figure 4.7: (a) SEM image of the HC-PCF. Courtesy of B.J.Mangan, Crystal Fibre A/S. (b) Measured far-field profile of the laser mode on the logarithmic intensity scale. (c) Cuts through the maximum intensity area of the laser mode profile in vertical and horizontal directions on the linear intensity scale, and their Gaussian fits.

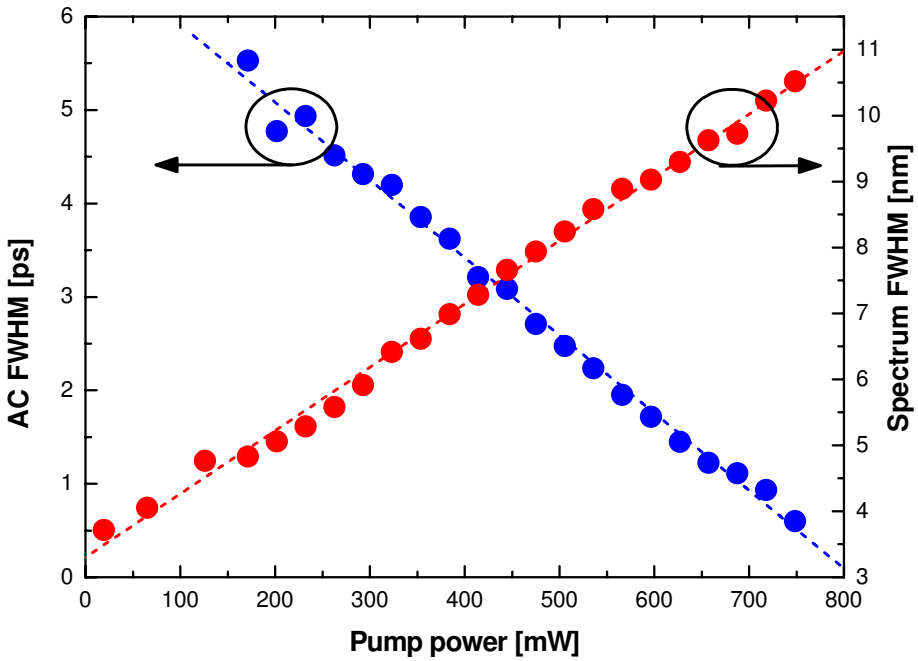

Figure 4.8: Dependencies of spectral width at FWHM, and intensity autocorrelation duration at FWHM of the laser pulse on the end amplifier pump power.

is caused mostly by the high insertion loss of the end PISO, whereas combined HC-PCF loss, consisting of the splice loss and attenuation in the fiber, only reaches 1.35 dB.

In Figure 4.6 (b) the noncollinear intensity autocorrelation of the shortest HC-PCF-compressed pulse is shown together with the calculated bandwidth-limited pulse shape (inverse Fourier transform of the power spectrum with flat phase), and the shortest pulse shape resulting from the numerical propagation calculation in Figure 4.6 (a).

The calculated bandwidth-limited pulse has FWHM duration of 370 fs, whereas the shortest pulse resulting form the HC-PCF propagation calculation has FWHM duration of 415 fs. The FWHM duration of near-Lorentzian autocorrelation of 615 fs would result in the deconvoluted FWHM pulse duration of only 307.5 fs, given the Lorentzian autocorrelation deconvolution factor of 0.5 [64]. This value is lower than that for the Fourier limited pulse (370 fs), although Lorentzian pulse shape has low-intensity wings that span for at least ± 2.5 ps in respect to the autocorrela-

tion maximum, thus resulting in an overall longer pulse. Nevertheless, comparison between the measured autocorrelation and calculated pulse shapes, and a good agreement in the theoretical and experimental length of the HC-PCF length needed to achieve the shortest pulse duration from the given spectrum and initial pulse duration, allows us to estimate the resulting pulse length to be around 400 fs.

Figure 4.7 shows the SEM image of the HC-PCF fiber and the resulting far-field laser mode shape. The HC-PCF based on the 7-cell design provides the near-single mode Gaussian output overlapped with a low-intensity hexagonal pattern in the far-field. The cuts through the maximum intensity area of the mode shape made in horizontal and vertical directions of the mode image show near-perfect Gaussian shapes, with vertical-to-horizontal FWHM aspect ratio of 1.07. Interestingly the low-intensity hexagonal pattern has an apparent vertical-to-horizontal aspect ratio of < 1, which is illustrated by the deviation from a Gaussian line shape in the low-intensity part of the horizontal direction cut. This weak mode ellipticity is a result of a slight asymmetry of the core typical for the air-guiding 7-cell core design fibers, which is also responsible for the high birefringence of the HC-PCF leading to its strong PM properties.

The monolithic all-fiber laser like the one described above has only one user-accessible degree of tuning freedom - change in the power provided by the pumping laser diodes. Figure 4.8 demonstrates dependencies of the resulting pulse autocorrelation duration, and its spectral bandwidth, both measured at FWHM, on the end amplifier pump power. The compression HC-PCF was kept at the same length of 9.5 m as in the measurements shown above. One can see that the generated bandwidth growth linearly with increase in the pump power, whereas the resulting autocorrelation duration linearly decreases. These linear dependencies demonstrate, that the proposed laser design has a potential in scalability leading to both higher output pulse energies and shorter pulse durations, as well as a high degree of tunability in its performance by simply adjusting the pump power in the end amplifier. The tunability limit will be reached when the bandwidth will reach the values, at which the higher-order dispersion will act stronger on the spectral wings of the pulse, thus stretching it due to higher positive nonlinear chirp. The spectral shape may also become a limiting factor at this stage, since more spectral fringes will result in the pronounced wings in the pulse, and an overall more complicated resulting pulse shape.

4.5 Summary

In conclusion, a fully monolithic, i.e. without any free-space coupling, all-PM femtosecond laser with a very high pulse stability against Q-switching laser has been demonstrated. The laser is mode-locked using a SESAM and is stabilized and dispersion-managed using a narrow-bandwidth FBG. The subsequent amplification of the laser in a series of single-mode amplifiers and monolithic compression in spliced-on PM HC-PCF results in the pulses of around 400 fs duration and 4 nJ pulse energy, directly delivered from the fiber end.

The laser has a potential in scalability both in terms of higher pulse energies and shorter pulse durations, as well as in the repetition rate (by adjusting the cavity length). It also offers a high degree of tunability in the resulting pulse energy, duration and chirp by simply adjusting the pump power in the final amplifier stage. A reasonably good agreement between theoretical predictions and experimental results is observed for such crucial parameters as the laser mode-locking stability lower limit and the HC-PCF pulse compression performance.

Exceptional stability of this laser suggests that it has a very high potential as a stable seed source for a novel Yb-doped amplifier systems, such as based on Yb:KGW [65] and Yb:YAG [66] medium.

Chapter 5

Highly-Stable Monolithic Femtosecond Yb-Fiber Laser System Based on Photonic Crystal Fibers

This chapter describes one self-starting, passively stabilized all fiber SESAM mode-locked femtosecond laser with very high operational and environmental stability [53, 54]. The system is based on the use of SC-PBG and HC-PCF for intracavity and extracavity dispersion compensation respectively. With the 232 fs, 45 pJ pulses from the oscillator, the final direct fiber-end delivers around 297 fs, 7.3 nJ output. And using the high power fiber amplifier, more than 1W pulses which can be used for supercontinuum generation are delivered directly from fiber end. Our laser shows exceptional stability. During more than one week's running, no Q-switched mode-locking events were detected. An average fluctuation of only $7.85 \cdot 10^{-4}$ over the mean output power was determined as a result of more than 6-hours measurements. The laser is stable under mechanical disturbances and also stable in the temperature range of at least $10 - 40^0 C$.

5.1 Introduction

Recent progress in the development of fs fiber lasers has resulted in pulse energies and durations comparable to the solid-state lasers. For the applications in medicine, micromachinning and metrology, The environmental and operational stability of the laser is crucial. Many of the demonstrated lasers are laboratory-based, table-top system, at least partly relying on the technology typical for the solid-state lasers, such as free-space coupling and mechanical adjustment. In order to achieve high environmental and operational stability of the laser, free-space coupling should be avoided and self-stabilization mechanisms should be present to ensure the stable mode-locking operation. Also, direct fiber-end delivery of pulses without free space devices such as gratings or prisms is also an important advantage.

In chapter 4, mode-locking and stabilization using FBG [30, 55] is described. In that case, although the laser is compact and stable, the output pulses' spectrum is sacrificed due to the narrow bandgap of FBG. A monolithic oscillator with larger bandwidth and transform-limited pulses would be highly desirable because it would allow the use of either parabolic [67] or chirped-pulse [68] amplification to generate high-power ps pulses suitable for dispersive recompression.

In this chapter, a highly stable fs master oscillator and power amplifier operating around the wavelength of 1035 nm based on the use of different types of photonic crystal fibers will be demonstrated. One is used for intra-cavity for both oscillator dispersion compensation and stabilization. The stabilization is realized by distributed nonlinear filtering and optical limiting which results in the environmental and operational stability of the system. HC-PCF is used for the final low-nonlinearity compression of amplified laser pulses. Our system employs CPA principle where the output of the femtosecond oscillator is strongly stretched before amplification in order to preserve smoothness of the spectrum.

PCF was used in a non-monolithic and no-PM cavity for dispersion compression in [69] and one similar arrangement to ours based on non-PM fibers and partly using free-space coupling was presented in [12]. However the stability of this laser was comparable to "that of other non-PM fiber lasers - that is the laser was not environmentally stable and the output could be affected by moving the fibers"

This laser delivers the pulses with fixed polarization state of 297 fs duration in the main peak and 7.2 nJ total energy (of which 56% is in the main peak). This performance is comparable to some other published lasers. However, the operational and environmental stability of our laser is extremely high which is crucial for most

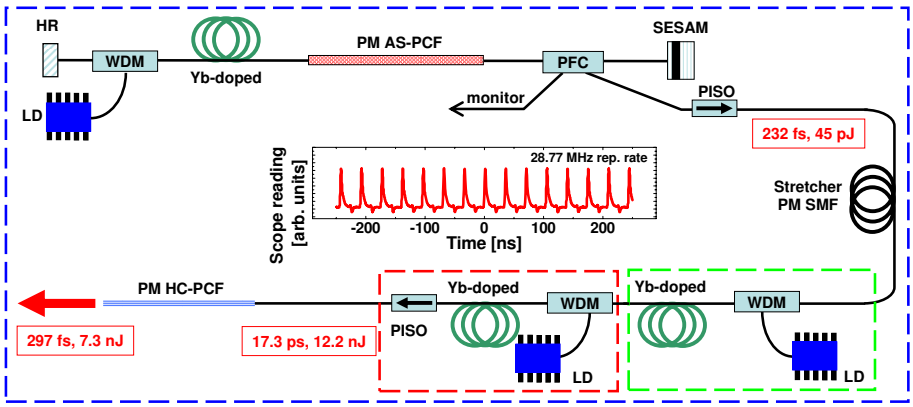

Figure 5.1: General layout of the MOPA. HR - high-reflectivity broadband mirror, SESAM - semiconductor saturable absorber mirror, PM AS-PCF - PM all-solid photonic crystal fiber, WDM - 980/1030 nm wavelength division multiplexer, PFC - 20/80 polarization filter coupler, LD - pump laser diode at 974 nm, PISO - polarization-maintaining isolator, PM SM - polarization-maintaining single-mode fiber. PM HC-PCF - PM hollow-core photonic crystal fiber. Inset: oscilloscope reading of the oscillator pulse train in fundamental single-pulse modelocking regime.

fiber laser applications. To the best of our knowledge, this is the first demonstration of a monolithic, non-table-top mode-locking femtosecond laser system which maintains stable operation in the temperature range of at least $10-40^0C$. This shows a potential of PCF-based technology in producing a highly stable mode-locking femtosecond fiber lasers, as an alternative to other approaches such as e.g. the use of FBG.

5.2 Laser Design

Our fully monolithic laser consists of four main stages: a mode-locking oscillator, a stretcher fiber, am amplifier stage featuring a pre-amplifier and a booster amplifier, and a spliced-on HC-PCF pulse compressor. All stage, including the compressor, were based on PM fibers and were spliced together. The schematic of the laser is shown in Figure 5.1.

The linear-cavity oscillator was confined between a fiber-pigtailed SESAM and a fiber-pigtailed broadband high-reflectivity mirror. The SESAM had a modulation depth 24%, non-saturable loss of 16%, saturation fluence of $130uJ/cm^2$, and

relaxation time of 500 fs [39].A 32-cm long Yb-doped fiber [31] was used as gain medium.

The cavity dispersion management was performed using 1.21 m of specialty PM AS-PCF from Crystal Fibre A/S, which features anomalous dispersion at Yb wavelength. This fiber consists of fused SiO_2 core and matrix, and B:SiO_2 and Ge:SiO_2 rods, and is guiding using a hybrid mechanism: by TIR between SiO_2 core and B:SiO_2 rods in one plane, and by photonic bandgap mechanism provided by Ge:SiO_2 rods in the orthogonal plane [70, 71]. A scanning electron microscope (SEM) image of this fiber is shown in Figure 5.2 (a), and its transmission and dispersion spectra are shown in Figure 5.2 (b). The dispersion spectrum was estimated by spectral white light interferometry [46, 44].

This fiber was instrumental in passive stabilization of our laser by introducing the nonlinear optical limiting mechanism for the stronger pulses that result from spontaneous and induced intensity fluctuations. This self-stabilization mechanism is based on the wavelength-dependent cavity loss for the laser, introduced by the AS-PCF. As the intracavity power grows, the stronger laser pulses experience stronger SPM in the fibers, and their spectral bandwidth expands. In order to maintain the shorter pulse duration in a weakly-stretched pulse regime [72, 73] such stronger and spectrally broader pulses are formed on the longer-wavelength side of the AS-PCF transmission spectrum, featuring higher anomalous dispersion. On the other hand, the transmission loss of the AS-PCF is also higher in this spectral range, which leads to efficient optical limiting for such pulses, and to the delayed onset of Q-switched modelocked operation. The detailed investigation of such a self-stabilization mechanism of a modelocked femtosecond fiber laser with a photonic crystal fiber is presented in [53].

The rest of the cavity consisted of a standard PM SMF [62], and the total cavity length was 3.55 m, which resulted in the fundamental repetition rate of 28.77 MHz (see inset of Figure 5.1). The cavity was pumped by a 974 nm single-mode laser diode through a 980/1030 WDM, and for the outcoupling a 20/80 2x2 PFC was used. The oscillator had two outputs: one was isolated, stretched, and used for seeding the amplifier, and another one was angle-cleaved and used as a monitor port for stability observations.

The laser operated in a weakly-stretched pulse regime [72, 73] with small anomalous cavity dispersion. The net cavity dispersion on one roundtrip was estimated to be zero at 1024 nm, and at the laser central operating wavelength of 1033 nm it was 0.089 ps/nm [53]. The laser was self-starting, and provided stably modelocked pulses with the energies in the range 39-49 pJ, in the pump power range of 65-75

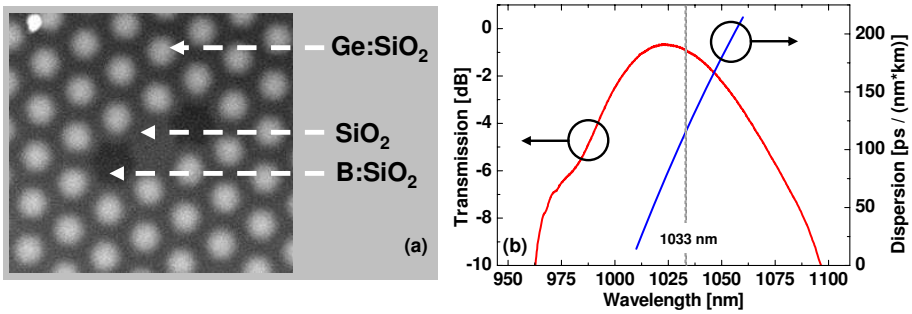

Figure 5.2: (a) SEM image of the PM AS-PCF. Courtesy of Crystal Fibre A/S. (b) Transmission and dispersion of PM AS-PCF. Central wavelength of the laser at 1033 nm is indicated by a grey line.

mW. At higher pump powers the laser enters a Q-switched ML phase, followed by a stable harmonic ML phase. The oscillator-generated pulses measured after 1-m long PM SMF pigtail following the outcoupler, had near-perfect Gaussian shapes with no side pulse visible in the autocorrelation, and at 45 pJ energy the pulse duration was estimated to be 232 fs at full width at half maximum (FWHM) from the autocorrelation with FWHM of 328 fs [53].

It is noted that at the outcoupling point the pulses were still negatively chirped, and were recompressed down to 232 fs during the propagation in the 1-m long PM SMF pigtail. We will discuss this recompression, as well as spectral and temporal evolution of the intra-cavity pulses in the oscillator cavity in the Theoretical section below.

The isolated output of the master oscillator was launched into a 35-m long standard PM SMF, where the laser pulse was stretched to approximately 12 ps duration, in order to decrease its peak intensity before amplification. The stretched pulse was amplified in a chain of two single-mode amplifiers to the energy of 12.7 nJ, corresponding to a cw equivalent power of 365 mW. After the isolation, the pulse energy was 12.2 nJ (351 mW of cw power). The pulse shape had the autocorrelation of 24.5 ps at FWHM, corresponding to 17.3 ps in pulse duration at FWHM, assuming Gaussian shape. The spectral bandwidth of the oscillator input pulse was 7 nm at FWHM, and after CPA and isolation it was 9 nm.

After isolation, the stretched and amplified laser signal was launched into a compressor - a hollow-core photonic crystal fiber (HC-PCF) HC-1060-2 from Crystal Fibre A/S [63], featuring anomalous dispersion at the laser wavelength. Such a fiber

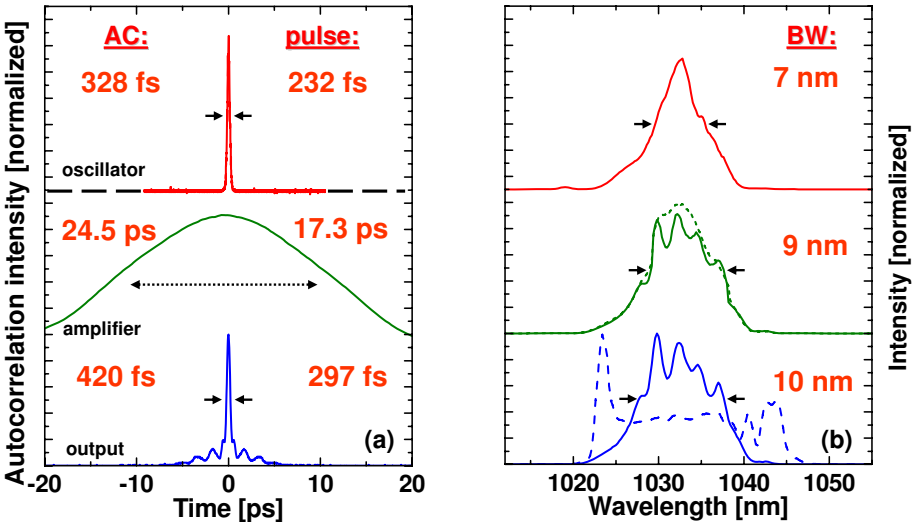

Figure 5.3: (a) Autocorrelations of the pulse measured after 1-m long PM SMF pigtail following the output port of the oscillator (45 pJ / 1.35 mW), at the isolated output of the amplifier before compression in HC-PCF (12.2 nJ / 351 mW), and at the output of the MOPA after compression in HC-PCF (7.3 nJ / 210 mW). Corresponding autocorrelation and pulse durations at FWHM are indicated. (b) Corresponding optical spectra. Spectral bandwidth at FWHM is indicated. Dotted line - amplifier spectrum measured before the isolator. Dashed line - output spectrum in the case when no CPA is used, i.e. the oscillator pulses are not stretched before amplification. See text for details.

has a group birefringence of $\Delta n = 1.65 \cdot 10^{-4}$, which ensures its high PM properties [56]. This HC-PCF was fusion-spliced onto the PM SMF output of the amplifier isolator with the splice loss of 0.6 dB using the technique described in [56].

After propagation through 21 m of HC-PCF, we achieved the shortest pulse duration with an autocorrelation of 420 fs at FWHM, and an estimated pulse duration of 297 fs. The spectral bandwidth of the compressed output pulse was found to be 10 nm at FWHM. The resulting cw output power was 210 mW, corresponding to a pulse energy of 7.3 nJ. The total compressor loss, including PM-SMF-to-HC-PCF splice loss was 2.2 dB, of which 1.6 dB was attenuation in HC-PCF.

Now the evolution of the laser pulse throughout the system in the temporal and spectral domains are showed respectively. In the time domain, shown in Figure 5.3 (a), an oscillator-generated near-perfect Gaussian pulse with FWHM duration of

232 fs acquires the duration of 17.3 ps after CPA, and is finally recompressed to the duration of 297 fs. The conversion factors from work [64] were used to estimate the pulse durations from the measured autocorrelations. The final pulse, however, is accompanied by little side pulses, as a result of residual chirp by non-compensated third-order dispersion in the HC-PCF, as well as by the spectral oscillations present in the isolated amplifier output. The pulse quality can be further significantly improved by achieving the parabolic amplification. In the work [67] it is shown theoretically and experimentally that near-parabolic pulses can be obtained by amplifying 200-fs input pulses in normal-dispersion fibers. Our recent work [74] shows that parabolic pulses may be compressed with high quality (> 90 % of the pulse energy in the main peak) at pulse energies of tens of nJ, when using a suitable (but realistic) hollow-core compressor fiber. This suggests that our approach can be further improved substantially before being limited by dispersion-slope effects.

In the spectral domain, shown in Figure 5.3 (b), the oscillator delivers a smooth spectrum with the bandwidth of 7 nm at FWHM, which then undergoes spectral broadening to 9 nm after CPA due to SPM in the amplifier fibers. The amplifier spectrum before isolation, shown by the dotted line, is smooth. However, after the isolator, the spectrum develops spikes, possibly due to spectral filtering in the isolator itself. The spectrum of the pulse compressed in 21 m of HC-PCF is very similar to that of the isolated amplifier output. However, its spectral bandwidth is now slightly larger and reaches 10 nm at FWHM. This low Kerr nonlinearity of the HC-PCF is in accordance with our earlier observations [55]. However, we note here that at the pulse energies reaching several nJ, and the pulse durations of only few hundred fs, as in this work, the Kerr nonlinearity of HC-PCF already becomes observable. The importance of using CPA for maintaining a relative spectral smoothness is shown by the example of an output spectrum in the case, where the seed pulse was launched into the amplifier without stretching (dashed line in Figure 5.3 (b)). This spectrum is very strongly distorted by the SPM.

5.3 Master Oscillator Theoretical Modelling

A detailed model of the master oscillator was set up along the lines described in [30]. The SESAM was described by a rate equation model using the parameters given above, the amplifier was approximated by a point amplifier surrounded by passive fibers with the proper dispersion values, and propagation in passive fibers was described by a generalized nonlinear Schrödinger equation. The inclusion of third-order dispersion is particularly important due to the careful dispersion balancing in

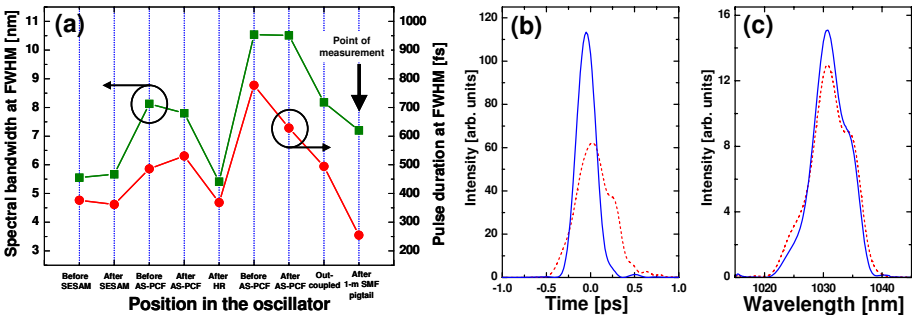

Figure 5.4: a) Calculated evolution of spectral bandwidth and pulse duration in the oscillator on one roundtrip, and after 1-m long PM SMF pigtail following the outcoupler (point of experimental measurements). (b) Calculated pulse shapes at the outcoupler (dashed line), and at the point of measurements (solid line). (c) Corresponding spectra.

the cavity, and the strong third-order dispersion of the AS-PCF. The dispersion parameters for the standard PM fibers were taken to be β_2=0.023 ps^2/m, β_3=3.9 $\cdot 10^{-5}$ ps^3/m [12], and the effective area was assumed to be 28 μm^2, corresponding to an MFD of 6 μm. For the amplifier fiber, the dispersion values were taken as β_2=0.039 ps^2/m and β_3=10^{-5} ps^3/m [31]. The dispersion parameters of the AS-PCF were measured to be β_2=-0.0577 ps^2/m, β_3=0.00133 ps^3/m, and its effective area was estimated to be 88 μm^2 from numerical modelling. The high β_2 and β_3 values of the AS-PCF reflect a complex and rapidly changing mode profile, which also imposes a splice loss to the standard PM fibers, with a significant frequency dependence. The measured insertion loss curve was included in the modelling and found to be crucial for explaining the excellent stability properties of the laser [53].

The model results reproduce most features of the experimental spectra, although the pulse energy where stable ML operation occurs is somewhat underestimated (around 30 pJ in the model). We attribute this discrepancy to differences in fiber effective area parameters, and possibly also SESAM parameters, between model and experiment. The modelling reveals a significant intracavity pulse breathing, with both temporal and spectral FWHM varying by about a factor of two, as shown in Figure 5.4 (a). Since the pulse seeks to optimize SESAM transmission, it is approximately transform limited at the SESAM, and by consequence also at the HR mirror at the opposite end of the cavity. This implies that the pulse has negative chirp at the outcoupling point, and will therefore recompress in a standard fiber with normal dispersion, such as the isolator pigtails used in the experiment.

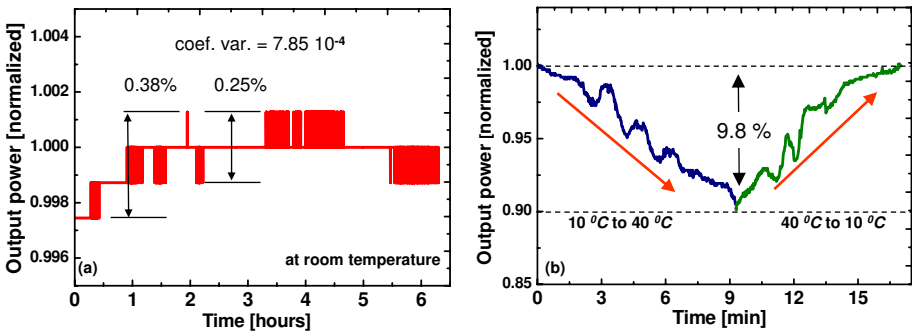

Figure 5.5: Output power of the oscillator in stable fundamental modelocking regime as (a) a function of lab time, measured at room temperature; (b) during reversible temperature sweeps in the range 10-40 ^0C. Here temperature was not changing evenly with time.

Interestingly, the calculated pulse duration after 1 m of pigtail is significantly shorter than the pulse width at any point in the cavity. This can be explained by the spectral recompression effect, occuring when a negatively chirped pulse propagates in a medium with a positive Kerr coefficient. From Figure 5.4 (a) it can be seen that the bandwidth of the cavity pulse decreases from 8.2 nm to 5.5 nm upon propagation from the point of output coupling to the SESAM. The outcoupled pulse, on the other hand, is four times weaker and therefore only recompresses to about 7.2 nm. It is noted that the calculated pulse after 1-m long pigtail is almost transform limited, and that both the calculated pulse duration (255 fs) and bandwidth (7.2 nm) are in very good agreement with the measured values (232 fs and 7 nm, respectively). In Figure 5.4(b,c) the pulse shapes and spectra right at the outcoupler and after 1 m pigtail propagation are shown. Note that the pulse shape in both the temporal and spectral domains has significant deviations from an ideal gaussian or $sech^2$ shape, suggesting that simplified models of stretched-pulse cavities based on such assumptions might not be applicable in this case.

5.4 Stability Measurements

A stability test of the oscillator by monitoring the output power during at least 6 hours of operation in the stably modelocked regime at room temperature also have been performed, see Figure 5.5 (a). We have observed a slight rise of the output power during the first hour of operation, which can be attributed to a thermal read-

justment of the pump diode. This initial output power rise amounts to a maximum output power fluctuation of only 0.38 %. In the following 5 hours of observations we noticed even smaller maximum output power fluctuations amounting to only 0.25 %. The "quantization" of the output measurement is caused by the discrete data acquisition scheme, available to us in this experiment. Based on these measurements we calculated the coefficient of variation over mean output power in the whole observation period. It was found to be only $7.85 \cdot 10^{-4}$, which is the long-term stability of our laser. This is a good result for a passively-stabilized monolithic, non-table-top femtosecond fiber laser system.

The overall modelocking stability of our laser was tested during 4-days long continuous operation, revealing no Q-switched modelocking events during this period. The laser remains stable against mechanical disturbances such as moving and reshuffling the fibers and kicking the tray on which the system rests. The laser operation can be disrupted by bending the fibers to around 1 cm of bending diameter, which results in higher cavity loss and puts the laser below threshold. Once such a strongly bent fiber is released, the laser fully resumes its stable operation.

The variable-temperature measurements are also been performed by placing the laser in a temperature chamber and performing temperature sweeps in the maximally-possible range between 10 ^{0}C and 40 ^{0}C. The results of the temperature stability measurements are shown in Figure 5.5 (b). The laser was always operating in the stable modelocked regime in the whole temperature sweep range, which suggests that the actual thermal stability range is even larger. At an increase of the temperature we observed an overall decrease in the output power, with a maximum power drop of 9.8 % at 40 ^{0}C. When the laser was cooled down back from 40 ^{0}C to 10 ^{0}C, the output power increased and reached the initial values, thus showing no hysteresis behavior. The output power decrease and increase during temperature sweeps was accompanied by the clearly visible oscillations, that we attribute to a known effect of the temperature-dependent polarization evolution in PM fiber splices. We note here, that the temperature was not changing evenly with time during these measurements, and only the starting and ending temperatures were known precisely. Thus, in Figure 5.5 (b) we are only able to plot the output power as a function of laboratory time.

The temperature dependence of Yb-ions emission and absorption cross-section [75], as well as the complex temperature-dependent effects in saturable absorber, affecting its recovery time and modulation depth [76, 77] all lead to the decrease of the laser output power at elevated temperatures. However, the stability of modelocking, i.e. the absence of Q-switching events during long-term and temperature

tests, is attributed to the presence of self-stabilization mechanism of the laser, relying on nonlinear optical limiting in the intra-cavity AS-PCF.

5.5 Supercontinuum Generation

Supercontinuum generation in nonlinear PCFs has for several years been studied as a source of spatially coherent broadband light [78]. Since the dispersion and nonlinearity of PCFs can be controlled, the ability to move the zero dispersion wavelength closer to the visible wavelength range has enabled generation of broad supercontinuum extending all the way down into the blue. If linearly polarized supercontinuum light passing through MIIPS which can adaptively and automatically compensate the combined phase distortion and compress the pulse[79]. this is very important for biophotonics imaging's application. The generation of wide supercontinuum in PCFs has been demonstrated with femtosecond laser. However, most of them are free space coupled which makes the supercontinuum spectrum unstable; for the fiber coulpled lasers, the output normally are not linearly polarized which can not be compressed by MIIPS. Since our monolithic fiber laser has stable and linearly polarized pluse output, it is suitable as the source for compressed supercontinuum generation.

Figure 5.6 shows one example of supercontinuum generation with 10 m NL-3.7-975 fibers [80]. The generated supercontinuum is not broad enough because of the low coupling coefficients between HC-PCF to NL-3.7-975 fiber due to the mismatch of their mode field area. This can be further improved by add one short piece of intermedium fiber whose mode field diameter is among the HC-PCF and the high nonlinearity fibers.

5.6 Summary

In conclusion, one monolithic femtosecond Yb-fiber MOPA using an all-solid PM PCF for dispersion management and stabilization of the master oscillator, and a PM HC-PCF for final pulse recompression has been demonstrated. The self-starting, HC-PCF-compressed MOPA delivers 7.3-nJ pulses with the main peak of around 297 fs FWHM duration directly from the output fiber end. A signature of non-compensated third-order dispersion is present in the pulse. Our future attempts will be aimed at achieving a parabolic pulse compression in this laser system, that can result in an improved resulting pulse quality.

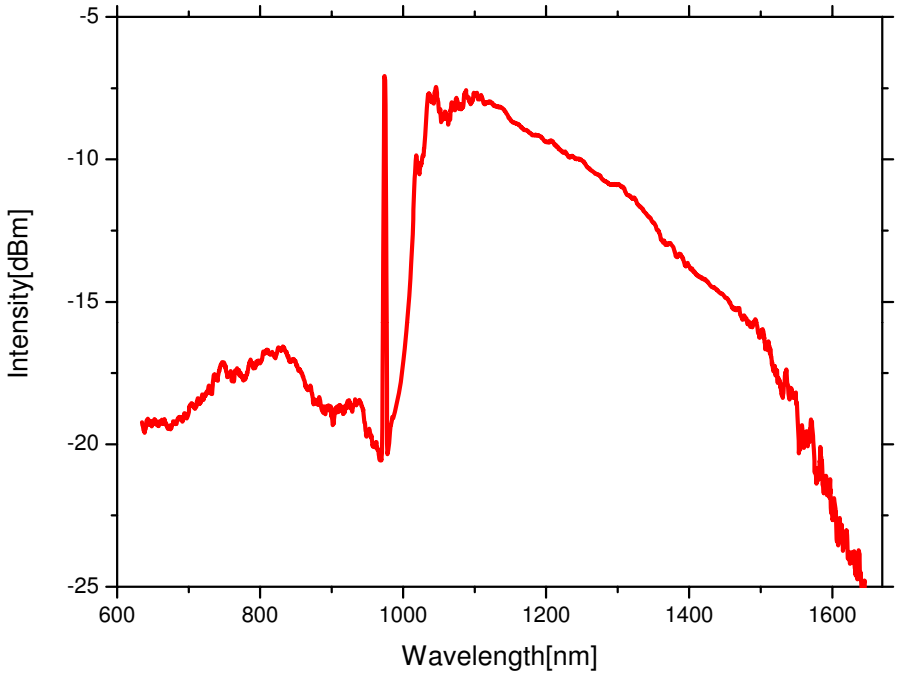

Figure 5.6: Supercontinuum after 10 m NL-3.7-975 fibers.

We have demonstrated a very high operational and environmental stability of the laser, resulting in less than 0.38 % output power fluctuations during more than 6 hours of operation, and maintained stable modelocking during temperature sweeps in the range 10 ^{0}C and 40 ^{0}C. The long-term stability of our laser, the coefficient of variation of output power, is only $7.85 \cdot 10^{-4}$ over more than 6 hours of measurements. The 4-days long observation of a stably modelocked laser revealed no Q-switched modelocking events during this period. We demonstrated that PCF technology can be a viable alternative to other methods such as e.g. FBGs in providing a monolithic and highly stable femtosecond fiber laser.

Such a laser has a potential in industrial and medical applications, where both high stability and direct fiber-end delivery of femtosecond pulses are required. High environmental stability could pave the way for use of this kind of a laser in a multimodality biophotonics platform, such as suggested in [81].

Finally, one example of supertinuum generation by our laser directly coupled to a high nonlinearity fiber was also demonstrated. The generated supercontinuum

spectrum can be further improved through increasing the coupling efficiency among HC-PCF and highly-nonlinear PCFs which can be realized by splicing an inter-medium fiber between.

Chapter 6

Quantum Well Saturable Absorber Mirror with Electrical Control of Modulation depth

6.1 Introduction

One way for passive mode-locking and control of ultrafast lasers is using SESAMs [32] e.g. the fiber lasers described in Chapter 4 and 5. The modulation depth - the value of saturable loss of the SESAM which was already described in Chapter 2, is an important parameter governing the self-starting and stability of laser mode-locking. In this chapter, an E-SESAM for the wavelength around 1065 nm, based on the low-temperature grown InGaAs/GaAs QWs embedded into a *p-i-n* structure is demonstrated. By applying the reverse bias voltage in the range $0-2$ V to the *p-i-n* structure, as measured by nonlinear reflectivity of 450 fs long laser pulses with 1065 nm central wavelength, in the pump fluence range $1.6-26.7 UJ/cm^2$, the modulation of the E-SESAM can be changed in the range $2.5-0.5\%$. This electrical control of the modulation depth is achieved by controlling the small-signal loss of the SESAM via quantum-confined Stark effect in the QWs.

The SESAM action is based on the saturation of the optical loss in the absorber

section at higher optical intensity, thus resulting in a higher SESAM reflectivity for stronger optical signals as described in chapter 2. The efficient mode-locking of an ultrafast laser is additionally dependent on the efficient ultrafast recovery of the saturable loss in the SESAM. This is ensured by the quick depletion of the photoexcited electronic states in the saturable absorber, which can be achieved by e.g. capture of the photoexcited carriers onto lattic defects [82, 83], and/or carrier sweep-out in an applied electric field [84]. The dynamical screening effect [85, 86] could also have an impact on the ultrafast dynamics in the biased QWs or QDs.

Laser mode-locking and control with E-SESAMs based on QWs [87, 88] and QDs [89, 90] was recently demonstrated by applying an electric field on the saturable absorber section. As in Ref. [88] the mode-locked laser stability could be manipulated and pulse shortening from 50 ps down to 20 ps could be realized, accompanied by the spectral expansion of the laser signal from 0.3 to 0.8 nm, which was attributed to a speed-up of the SESAM recovery rate due to the enhanced carrier sweep-out at higher bias fields. And in Ref. [90], when applying the reverse bias to the E-SESAM, a pulse shortening from 17.4 to 6.4 ps and a spectral shift from 1280 to 1282 nm were observed.

However, the ultrafast laser is a complex system, where the SESAM action is interplay with gain dynamics, gain curvature and other wavelength, power and time dependent loss factors in the oscillating laser cavity. In this chapter, a simple and direct experiment to characterize the E-SESAM action alone was realized by measuring the nonlinear reflectivity of femtosecond laser pulses as a function of both pump fluence and the reverse bias voltage on the E-SESAM.

6.2 Experimental Setup

Our *p-i-n*-junction-based E-SESAM structure was grown on an n-doped GaAs substrate using a standard molecular beam epitaxy. It had an n-doped 34-period long $GaAs/Al_{0.9}Ga_{0.1}As$ Bragg reflector with the stop band covering the range $1014 - 1126$ nm, followed by an undoped saturable absorber section and a *p*-doped GaAs cap layer, as shown in the upper part of Figure 6.1. The saturable absorber section featured 3 $LT - In_{0.2}Ga_{0.8}As/GaAs$ QWs with the QW width of 8 nm, additionally surrounded by $GaAs_{0.75}P_{0.25}$ barriers on each side for strain compensation in the QWs. The total thickness of the intrinsic section was 155 nm, and the potential drop of the *p-i-n* junction was approximately 1.0 V, resulting in the built-in electric field on the QWs of around 65 kV/cm as shown in the down part

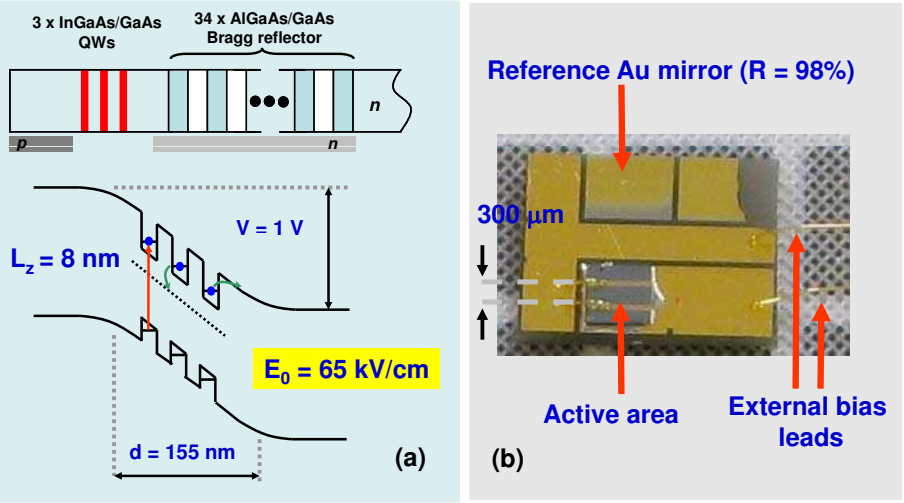

Figure 6.1: (a) Schematic of an E-SESAM. (b) Photograph of an E-SESAM chip; Au: reference golden mirror and V: external bias contacts.

of Figure 6.1 (a). The flat electrode was applied to the back of the n-doped GaAs substrate and narrow stripe electrodes separated by approximately 300 um were deposited on the p-doped cap layer, providing the free optical access to the SESAM. The photograph of the E-SESAM chip is shown in Figure 6.1(b). The E-SESAM area on the chip was around $1 \times 1\,mm^2$.

Figure 6.2 shows a small-signal reflectivity spectrum of the E-SESAM at zero external bias and the intensity spectrum of the output of the femtosecond laser used in the nonlinear reflectivity measurements. The peak of the optical absorption of the QWs in the E-SESAM at zero external bias is around 1056 nm. As described in chapter 4, the laser was a monolithic Yb-fiber femtosecond laser [55] operating at central wavelength of 1065 nm at the repetition rate of 45 MHz and providing the pulses of approximately 450 fs duration (FWHM) as assumed from the 650 fs long autocorrelation in Figure 6.3 (a). The laser output was focused onto the surface of the E-SESAM in between the stripe electrodes, and the incident and reflected laser power was measured using the calibrated powermeters as shown in Figure 6.3 (b). The laser pump fluence on the E-SESAM was varied in the range $1.6 - 26.7 uJ/cm^2$ with a $\lambda/2$-plate and a polarizer. A reference golden mirror with the reflectivity of 98% which is also deposited on the E-SESAM chip was used for absolute calibration of the reflectivity values.

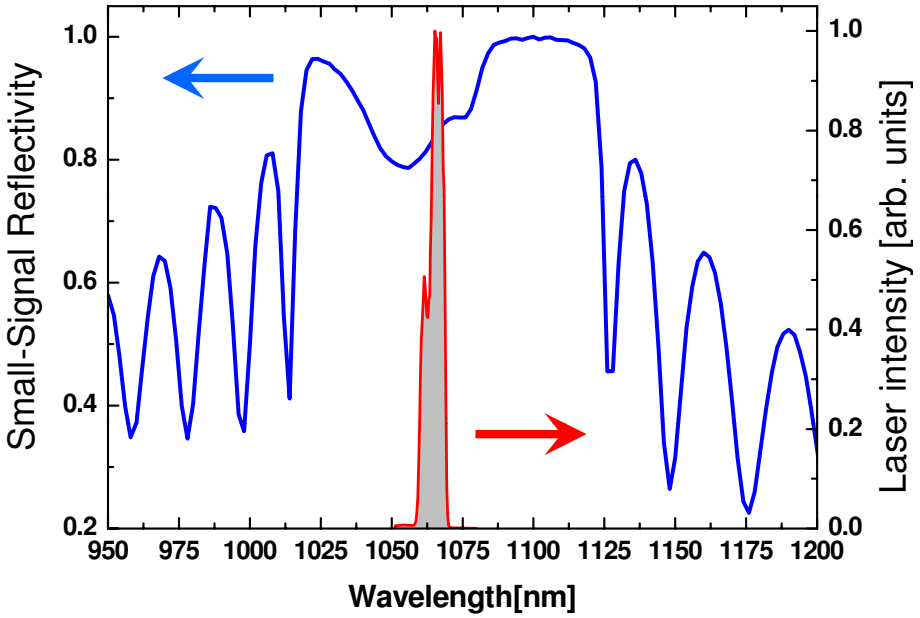

Figure 6.2: E-SESAM small-signal reflectivity spectrum at zero external bias and the intensity spectrum of the femtosecond laser output used in the nonlinear reflectivity experiment.

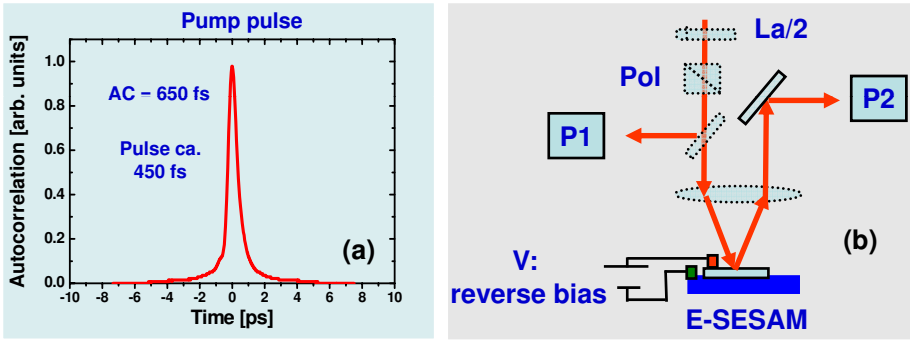

Figure 6.3: (a) The autocorrelation of input laser pulse. (b) The experiment setup.

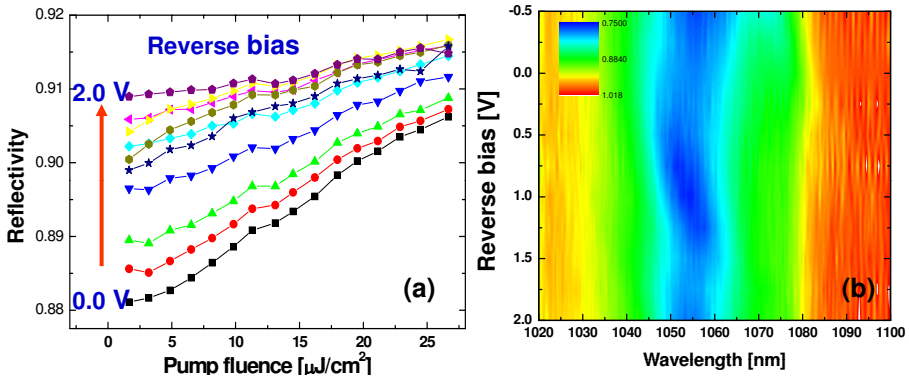

Figure 6.4: (a) Reflectivity of E-SESAM as a function of pump fluence, at different values of reverse bias in the range $0-2$ *V. (b) Reflectivity of E-SESAM as a function of selected bias values, at different wavelength.*

6.3 Experimental Results

The dependency of the E-SESAM reflectivity R on the pump fluence F_p for different valuse of applied reverse bias V is shown in Figure 6.4 (a). In order to prevent the electric breakdown of the *p-i-n* structure, in all experiments the reverse bias was limited to 2 V and the forward bias to 0.5 V in $R(V, \lambda)$ measurements. A typical SESAM behavior was observed for all values of V - in the whole range of the F_p, the reflectivity R grows with increase in the pump fluence. It should be noted that within the pump fluence range available to us $(1.6 - 26.7uJ/cm^2)$ the full saturation of QW absorption couldn't be reached. With increase in V, the overall E-SESAM reflectivity increases, thus showing a reduction in E-SESAM loss, with a significant decrease in the slope of the dependency $R(F_p)$. The dynamics of $R(V)$ is most dramatic at weaker pump fluence, as compared to the stronger pump. In Figure 6.6 (a), the dependency $R(V)$ is shown for two extreme values of pumping fluences available in this experiment. At weakest pump, the $R(V)$ first grows with the reverse bias in the range $0 - 4$ V which is corresponding to the total electric field on the QWs $E_{tot} = 65 - 130\,kV/cm$, and then shows an oscillation between 1 and 2 V with $E_{tot} = 194\,kV/cm$. The total voltage-induced reflectivity modulation is around 3%. At strongest pump $R(V)$ also grows in the range $V = 0 - 1$ V and then rolls-off at higher values of V, but with the total modulation of only around 1%. In Figure 6.5(b)the modulation depth ΔR achieved in this experiment - the difference between the R values measured at the extreme pump fluences is shown as a function of V. The dependency $\Delta R(V)$ is clearly dominated by the dependency of

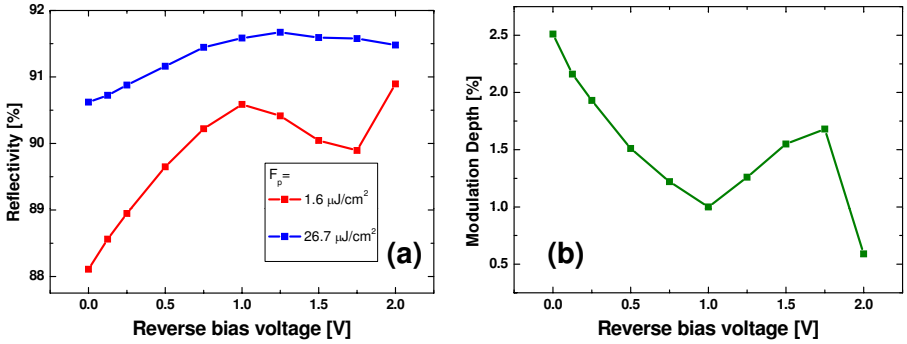

Figure 6.5: (a)Reflectivity of the E-SESAM at a pump fluence of 1.6 and 26.7 uJ/cm^2, as a function of reverse bias. (b) Modulation depth of the E-SESAM as a function of reverse bias.

$R(V)$ at weakest pump. $\Delta R$is the largest at reverse bias $V = 0$ and reaches about 2.5%. At $V = 1\,V$, ΔR reaches a local minimum of about 1% and then shows an oscillation before reaching its absolute minimum of around 0.5% at $V = 2\,V$.

The spectrum which is partly shown in Figure 6.4(b) and the autocorrelation of the reflected laser signal as a function of both F_P and V were also measured, but neither the reflected laser pulse shortening [91], nor its spectral expansion was observed within the accuracy of our measurements. In Ref.[84] the recovery time of a QD saturable absorber with applied electric field was found to decrease from 62 ps to 700 fs by enhanced carrier sweep-out, which is still longer than 450 fs pulses, used in our experiments.

The application of the transverse electric field to the QW results in a well-known QCSE. The QCSE manifests itself in the reduction in the optical transition energy (the Stark shift) as a result of the band structure tilt; and in the reduction in the optical absorption coefficient due to the weaker overlap of the spatially separated electron and hole wave functions. The spectrum of our laser applied to the E-SESAM which is 1065 nm is situated at the longer wavelength part than the peak of the QW absorption which is around 1050 nm. The application of the reverse bias to the E-SESAM and therefor the enhancement of the QCSE already present due to the built-in p-i-n field of $65\,kV/cm$ could thus lead to two following conflicting consequences: (I) Stark-shifting the QW absorption maximum into the laser spectrum, which is positioned at longer wavelength, thus increasing the E-SESAM loss at the laser wavelength and (II) the overall reduction in the optical absorption coefficient of the QWs. In Figure 6.6 (a) small-signal reflectivity spectra of the E-SESAM

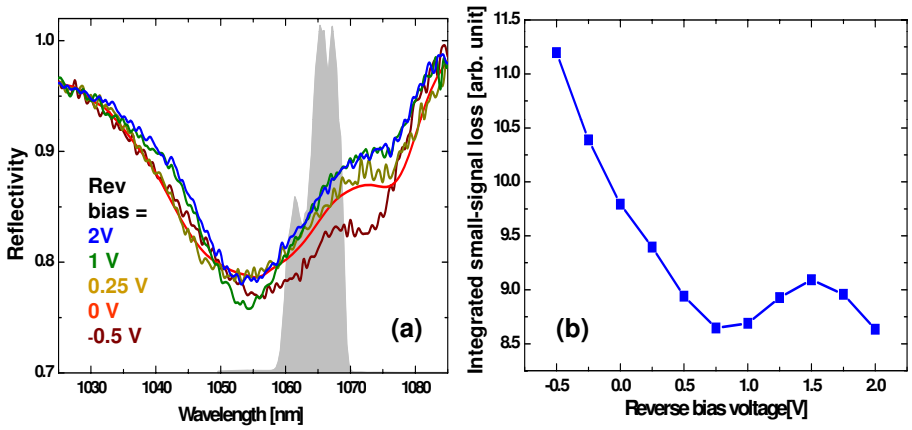

Figure 6.6: (a) Small-signal reflectivity of the E-SESAM measured at selected bias values. Laser spectrum is shown on the background. (b) Calculated small-signal loss of E-SESAM as experienced by the laser output, as a function of reverse bias.

in the vicinity of the laser spectrum, taken at different bias voltages are presented, showing a rather complex modification. One can see that both manifestations of the QCSE are present in these spectra but their respective contributions are different in different spectral ranges. The Stark shift mostly dominates around the wavelength of 1045 nm whereas the QW absorption change with applied bias seems to be the dominating effect around the central wavelength of the laser as 1065 nm. In addition to the reverse bias in the range 0-2 V, a small forward bias up to 0.5 V [89] corresponding $E_{tot} = 32\,kV/cm$ was applied to see the effect of QCSE reduction. it is clear that the QCSE from the *p-i-n* built-in electric field alone already has a significant impact on the optical properties of the SESAM.

The integrated small-signal loss, experienced by the laser in the E-SESAM at a given value of bias voltage was quantified by calculating the overlap integral between the laser intensity spectrum $I(\lambda)$ and the E-SESAM loss for different values of applied bias; $S(V) = \int_\lambda I(\lambda)[1 - R(V,\lambda)]d\lambda$, where $R(V,\lambda)$ is the E-SESAM small-signal reflectivity spectrum at specific values of bias voltage. The dependency $S(V)$ is shown in Figure 6.6 (b). It is nearly identical to the bias voltage dependency of the modulation depth $\Delta R(V)$ which is in turn dominated by the weak-pump reflectivity dependency on V.

This demonstrates that the achieved control of the modulation depth of the E-SESAM is mostly due to the modification of its small-signal loss at the laser wavelength by the QCSE. The observed decrease in the slope of $R(F_p)$ with in-

crease in V is thus a natural consequence of this effect. As the QWs become more transparent for the pump laser, $R(F_p)$ will depend less on the saturable loss, and in the limit of zero QW absorption will approach the reflectivity of a Bragg reflector when neglecting the nonsaturable loss.

6.4 Summary

One QW-based E-SESAM for the wavelength of 1065 nm has been demonstrated. The modulation depth in the pump fluence range $1.6026.7\,uJ/cm^2$ can be tuned in the range $2.5 - 0.5\%$ which is by a factor of 5, by application of the external reverse bias in the range $0 - 2\,V$. The applied bias also has a strong effect on the slope of the dependency $R(F_p)$ which is important for the self-starting of laser mode-locking. the electrical control of the E-SESAM is based on the QCSE which in this case was found to lead predominantly to the decrease in the QW small-signal absorption at the pump laser wavelength. The E-SESAM can be used for the active stabilization of ultrafast lasers and complement the passive nonlinear-optical control methods[54, 55, 53]. The reshaping of E-SESAM reflectivity spectrum by QCSE could be the reason for the laser spectral shift which was observed in Ref. [90].

Chapter 7

Amplification and Application of Monolithic Fiber Lasers

7.1 Introduction

High power stable fiber delivered laser systems with central wavelength at 1 um have attractive new applications in both scientific and industrial world [92]. The demand for higher output powers has pushed fibers towards having larger effective area with small nonlinearities. However, when increasing the fiber effective area, higher order modes are also increased for standard step-index LMA. The PCF Yb-doped amplifiers recently researched have unique properties which can be engineered to suppress high order modes and thus increase pointing stability [93]. The first part of this chapter will describe the amplification of monolithic fiber lasers by one PCF amplifier provided by NKT Photonics A/S.

The second part of this chapter demonstrates NPR induced by cross-splice PM fibers which is one of applications of the monolithic fiber lasers described in Chapter 4 and 5.

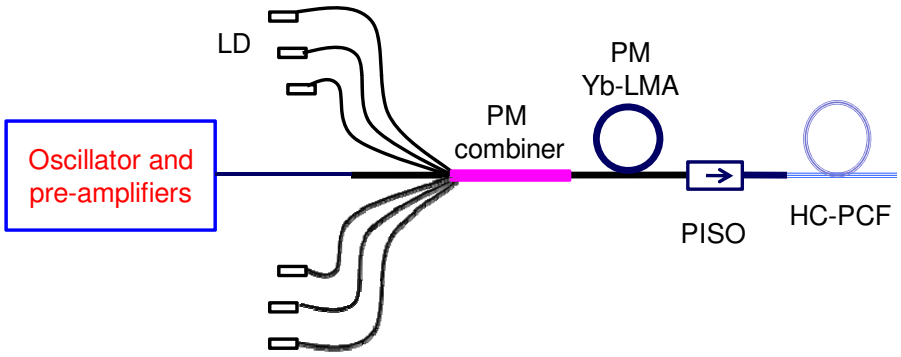

Figure 7.1: Diagram of high power amplifier and dispersion compensation setup. The detail of the oscillator and pre-amplifier shown in Figure 5.1 in absence of the pulse compression with HC-PCF, LD - pump diodes up to 10 W output at 974nm, PISO - high power isolator with PM LMA15 fiber pigtails. The amplifier is provided by NKT Photonics A/S.

7.2 High Power Yb-doped fiber Amplifier

The experimental amplification of fiber laser and pulse compression with HC-PCF setup is shown in figure 7.1. The fibers used in the amplifier are PM LMA15 [94]which keep the output pulse linearly polarized. HC-PCF with proper length (see Figure 1.2 (a)) is spliced after the amplifier for dispersion compensation. The splicing loss between PM LMA15 to HC-PCF is around 0.7 dB.

The autocorrelation and spectrum of input pulse before the amplifier is shown as the solid line in the middle of Figure 5.5 (a) and (b) respectively. In Figure 7.2 the output spectra measured at the end of the laser after HC-PCF with different length and different output power are shown. We note here, that the shown spectrum intensity are dependent on the coupling coefficient to the OSA and so that are not real laser output intensity. It can be seen that with the output power increasing, the nonlinear Raman Effect is more obvious which is the wavelength redshif in Figure 7.2. This is one of the main limitations for high power output. Another problem is that it is difficult to build a low loss high power isolator with fiber pigtails on the both sides. The high power isolator used in our experiment has an insertion loss up to 3.4 dB which lowered the output power as well as distorted the pulse shape.

The noncollinear intensity autocorrelation of the output after the compression is shown in Figure 7.3. The FWHM is dependent on the length of compression

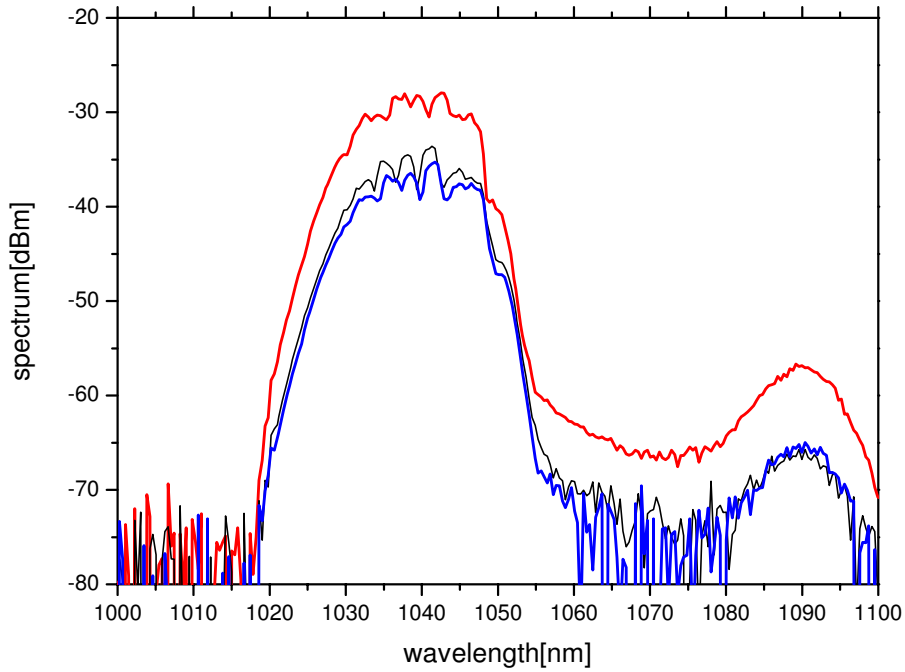

Figure 7.2: Output spectrum dependent on length of compensation fiber HC-PCF and power. Red line: without compensation fiber HC-PCF, 3.23 W output; purple line: 26.1 m HC-PCF and 2.1 W output, bule line: 26.1 m HC-PCF and 1.09 W output; deep blue line: 20 m HC-PCF and 1.59 W output, black line::20 m HC-PCF and 1.51 W output. It is noted that the spectrum intensity shown in this diagram is not real and dependent on power coupling coefficients to the OSA.

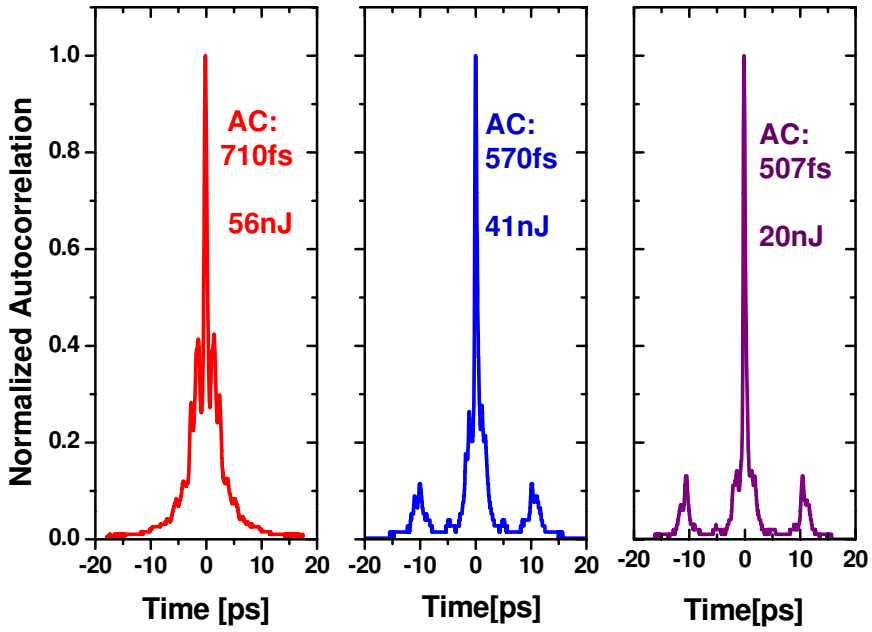

Figure 7.3: Autocorrelation traces with different output power.

HC-PCF fibers as well as the output power. When output power up to 56 nJ, the measured autocorrelation is 710 fs. The side pulses as can been seen from Figure 7.3 are caused by the non-compensated third-order dispersion of HC-PCF. The all-fiber system described above has one user-accessible degress of tuning freedom - change in the power provided by the pumping diodes. Figure 7.4 demonstrates the dependencies of the resulting pulse autocorrelation duration and output pulse power on the end amplifier pump power as well as the length of HC-PCF fiber. One can see that when the pump power increasing, the output power also increased, however the pulse duration is also broadened.

7.3 Nonlinear Optical Enhancement and Limiting in a Cross-Spliced All-Fiber Link

One application of the ultrafast laser is the demonstration of NPR. As described in Chapter 2, NPR can be used for mode-locking of ultrafast solid state and fiber

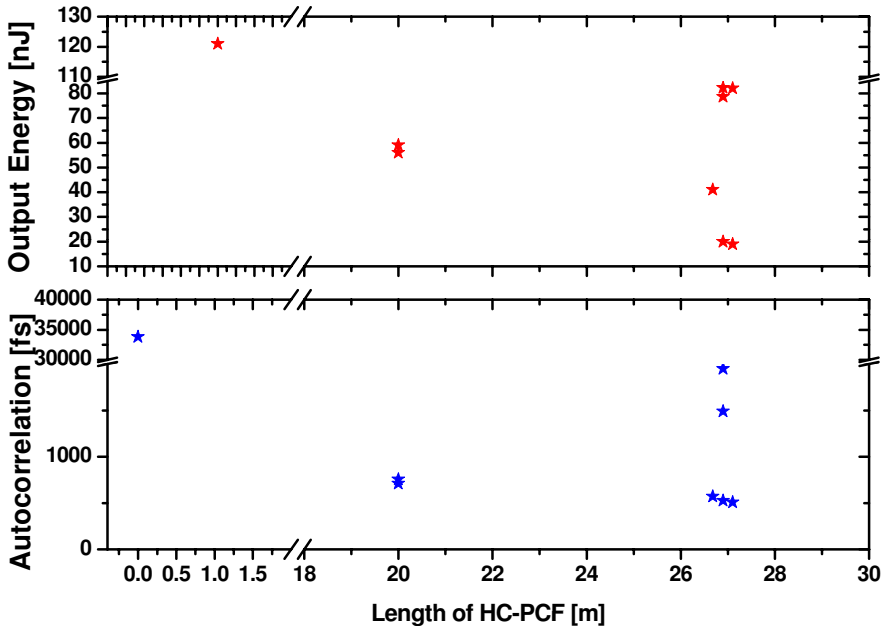

Figure 7.4: Dependence of output power and autocorrelation pulse duration at the length of compensation fiber HC-PCF.

lasers [95]. Using cross-spliced PM fibers is a particularly promising way to achieve an NPR-based modelocking scheme [96]. However, the direct optical enhancement and/or limiting action of a cross-spliced fiber link for ultrafast laser applications has not been demonstrated, to the best of our knowledge. In this work, we present a direct study of NPR in a fiber link by using ultrashort laser pulses, and the nonlinear modulation of the laser intensity of 56% is demonstrated.

The experimental setup used for the NPR measurement is shown in Figure 7.5 (a). We note that in Refs. [97] NPR was also measured in a highly birefringent optical fiber. However, in this case a very strong spectral interference between two polarization states can be induced which will seriously affect the stable pulse in mode-locking lasers. In our scheme, we used a combination of the non-PM fiber spliced to two cross-spliced PM fibers.

The cross-splicing angle between the PM axes of the two PM fibers was chosen to be 22^0, which will result in the maximum intensity modulation depth induced by the NPR [98]. The PM fibers used in the cross-splicing were 12cm (L1) and 2mm (L2) - long, respectively, and were followed by 4.7 m (L3) - long HI1060 non-PM

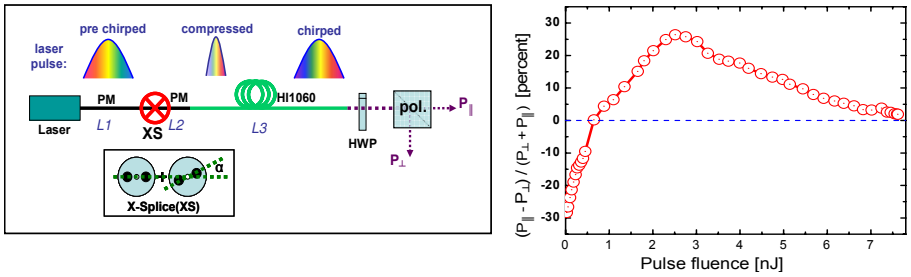

Figure 7.5: (a) Fiber link layout and experimental setup: PM - polarization maintaining fiber, HWP - half wave plate, pol. - polarizer. (b) Intensity discrimination for 2 orthogonal output polarizations as a function of input pulse energy.

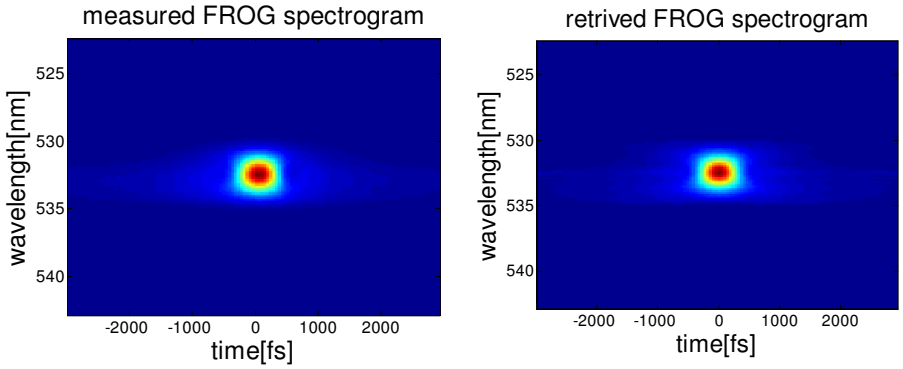

Figure 7.6: (a) Measured SHG FROG trace from one monolithic fiber laser described in chapter 5. (b) Computed SHG FROG trace of the retrived pulse.

fiber. The length of one of the PM fibers of 2mm is shorter than the beat length, which helped us to avoid polarization-state interference. The fiber link and the schematic of the measurements is presented in Figure 7.5 (a).

The details on the pump laser used in the measurements was described in Chapter 5 and can be found in [53, 54].

The laser pulses used in our experiment had FWHM of 420 fs when fully compressed (See. Figure 7.8(a)). Its Frog traces are shown in Figure 7.6. The measured and retrieved pulse autocorrelation, pulse intensity and phase are shown in Figure 7.7. They were negatively pre-chirped to 2.68 ps, in order to provide the shortest duration while in the non-PM HI1060 fiber, thus achieving the strongest NPR. We note here that the dispersion of all fibers used in the link is normal. The intensity

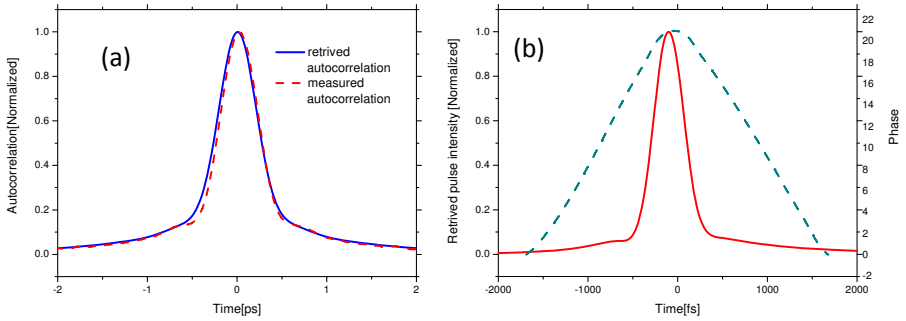

Figure 7.7: (a) Measured (dash) and Retrieved (solid) pulse autocorrelation. (b) Retrieved intensity (red line) and phase (dash) vs. time. FROG error $< 0.95\%$.

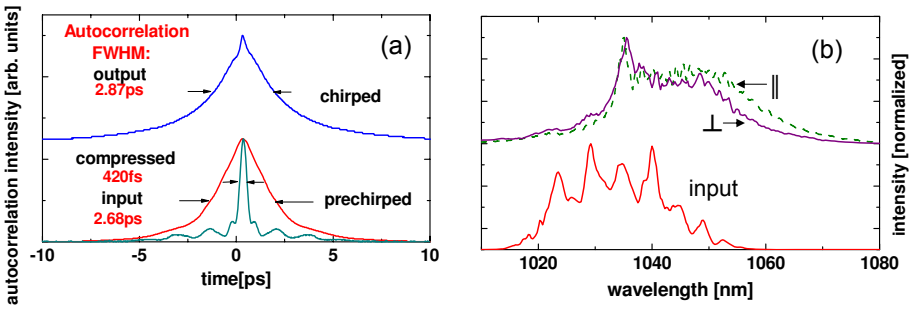

Figure 7.8: (a) Autocorrelation trace of the pulses: green line - the compressed laser output, red line - negatively pre-chirped pulse used at the input, blue line - positively chirped laser pulse at the output of the fiber link. (b) Laser spectra measured after the laser (red), fast axis of the output (dash) and slow axis of the output (purple).

discrimination between the two orthogonal polarization states of the output signal as a function of the input pulse energy is demonstrated in Figure 7.5(b). It is clearly seen that the intensity distribution switches between the two polarization states, with the total modulation reaching as much as 56 %.

In Figure 7.8 we show the measured autocorrelation and spectrum of the laser signal before and after the cross-spliced fiber link. The output spectra of the two orthogonal polarization states clearly shows no signs of strong interference that would affect the performance of the laser based on this nonlinear pulse control scheme. The output spectrum shows narrowing and a certain red-shift in comparison with the

input spectrum, which is probably due to the combination of self-phase modulation, cross-phase modulation and dispersion effects.

The achieved power modulation depth of 56%, and the absence of strong interference in the output spectra indicates that this cross-spliced link can be used *for both passive mode-locking and stabilization* of ultrashort all-fiber lasers. It could serve as an alternative to SESAM mode-locking (see e.g. [55, 53, 54]), and provide a much better laser durability since the SESAMs are prone to burn-out effects. It can also at the same time replace the nonlinear-optical stabilization schemes such as the ones relying on optical limiting in fiber Bragg gratings and dispersive photonic crystal fibers. The work on implementation this nonlinear control scheme in an environmentally stable all-fiber femtosecond laser is currently in progress.

7.4 Summary

The amplification and application of our monolithic fiber lasers have been demonstrated. With the PM PCF fiber amplifier and HC-PCF for output dispersion compensation technology, pulses with dozens of nJ power and under ps temporal duration can be delivered directly from fiber. This stable high power laser system can have practical applications. The NPR of cross-spliced PM fibers are also demonstrated. The achieved 56% modulation depth and the absence of interference in the output spectra indicates the possibility of mode-locking by the cross-spliced link.

Chapter 8

Summary and outlook

This thesis is mainly focus on the development of new stable monolithic fiber lasers and fiber laser systems with the central wavelength around 1 um. One of the most important applications in our case is for biophotonic imaging [81, 92].

The development of PCFs has provided new fiber based on products which are interesting for the realization of stable mode-locked fiber laser systems. One main part of this thesis is based on the adoption of different PCFs which are used for dispersion compensation intra and extra laser oscillating cavity, laser stabilization, high power amplification and supercontinuum generation and so on.

Different mode-locking mechanisms are mentioned. Both the monolithic fiber lasers described in thesis are based on SESAM. One QW-base E-SESAM with tunable modulation depth is also demonstrated and it can be used for active stabilization of ultrafast lasers and complement the passive nonlinear-optical control methods. The NPR realized by cross-spliced fiber link makes another kind of all fiber lasers possible.

The theory and basic numeral modeling about pulse propagation though fibers are presented in Chapter 2. It includes fiber dispersion effect, gain and nonlinear effect e.g. self phase modulation, Raman effect and nonlinear polarization rotation. Some simulation results are also shown. Chapter 2 also demonstrates the theory about passive mode-locking mechanisms including nonlinear polarization rotation and mode-locked with SESAM.

The dispersion measurements are all done by myself and I improved the setup

from [46]. The measured dispersion results are accurate compared with the data by traditional commercial dispersion method. The intensity autocorrelator was built by D. Turchinovich before I started my PhD and I rebuilt it several times afterwards. The FROG setup initially was built by R. K. Olsson and I built it again to my lab with the help from H. Tu. The retrived pulse autocorrelations from FROG are perfectly matched with the ones measured by the intensity autocorrelator.

Chapter 4 describes one 1064 nm all-PM fiber laser stabilized with a narrow-band Brag-grating. It was built by D. Turchinovich and I did the HC-PCF cut back experiments for dispersion compensation measurements. This laser is long term stable and is also the source for characterizing the E-SESAM presented in Chapter 6.

I built the highly-stable monolithic femtosecond 1035 nm laser alone and also did some simulation work, however the modeling results shown in this thesis were done by J. Lægsgaard. The laser system is self starting and quiet stable even when the temperature changed from 10° to 40°. And the stability test was done in NKT Photonics A/S. At the moment, the laser system is in the lab of UIUC for biophotonic imaging experiments.

The experimental work about the E-SESAM characterization was finished with the help from D. Turchinovich. The results demonstrate the modulation depth of the E-SESAM can be tuned in the range $2.5 - 0.5\%$ which is by a factor of 5, by application of the external reverse bias in the range $0 - 2V$, so that it can be used for active stabilization of ultrafast lasers.

The experiments of high power amplification, supercontinuum generation and NPR realization by cross-spliced fiber link are also done by myself. The PM PCFs Yb-doped high power amplifier is provided by NKT Photonics A/S. The output power loss from after the amplification and compression mainly comes from the high insertion loss of the fiber pigtailed isolator (3.4 dB), splicing loss between LMA15 fiber and HC-PCF (0.7 dB) and the transmission loss of HC-PCF (1.7 dB for 20 m HC-PCF).

The main PhD work has been described above and the possible improvements will de discussed as below.

Stable, compact and low consumption ultrashort laser systems with high power and nice short temporal shapes output are always preferred for applications. The monolithic fiber lasers described in this thesis are already stable, compact and low cost. The output power range and pulse duration are still needed to be improved.

High power PCFs amplifiers can provide enough amplification and the limitation for directly high power fiber delivery now is mainly on the high power fiber coupled isolator. As long as the insertion loss of the isolator decreases, the final output power can be doubled. Another factor is the nonlinear Raman effect on the amplifier for which low nonlinearity LMA fibers are needed.

Third order dispersion can induce significant chirp into ultrashort pulses. Ultrafast lasers with free space output can deliver near transform-limited pulses with nice pulse shapes. This is because the pulses can be compressed by the combination of gratings, lens and chirped mirrors which can compensate not only the second-order dispersion but also the third-order dispersion. With all-fiber lasers, all the dispersion compensation are done by fibers. Nowadays, it is not easy to find a pair of fibers which can both compensate the GVD and TOD at the same time, meanwhile with required nonlinearity. With the more widely research on PCFs, it is more and more possible to design such fibers with which the fiber laser can deliver much shorter pulses than what we have now.

In reality, another key issue about ultrafast lasers are their lifetime which is dependent on the lifetime of the components in the laser system. For fiber lasers mode-locked with SESAM, the lifetime of SESAM becomes a big issue since its quality degrades with time and is easily permanent damaged when pulse fluctuations larger than the threshold of SESAM. There are some solutions: to design new SESAM, move the pulse spot to another place on the SESAM mechanically or mode-locking in the absence of SESAM. Mode-locking with NPR induced by cross-spliced fiber link is one solution and we are trying to realize it.

Bibliography

[1] A. J. DMaria, D. A. Stetser, and H. Heynau. Self mode-locking of lasers with saturable absorbers. *Applied Physics Letters*, 8(7):174–176, 1966.

[2] J. C. Diels and W. Rudolph. *Ultrashort Laser Pulse Phenomena*. Elsevier, 2nd edition, 2006.

[3] L. He, K. Sheehy, and W. Culbertson. Femtosecond laser-assisted cataract surgery. *Current opinion in ophthalmology*, Dec 9 2010.

[4] E. Balestrazzi and L. Mosca. New femtosecond laser technology applications in corneal lamellar surgery. *Annals of ophthalmology (Skokie, Ill.)*, 42 Spec No:5–9, 2010.

[5] R. R. Gattass, L. R. Cerami, and E. Mazur. Micromachining of bulk glass with bursts of femtosecond laser pulses at variable repetition rates. *Optics express*, 14(12):5279–5284, Jun 12 2006.

[6] B. Dusser, Z. Sagan, H. Soder, N. Faure, J. P. Colombier, M. Jourlin, and E. Audouard. Controlled nanostructrures formation by ultra fast laser pulses for color marking. *Optics express*, 18(3):2913–2924, Feb 1 2010.

[7] M. Nagai, K. Tanaka, H. Ohtake, T. Bessho, T. Sugiura, T. Hirosumi, and M. Yoshida. Generation and detection of terahertz radiation by electro-optical process in gaas using $1 \cdot 56 \mu m$ fiber laser pulses. *Applied Physics Letters*, 85(18):3974–3976, 2004.

[8] D. Turchinovich, P. U. Jepsen, B. S. Monozon, M. Koch, S. Lahmann, U. Rossow, and A. Hangleiter. Ultrafast polarization dynamics in biased quantum wells under strong femtosecond optical excitation. *Physical Review B (Condensed Matter and Materials Physics)*, 68(24):241307–1–4, 2003.

[9] H. Kalaycioglu, B. Oktem, Ç. Senel, P. P. Paltani, and F. Ö. Ilday. Microjoule-energy, 1 mhz repetition rate pulses from all-fiber-integrated nonlinear chirped-pulse amplifier. *Optics Letters*, 35(7):959–961, 2010.

[10] F. Ö. Ilday, J. Chen, and F. Kartner. Generation of sub-100-fs pulses at up to 200 mhz repetition rate from a passively mode-locked yb-doped fiber laser. *Optics express*, 13(7):2716–2721, Apr 4 2005.

[11] C. Rullière. *Femtosecond Laser Pulses Priniples and Experiments*. Springer Scince and Business Media, 2nd edition, 2005.

[12] C. K. Nielsen, K. G. Jespersen, and S. R. Keiding. A 158 fs 5.3 nj fiber-laser system at 1 microm using photonic bandgap fibers for dispersion control and pulse compression. *Optics express*, 14(13):6063–6068, Jun 26 2006.

[13] J. C. Knight, T. A. Birks, P. J. Russell, and D. M. Atkin. Dispersion measurement of arrayed-waveguide gratings by fourier transform spectroscopy. *Optics Letters*, 21(19):1547–1549, 1996.

[14] http://www.nktphotonics.com/fiber.

[15] J. Lægsgaard. *Introduction to dielectric waveguides*. DTU Fotonik, 2009.

[16] J. C. Knight, J. Broeng, T. A. Birks, and P. St. J. Russell. Photonic band gap guidance in optical fibers. *Science*, 282(5393):1476–1478, 1998.

[17] J. Lægsgaard. Mode profile dispersion in the generalised nonlinear schrödinger equation. *Optics express*, 15(24):16110–16123, Nov 26 2007.

[18] J. M. Dudley, G. Genty, and S. Coen. Supercontinuum generation in photonic crystal fiber. *Reviews of Modern Physics*, 78(4):1135–1184, 2006.

[19] G. P. Agrawal. *Nonlinear Fiber Optics*. Academic Press, 3rd edition, 2005.

[20] F. DeMartini, C. H. Townes, T. K. Gustafson, and P. L. Kelley. Self-steepening of light pulses. *Physics Review*, 164(2):312–323, Dec 1967.

[21] D. Grischkowsky, E. Courtens, and J. A. Armstrong. Observation of self-steepening of optical pulses with possible shock formation. *Physics Review Letters*, 31(7):422–425, Aug 1973.

[22] I. D. Jung, F. X. Kärtner, N. Matuschek, D. H. Sutter, F. Morier-Genoud, Z. Shi, V. Scheuer, M. Tilsch, T. Tschudi, and U. Keller. Semiconductor saturable absorber mirrors supporting sub-10-fs pulses. *Applied Physics B Lasers and Optics*, 65(2):137–150, 1997.

[23] F. Shimizu. Frequency broadening in liquids by a short light pulse. *Physical Review Letters*, 19(19):1097–1110, 1967.

[24] E. P. Ippen, C. V. Shank, and T. K. Gustafson. Self-phase modulation of picosecond pulses in optical fibers. *Applied Physics Letters*, 24(4):190–192, 1974.

[25] K. Rottwitt. *Notes to course 34052 and Nonlinear optics.* DTU Fotonik, 2008.

[26] R. G. Smith. Optical power handling capacity of low loss optical fibers as determined by stimulated raman and brillouin scattering. *Applied Optics*, 11(11):2489–2494, 1972.

[27] H. W. Etzel, H. W. Candy, and R. J. Ginther. Stimulated emission of infrared radiation from ytterbium-activated silicate glass. *Applied Optics*, 1, 1962.

[28] H. Garcia, A. W. Johnson, F. A. Oguama, and S. Trivedi. Pump-induced nonlinear refractive-index change in erbium- and ytterbium-doped fibers: theory and experiment. *Optics Letters*, 30(11):1261–1263, 2005.

[29] R.Paschotta, J. Nilsson, A. C. Tropper, and D. C. Hanna. Ytterbium-doped fiber amplifiers. *IEEE Journal of Quantum Electronics*, 33(7):1049–1056, 1997.

[30] J. Lægsgaard. Control of fibre laser mode-locking by narrow-band bragg gratings. *Journal of Physics B: Atomic, Molecular and Optical Physics*, 41(9), 2008.

[31] http://www.nufern.com/fiber_detailed.php/84.

[32] U. Keller. Recent developments in compact ultrafast lasers. *Nature*, 424(6950):831–838, Aug 14 2003.

[33] F. Ö. Ilday and F. W. Wise. Nonlinear wave phenomena in confined structures - nonlinear effects in fibers - nonlinearity management: A route to high-energy soliton fiber lasers. *Journal of the Optical Society of America - B - Optical Physics*, 19(3), 2002.

[34] H. A. Haus. Mode-locking of lasers. *IEEE Journal of Slected Topics in Quantum Electronics*, 6(6):1173–1185, 2000.

[35] F. Ö. Ilday, J. Buckley, L. Kuznetsova, and F. W. Wise. Generation of 36-femtosecond pulses from a ytterbium fiber laser. *Optics Express*, 11(26):3550–3554, 2003.

[36] K. Ögöen and F. ÖIlday. All-fiber all-normal dispersion laser with a fiber-based lyot filter. *Optics Letters*, 35(8):1296–1298, 2010.

[37] K. Kieu and F. W. Wise. All-fiber normal-dispersion femtosecond laser. *Optics Express*, 16(15):11453–11458, 2008.

[38] H. Lim, Y. Jiang, Y. Wang, Y. C. Huang, Z. Chen, and F. W. Wise. Ultrahigh-resolution optical coherence tomography with a fiber laser source at 1 um. *Optics Letters*, 30(10):1171–1173, 2005.

[39] http://www.batop.de/information.

[40] X. Liu, E. U. Rafailov, D. Livshits, and D. Turchinovich. Quantum well saturable absorber mirror with electrical control of modulation depth. *Applied Physics Letters*, 97(5):051103, 2010.

[41] M. Haiml, R. Grange, and U. Keller. Optical charactriztion of semiconductor saturable absorbers. *Applied Physics B*, 79, 2004.

[42] L. G. Cohen and Chinlon Lin. Pulse delay measurements in the zero material dispersion wavelength region for optical fibers. *Applied Optics*, 16(12):3136–3139, 1977.

[43] L. G. Cohen. Comparison of single-mode fiber dispersion measurement techniques. *Journal of Lightwave Technology*, 3(5):958–966, 1985.

[44] J. Y. Lee and D. Y. Kim. Versatile chromatic dispersion measurement of a single mode fiber using spectral white light interferometry. *Optics express*, 14(24):11608–11615, Nov 27 2006.

[45] J. Gehler and W. Spahn. Dispersion measurement of arrayed-waveguide gratings by fourier transform spectroscopy. *Journal of Lightwave Technology*, 36(4):338–339, 2000.

[46] T. J. Ahn, Y. Jung, K. Oh, and D. Y. Kim. Optical frequency-domain chromatic dispersion measurement method for higher-order modes in an optical fiber. *Optics express*, 13(25):10040–10048, Dec 12 2005.

[47] R. Trebino. *Frequency-Resolved Optical Gating: the measurement of Ultrashort Laser Pulses*. Kluwer Academic Publishers, 2002.

[48] E. S. Kintzer and C. Rempel. Near-surface second-harmonic generation for autocorrelation measurements in the uv. *Applied Physics B: Lasers and Optics*, 42(2):91–95, 1987.

[49] R. Trebino and D. J. Kane. Using phase retrieval to measure the intensity and phase of ultrashort pulses: frequency-resolved optical gating. *JOSA A*, 10(5):1101–1111, 1993.

[50] R. K. Olsson. *Optical fiber links for transmission of nanojoule femtosecond laser pulses.* PhD thesis, DTU Fotonik, 2010.

[51] http://www.femtosoft.biz/frog.shtml.

[52] K. W. Delong, D. N. Fittinghoff, and R. Trebino. Practical issues in ultrashort-laser-pulse measurement using frequency-resolved optical gating. *IEEE Journal of Quantum Electrinics*, 32(7):1253–1264, 1996.

[53] X. Liu, J. Laegsgaard, and D. Turchinovich. Self-stabilization of a mode-locked femtosecond fiber laser using a photonic bandgap fiber. *Optics Letters*, 35(7):913–915, Apr 1 2010.

[54] X. Liu, J. Laegsgaard, and D. Turchinovich. Highly-stable monolithic femtosecond yb-fiber laser system based on photonic crystal fibers. *Optics express*, 18(15):15475–15483, Jul 19 2010.

[55] D. Turchinovich, X. Liu, and J. Laegsgaard. Monolithic all-pm femtosecond yb-fiber laser stabilized with a narrow-band fiber bragg grating and pulse-compressed in a hollow-core photonic crystal fiber. *Optics express*, 16(18):14004–14014, Sep 1 2008.

[56] J. T. Kristensen, A. Houmann, X. Liu, and D. turchinovich. Low-loss polarization-maintaining fusion splicing of single-mode fibers and hollow-core photonic crystal fibers, relevant for monolithic fiber laser pulse compression. *Optics express*, 16(13):9987–9995, 2008.

[57] S. W. Clark, F. Ö. Ilday, and F. W. Wise. Fiber delivery of femtosecond pulses from a ti:sapphire laser. *Optics Letters*, 26(17):1320–1322, 2001.

[58] A. Chong, W. H. Renninger, and F. W. Wise. Environmentally stable all-normal-dispersion femtosecond fiber laser. *Optics Letters*, 33(10):1071–1073, 2008.

[59] F. Ö. Ilday, J. R. Buckley, H. Lim, F. W. Wise, and W. G. Clark. Ultrafast optics - generation of 50-fs, 5-nj pulses at 1.03 mm from a wave-breaking-free fiber laser. *Optics Letters*, 28(15), 2003.

[60] B. Ortac, J. Limpert, and A. Tunnermann. High-energy femtosecond yb-doped fiber laser operating in the anomalous dispersion regime. *Optics Letters*, 32(15):2149–2151, Aug 1 2007.

[61] J. Nilsson and D. N. Payne. High-power fiber lasers. *Science*, 332(6032):921–922, 2100.

[62] http://www.nufern.com/specsheets/pm980130014xx1550hp.pdf.

[63] http://www.crystal-fibre.com/datasheets/HC-1060-02.pdf.

[64] L.Sala, G.A.Kenney-Wallace, and G.E.Hall. Cw autocorrelation measurements of picosecond laser pulses. *IEEE Journal of Quantum Electronics*, 16:990–996, 1980.

[65] G.Paunescu, J.Hein, and R.Suerbrey. 00-fs diode-pumped yb:kgw mode-locked laser. *Applied Physics B*, 79:555–558, 2004.

[66] P.Rußbüldt, T.Mans, D.Hoffmann, and R.Poprawe. High power yb:yag innoslab fs-amplifier. In *CTuK5*, San Jose, CA, 2008.

[67] M. E. Fermann, V. I. Kruglov, B. C. Thomsen, J. M. Dudley, and J. D. Harvey. Self-similar propagation and amplification of parabolic pulses in optical fibers. *Physics Review Letters*, 84:6010–6013, 2000.

[68] J. Limpert, T. Schreiber, H. Zellmer S. Nolte, and A. Tünnermann. All fiber chirped-pulse amplification system based on compression in air-guiding photonic bandgap fiber. *Optics express*, 11:3332–3337, 2003.

[69] H. Lim, F. Ö. Ilday, and F. W. Wise. Femtosecond ytterbium fiber laser with photonic crystal fiber for dispersion control. *Optics Express*, 10(25), 2002.

[70] J. K. Lyngsø, B. J. Mangan, and P. J. Roberts. Polarization maintaining hybrid tir/bandgap all-solid photonic crystal fiber.

[71] C. B. Olausson, C. I. Falk, J. K. Lyngsø, B. B. Jensen, K. T. Therkildsen, J. W. Thomsen, K. P. Hansen, A. Bjarklev, and J. Broeng. Amplification and ase suppression in a polarization-maintaining ytterbium-doped all-solid photonic bandgap fibre. *Optics Express*, 16, 2008.

[72] H. A. Haus, K. Tamura, L. E. Nelson, and E. P. Ippen. Stretched-pulse additive pulse mode-locking in fiber ring lasers: theory and experiment. *IEEE Journal of Quantum Electronics*, 31(3):591–598, 1995.

[73] S. Namiki, E. P. Ippen, H. A. Haus, and C. X. Yu. Energy rate equations for mode-locked lasers. *Journal of the Optical Society of America B (Optical Physics)*, 14(8):2099–2111, 1997.

[74] J. Lægsgaard and P. J. Roberts. Compression of realistic laser pulses in hollow-core photonic bandgap fibers. *Journal of the Optical Society of America B: Optical Physics*, 26(4):783–791, 2009.

[75] T. C. Newell, P. Peterson, A. Gavrielides, and M. P. Sharma. Temperature effects on the emission properties of yb-doped optical fibers. *Optics Communications*, 273(1):256–259, 2007.

[76] J. Mangeney, N. Stelmakh, F. Aniel, and P. Boucaudand J.-M. Lourtioz. Temperature dependence of the absorption saturation relaxation time in light- and heavy-ion-irradiated bulk gaas. *Applied Physics Letters*, 80(25):4711–4713, 2002.

[77] E. Le Cren, S. Lobo, S. Feve, and J.-C. Simon. Polarization sensitivity characterization under normal incidence of a multiple quantum wells saturable absorber nonlinear mirror as a function of the temperature of the chip. *Optics Communications*, 254(1-3):96–103, 2005.

[78] J. K. Ranka, R. S. Windeler, and A. J. Stentz. Visible continuum generation in air-silica microstructure optical fibers with anomalous dispersion at 800 nm. *Optics Letters*, 25(1):25–27, 2000.

[79] H. Tu, Y. Liu, D. Turchinovich, and S. A. Boppart. Compression of fiber supercontinuum pulses to the fourier-limit in a high-numerical-aperture focus. *Optics Letters*, 36(12):2315–2317, 2011.

[80] http://www.nktphotonics.com/files/files/SC-3.7-975-071031.pdf.

[81] H. Tu and S. A. Boppart. Versatile photonic crystal fiber-enabled source for multi-modality biophotonic imaging beyond conventional multiphoton microscopy. *Proceedings of the SPIE - The International Society for Optical Engineering*, 7569, 2010.

[82] L. R. Brovelli, U. Keller, and T. H. Chiu. Design and operation of antiresonant fabry-perot saturable semiconductor absorbers for mode-locked solid-state lasers. *Journal of the Optical Society of America B (Optical Physics)*, 12(2):311–322, 1995.

[83] A. Jasik, J. Muszalski, K. Pierscinski, M. Bugajski, V. G. Talalaev, and M. Kosmala. Low-temperature grown near surface semiconductor saturable absorber mirror: Design, growth conditions, characterization, and mode-locked operation. *Journal of Applied Physics*, 106(5), 2009.

[84] D. B. Malins, A. Gomez-Iglesias, S. J. White, W. Sibbett, A. Miller, and E. U. Rafailov. Ultrafast electroabsorption dynamics in an inas quantum dot saturable absorber at 1.3 mu m. *Applied Physics Letters*, 89(17), 2006.

[85] D. Turchinovich, P. U. Jepsen, B. S. Monozon, M. Koch, S. Lahmann, U. Rossow, and A. Hangleiter. Ultrafast polarization dynamics in biased quantum wells under strong femtosecond optical excitation. *Physical Review B (Condensed Matter and Materials Physics)*, 68(24):241307–1–4, 2003.

[86] D. Turchinovich, B. S. Monozon, and P. U. Jepsen. Role of dynamical screening in excitation kinetics of biased quantum wells: Nonlinear absorption and ultrabroadband terahertz emission. *Journal of Applied Physics*, 99(1), 2006.

[87] B. Stormont, E. U. Rafailov, and I. G. Cormack. Extended-cavity surface-emitting diode laser as active mirror controlling modelocked ti:sapphire laser. *Electronics Letters*, 40(12), 2004.

[88] A. Isomäki, A. Vainionpää, S. Suomalainen, and O. G. Okhotnikov. Self-starting mode-locked fiber laser using biased semiconductor absorber mirror. *Proceedings of SPIE - The International Society for Optical Engineering*, 5958:1–5, 2005.

[89] A. A. Lagatsky, E. U. Rafailov, W. Sibbett, D. A. Livshits, A. E. Zhukov, and V. M. Ustinov. Quantum-dot-based saturable absorber with p-n junction for mode-locking of solid-state lasers. *IEEE Photonics Technology Letters*, 17(2):294–296, 2005.

[90] S. A. Zolotovskaya, K. G. Wilcox, A. Abdolvand, D. A. Livshits, and E. U. Rafailov. Electronically controlled pulse duration passively mode-locked cr : Forsterite laser. *IEEE Photonics Technology Letters*, 21(16):1124–1126, 2009.

[91] J. Wang, J. Wang, J. Wang, and C. Sun. Nonlinear pulse-shaping phenomena of semiconductor saturable absorber mirror. *Applied Physics Letters*, 89(23), 2006.

[92] H. Tu, Y. Liu, J. Lægsgaard, U. Sharma, M. Siegel, D. Kopf, and S. A. Boppart. Scalar generalized nonlinear schrödinger equation-quantified continuum

generation in an all-normal dispersion photonic crystal fiber for broadband coherent optical sources. *Optics Express*, 18(1):27872–27884, 2010.

[93] K. P. Hansen, J. Broeng, A. Patersson, P. M. W. S. Martin, D. Nielsen, C. Jakobsen, and H. R. Simonsen. High-power photonic crystal fibers. *Prod. SPIE*, 6102, 2006.

[94] http://www.nktphotonics.com/files/files/LMA-15-100409.pdf.

[95] M. Hofer, M. E. Fermann, F. Haberl, M. H. Oberand, and A. J. Schmidt. Mode locking with cross-phase and self-phase modulation. *Optics Letters*, 16, 1991.

[96] C. K. Nielsen and S. R. Keiding. All-fiber mode-locked fiber laser. *Optics Letters*, 32(11):1474–1476, Jun 1 2007.

[97] C. Vinegoni, M. Wegmuller, B. Huttnerand, and N. Gisin. Mode locking with cross-phase and self-phase modulation. *Journal of Optics A*, 2, 2000.

[98] R. H. Stolen, J. Botineau, and A. Ashkin. Intensity discrimination of optical pulses with birefringent fibers. *Optics Letters*, 7, 1982.